TECHNISCHE UNIVERSITÄT
BERGAKADEMIE FREIBERG
The University of Resources. Since 1765.

Evolution of Particle Morphology during Char Conversion Processes Applied for the CFD Modeling of an Entrained-Flow Gasifier

By the Faculty of Mechanical, Process and Energy Engineering
of the Technische Universität Bergakademie Freiberg

approved

Thesis

to attain the academic degree of

Doktor-Ingenieur
(Dr.-Ing.)

submitted by **M.Sc. Nguyen Cong Bang**

born on the August 23, 1984 in Haiphong, Vietnam

Assessor: Prof. Dr.-Ing. Bernd Meyer, TU Bergakademie Freiberg
Priv.-Doz. Dr.-Ing. habil. Falah Alobaid, TU Darmstadt

Date of the award: Freiberg, March 23, 2021

Versicherung

Hiermit versichere ich, dass ich die vorliegende Arbeit ohne unzulässige Hilfe Dritter und ohne Benutzung anderer als der angegebenen Hilfsmittel angefertigt habe; die aus fremden Quellen direkt oder indirekt übernommenen Gedanken sind als solche kenntlich gemacht.

Bei der Auswahl und Auswertung des Materials sowie bei der Herstellung des Manuskripts habe ich Unterstützungsleistungen von folgenden Personen erhalten:

- Prof. Dr.-Ing. Bernd Meyer
- PD Dr.-Ing. habil. Andreas Richter

Weitere Personen waren an der Abfassung der vorliegenden Arbeit nicht beteiligt.

Die Hilfe eines Promotionsberaters habe ich nicht in Anspruch genommen. Weitere Personen haben von mir keine geldwerten Leistungen für Arbeiten erhalten, die nicht als solche kenntlich gemacht worden sind. Die Arbeit wurde bisher weder im Inland noch im Ausland in gleicher oder ähnlicher Form einer anderen Prüfungsbehörde vorgelegt.

23. März 2021 M.Sc. Nguyen Cong Bang

Declaration

I hereby declare that I completed this work without any improper help from a third party and without using any aids other than those cited. All ideas derived directly or indirectly from other sources are identified as such.

In the selection and use of materials and in the writing of the manuscript I received support from the following persons:

- Prof. Dr.-Ing. Bernd Meyer
- PD Dr.-Ing. habil. Andreas Richter

Persons other than those above did not contribute to the writing of this thesis.

I did not seek the help of a professional doctorate-consultant. Only those persons identified as having done so received any financial payment from me for any work done for me. This thesis has not previously been published in the same or a similar form in Germany or abroad.

March 23, 2021 M.Sc. Nguyen Cong Bang

Acknowledgments

First, I would like to thank my first supervisor, Prof. Dr.-Ing. Bernd Meyer, who allowed me to study and do scientific research at the Institute of Energy Process Engineering and Chemical Engineering, TU Bergakademie Freiberg, Germany. I wish to express gratitude to my direct supervisor, PD Dr.-Ing. habil. Andreas Richter, who guides me in my scientific research. With his intensive support and useful advice, I achieved the goal of my doctoral project. Above all, the most valuable thing I have learned from him is a professional approach to scientific investigation.

I want to thank my colleague, Mathias Hartwich, who readily helped me solve daily problems with enthusiasm, friendliness and openness. Many thanks to Johannes Scherer, who helped me edit the original draft of my scientific articles. Sincere thanks also to Dr. Sebastian Kriebitzsch, who wrote the first version of the program for the surface reaction rate, and Claudia Arnold, who wrote the first version of the code for a dynamic mesh. Based on this, I solved part of the goal of my doctoral thesis.

I would like to thank the Vietnamese government for funding the scholarship during my four-year study in Germany, and the Hanoi University of Science and Technology for encouraging me in this doctoral program. I would like to thank Prof. Mai Xuan Ky, who introduced me to Germany for my doctorate.

First and foremost, I owe thanks to my mother, father, and siblings for their unconditional love. I wish to express special gratitude to my beloved wife, Nguyen Ngoc Mai, and our lovely daughter, Nguyen Mai Phuong, for their love, understanding, and encouragement during the years that I have been away from home. Without their support, I would not be able to achieve my success.

Contents

List of Figures

List of Tables

Nomenclature

Latin letters

$\dot{m}$	Mass flow rate	kg/s
$\dot{m}''$	Specific mass flow rate	kg/(m^2 s)
$\vec{F}$	Force	N/kg
$\vec{F}_S$	Momentum source	N/(m^3 s)
$\vec{n}$	Normal vector	–
a	Absorption coefficient	–
a_p	Particle equivalent absorption coefficient	–
A_{int}	Internal reaction surface	m^2
A_{pn}	Projected particle area	m^2
A_p	Outer reaction surface	m^2
A_{ta}	Annealing pre-exponential factor	1/s
a_{tf}	Total force except drag	N/kg
C_1	Diffusion rate constant	s/K$^{0.75}$
C_2	Inertial coefficient	–
C_ξ	Volume fraction constant	–
c_d	Drag coefficient	–
C_L	Input parameter of Discrete Random Walk Model	–
C_m	Thermophoretic force constant	–
C_s	Thermophoretic force constant	–
C_t	Thermophoretic force constant	–
C_{τ^*}	Time scale constant	–
C_{sw}	Swelling factor	–
D	Species diffusion coefficient in a mixture	m^2/s
d	Diameter	m
D_0	Diffusion rate coefficient through gas film	s/m
D_a	Diffusion rate coefficient through ash layer	s/m

D_h	Hydraulic diameter	m
D_p	Characteristic particle diameter	m
D_{th}	Thermophoretic force coefficient	–
E_a	Activation energy	J/kmol
E_p	Particle equivalent emission	–
$E_{a,ta}$	Annealing activation energy	J/kmol
f_h	Fraction of heterogeneous reaction heat absorbed directly by particle	–
f_{pn}	Particle scattering factor	–
f_{pore}	Pore fraction	–
f_{ta}	Annealing factor	–
f_{vap}	Particle moisture fraction	kg/kg
f_{vol}	Particle volatile fraction	kg/kg
G	Incident radiation	W/m^2
G_S	Radiation source	W/m^3
h	Enthalpy	J/kg
H_S	Heat source	$J/(m^3\,s)$
h_{conv}	Convective heat transfer coefficient	$W/(m^2\,K)$
K	Species inhibition constant	var.
k	Turbulent kinetic energy	m^2/s^2
k_∞	Pre-exponential factor	var.
$k_{d,\infty}$	Deactivated pre-exponential factor	var.
k_{diff}	Film diffusion coefficient	m/s
k_{kin}	Kinetic rate coefficient	s/m
k_{ta}	Annealing coefficient	–
l	Longitudinal particle length	m
L_e	Eddy length scale	m
m	Mass	kg
M_S	Mass source	$kg/(m^3\,s)$
M_w	Molecular weight	kg/kmol
n	Reaction order	–
N_p	Number of particles	
n_T	Temperature exponent	–

N_{hom}	Number of chemical reactions	
n_{ind}	Refractive index	–
N_{sub}	Number of sub surfaces	–
p	Partial pressure	$\mathrm{N/m^2}$
P_m	Permeability coefficient	–
q_{rad}	Radiation flux	$\mathrm{W/m^3}$
R	Specific reaction rate	$\mathrm{kg/(m^2\,s)}$
R^2	Measure of goodness of fit	–
R_G	Gas constant	$\mathrm{kJ/(kmol\,K)}$
r_{ext}	Outer heterogeneous reaction rate	kg/s
r_{int}	Internal heterogeneous reaction rate	kg/s
S_m'''	Mass-specific surface area	$\mathrm{m^2/kg}$
S_V'''	Volume-specific surface area	$\mathrm{m^2/m^3}$
T	Temperature	K
t	Time	s
t^*	Non-dimensional reaction time	–
T_L	Lagrangian integral time	s
t_{cross}	Time for particle to cross eddy	s
u	Fluid velocity	m/s
u'	Velocity fluctuation	m/s
u_p	Particle velocity	m/s
V	Volume	$\mathrm{m^3}$
v'	Velocity fluctuation	m/s
w'	Velocity fluctuation	m/s
X	Conversion level	–
x_p	Particle position	–
Y	Species mass fraction	kg/kg
Y^*	Mass fraction in concept reactor	kg/kg
$Y_{p,d}$	Mass fraction of particle size distribution	kg/kg

Greek letters

α	Density exponent	–
α'	Essenhigh density exponent	–

β	Diameter exponent	–
χ	Density parameters	
ΔH_R	Heat of reaction	J/kg
Δt^*	Time to cross control volume	s
δ	Mean free path of fluid	m
ϵ	Turbulent kinetic dissipation rate	m^2/s^3
ϵ_{pn}	Particle emissivity	–
η	Effectiveness factor	–
$\eta^{'}$	Second effectiveness factor	–
Γ	Incident radiation coefficient	–
γ	Random Pore Model factor	–
λ	Thermal conductivity	$W/(m\,K)$
Λ_{max}	Maximal reactivity ratio	–
μ	Molecular viscosity	$N\,s/m^2$
ν	Reaction stoichiometry	–
Φ	Thiele modulus	–
ϕ	Particle sphericity	–
$\phi_\perp$	Particle crosswise sphericity	–
π	Pi number	
Ψ	Pore structure parameter	–
ρ	Density	kg/m^3
σ	Stefan-Boltzmann constant	$W/(m^2\,K^4)$
σ_p	Particle equivalent scattering factor	–
τ^*	Time scale of concept reactor	s
τ_e	Lifetime of the eddy	s
τ_{inter}	Time of interaction between particle and eddy	s
τ_{relax}	Particle relaxation time	s
τ_{tor}	Pore tortuosity	–
θ_b	Blowing factor	–
θ_g	CBK model empirical factor	–
θ_o	CBK model empirical factor	–
ε	Porosity	–

ς	Random number	–
ξ	Burning mode parameter	–
ξ^*	Length scale of concept reactor	m

Dimensionless numbers

Kn	Knudsen number
Nu	Nusselt number
Pr	Prandtl number
Re	Reynolds number
Sc	Schmidt number
Sh	Sherwood number

Indices

–	Mean value
0	Initial situation
∞	Conditions around particle
a	Ash
C	Carbon
c	Char
$cell$	Computational cell
$core$	Core
cv	Control volume
cy	Cylinder
d	Drag
dc	Double cone
$devol$	Devolatilization
eff	Effective
fg	Latent
g	Gas phase
$grav$	Gravity
het	Heterogeneous reaction
hom	Homogeneous reaction
hrz	Heterogeneous reaction zone
i	Species i

in	Inlet conditions
int	Intrinsic kinetics
j	Reaction j
k	Sub surface index
Kn	Knudsen
m	Mixture
max	Maximum
min	Minimum
n	n^{th} particle
op	Operation
other	Other
out	Outlet conditions
ox	Oxidant
p	Particle
pore	Pore
r	Reaction
rad	Radiative
ref	Reference
s	Outer surface conditions
sol	Solid phase
sph	Sphere
t	True
th	Thermophoretic

Acronyms

0D	Zero-Dimensional
2D	Two-Dimensional
3D	Three-Dimensional
CBK	Carbon Burnout Kinetics
CFD	Computational Fluid Dynamics
CSIRO	Commonwealth Scientific and Industrial Research Organization
DNS	Direct Numerical Simulation
DRW	Random Walk Model

EDC	Eddy Dissipation Concept
EFM	Effectiveness Factor Model
HITECOM	High-Temperature Conversion Optical Measurement
IGCC	Integrated Gasification Combined Cycle
LES	Large Eddy Simulation
OFM	One-Film Model
PEFR	Pressurized Entrained-Flow Reactor
PRM	Particle-Resolved Model
PZM	Porous Zone Model
RANS	Reynolds-Averaged Navier-Stokes
RPM	Random Pore Model
SCM	Shrinking Core Model
SDM	Shrinking Density Model
SNOR	Single Nth-Order Reaction
SPM	Shrinking Particle Model
TFM	Two-Film Model
UDFs	User-Defined Functions

Abstract

The Ph.D. thesis aims to develop a comprehensive modeling approach for partial oxidation technologies, focusing on the entrained-flow gasification process for converting coal and carbonaceous material, such as municipal waste, biomass, or recycled plastic into syngas. Since the entrained-flow gasification process is characterized by turbulent flow and multi-scale length and time, it is much more computational effort to solve all scales directly. Therefore, developing sub models is necessary for the CFD modeling of the entrained-flow gasification process. Among the key processes taking place inside an entrained-flow gasifier, the char conversion is the slowest process. Hence, it controls the performance and efficiency of the gasifier. For that reason, comprehensively understanding complex physical and chemical phenomena occurring during the conversion of a char particle is crucial to attain an optimal design of the entrained-flow gasifier.

Interpreting the morphology evolution of a char particle during char conversion process is the first part of the Ph.D thesis. Based on particle-resolved simulations, some aspects of the particle morphology are studied in detail. First, the particle shape development due to heterogeneous reactions taking place at the outer particle surface is investigated. As the particle shape is different for each types of feedstock fed the entrained-flow gasifier, spherical and several non-spherical char particles are considered to examine how their shape develops during the char conversion process. A CFD particle-resolved model combined with a dynamic mesh algorithm is applied to study changes in the particle shape. Based on tracked shapes, dynamic models for the drag coefficient and particle sphericity, which depend on the particle Reynolds number and char conversion level, are worked out. The dynamic drag model can be used to improve the accuracy of particle trajectories, hence the hydrodynamics calculation of the entrained-flow gasifier. Second, intraparticle phenomena are considered to study how the volume and density of a char particle evolve during the char conversion process. For that purpose, another CFD particle-resolved model is used to calculate the conversion process of char particles under different reaction conditions. As a result, the evolution of the particle diameter, density, and internal surface area are monitored over reaction time. Analyzing the numerical data obtained from the CFD particle-resolved simulations reveals advanced sub models for fundamental conversion parameters. The advanced sub models provide a further understanding of the particle morphology evolution during the char conversion process, and can be used to improve the accuracy of particle conversion models applied for the CFD modeling of the entrained-flow gasifier.

Improving the accuracy and reliability of the CFD modeling of the entrained-flow gasifier is the final part of the Ph.D. thesis. A particle sub model developed in combination with the advanced sub models describing the particle morphology evolution is carried out based on the CFD framework to simulate a pressurized entrained-flow gasifier. Experimental data are used to validate the sub models applied. The validation shows a good agreement between the CFD simulation and measurement data. Influences of the particle shape development, other particle sub models, and ash inhibition on CFD simulation results of the gasifier are studied and discussed in detail.

Zusammenfassung

Das Ziel der vorliegenden Dissertation ist die Entwicklung eines umfassenden CFD-Modells zur Modellierung von Partialoxidationsprozessen mit dem Schwerpunkt auf der Flugstromvergasung von Kohle und kohlenstoffhaltigen Einsatzstoffen wie Siedlungsabfälle, Biomassen oder Kunststoffabfälle. Da Flugstromprozesse durch turbulente Mischungsvorgänge und komplexe Reaktionsvorgänge charakterisiert sind, variieren charakteristische Längen- und Zeitskalen um mehrere Größenordnungen. Eine direkte Berechnung aller relevanten Skalenbereiche ist aufgrund des hohen Rechenaufwands nicht möglich, sodass der Einsatz von Submodellen notwendig ist. Zu den wichtigsten Teilprozessen zählen die heterogenen Reaktionen der Kokspartikel, da diese häufig langsam ablaufen und dadurch den Kohlenstoffumsetzungsgrad sowie den Gesamtwirkungsgrad begrenzen. Aus diesem Grund ist ein umfassendes Verständnis der komplexen physikalischen und chemischen Phänomene, die bei der Umwandlung eines Kokspartikels auftreten, von entscheidender Bedeutung für die Optimierung von Flugstromvergasungsprozessen und die Entwicklung neuartiger Vergaserdesigns mit hoher Leistung und Effizienz.

Im ersten Teil dieser Arbeit wird die Entwicklung der Partikelmorphologie beim Koksumsatz untersucht. Dazu werden partikelaufgelöste Simulationen durchgeführt und unterschiedliche Aspekte bei der Änderung der Partikelmorphologie detailliert betrachtet. Zunächst wird die Entwicklung der Partikelform aufgrund heterogener Reaktionen untersucht. Da die Partikelform für die Einsatzstoffe jedes Flugstromvergasers unterschiedlich ist, werden sowohl kugelförmige als auch mehrere nicht-kugelförmige Kokspartikel betrachtet. Hier kommt ein CFD-Modell in Kombination mit einer dynamischen Gittergenerierung zum Einsatz. Basierend auf der Änderung der Partikelform werden neue Korrelationen für die Sphärizität und den Widerstandskoeffizienten der Partikel abgeleitet, die von der Reynolds-Zahl und dem Kohlenstoffumsetzungsgrad abhängen. Die resultierenden Korrelationen verbessern die Genauigkeit der berechneten Partikeltrajektorien und damit die hydrodynamische Berechnung der Flugstromvergaser. Des Weiteren werden Transportvorgänge innerhalb des Partikels berücksichtigt, um die Veränderung des Partikelvolumens und der Partikeldichte während des Umsatzes abzubilden. Zu diesem Zweck wird eine weitere CFD-Modell mit einem porösen Medium verwendet, um den Koksumsatz unter verschiedenen Reaktionsbedingungen zu modellieren. Basierend auf der Entwicklung des Partikeldurchmessers, der Dichte und der inneren Struktur des Partikels während der Reaktion werden neue Korrelationen für grundlegende Modellparameter entwickelt, die eine Verbesserung gegenüber den herkömmlichen und in der Literatur weit verbreiteten Kohleumwandlungsmodellen darstellen.

Ein weiterer Teil der Arbeit behandelt den Einsatz der entwickelten Teilmodelle zur Modellierung eines Vergasungsprozesses und die Analyse der Genauigkeit und der Zuverlässigkeit der Partikelmodelle. Dafür wird ein hybrides Partikelmodell in Kombination mit den resultierenden Korrelationen für die Entwicklung der Partikelmorphologie in einen bestehenden CFD-Löser implementiert und ein druckbeladener Flugstromreaktor modelliert. Die numerischen Ergebnisse zeigen eine gute Übereinstimmung mit den experimentellen Daten, sodass die Gültigkeit und Genauigkeit des Konversionsmodells bestätigt wird. Anschließend werden die Entwicklung der Partikelform, der Effekt der Ascheinhibierung und die heterogenen Reaktionen in unterschiedlichen Reaktionsregimen untersucht und der Einfluss des Konversionsmodells auf die Gesamtreaktorberechnung diskutiert.

1 Introduction

1.1 Entrained-Flow Gasification

Gasification is the thermochemical conversion of a carbonaceous feedstock using different gasification agents, such as air, O_2, H_2O, CO_2, H_2, and a mixture thereof, into synthesis gas with a useful chemical heating value. The synthesis gas, mainly consisting of H_2 and CO, can be applied for various purposes, e.g. it can be used for the production of valuable chemicals such as ammonia, methanol, acetic acid and liquid hydrocarbons, or it can be directly burnt in the gas turbine of the integrated gasification combined cycle (IGCC) power plants [1].

Entrained-flow gasification is most widely used in the solid fuel chemical industry since it can provide a high loading throughput at high temperature with high gasification efficiency. Therefore, the entrained-flow gasifier has become a dominant concept for syngas production because of its advantages, such as almost complete carbon conversion, tar-free raw gas, high specific coal throughput, low sensitivity to coal rank [1].

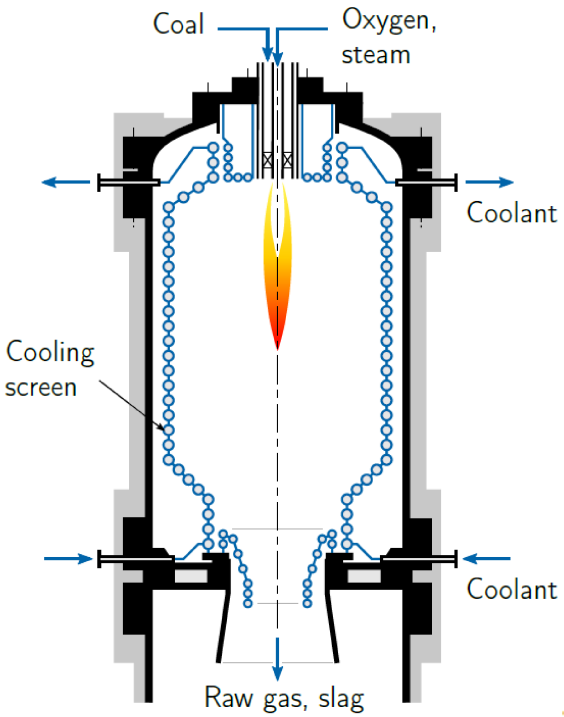

Fig. 1.1: Diagram of an entrained-flow gasifier with a cooling screen, GSP type entrained-flow gasifier [2]

For example, Figure 1.1 illustrates the configuration of a single-stage downdraft entrained-flow gasifier [2]. The GSP type entrained-flow gasifier is a top-fired gasifier with a single central burner. The ground coal enters the gasifier as dry feed or slurry. The fuel stream is brought into contact with oxygen and steam as gasification agents in a downward co-current flow at high pressures and temperatures above the ash melting point. The reaction chamber is equipped with a cooling screen to protect the gasifier wall from overheating. Most of the ash

material in the form of liquid slag locates on the cooling screen, flows down to the bottom of reaction chamber due to gravity, and leaves the gasifier at a common outlet. The granulated slag is collected in a water bath at the bottom of the vessel and is discharged periodically. The remaining ash is transported as fly ash by the syngas.

The chemical reactions and gas flow conditions taking place inside entrained-flow gasifiers are quite complex. The reacting gas flow is characterized by a fully turbulent flow. In addition, the solid fuel particles undergo a complex morphology transformation during a series of process such as heating, drying, pyrolysis and char conversion. The interaction between the gas flow and solid fuel particles dominates the performance and efficiency of entrained-flow gasifiers, and still is not fully understood. This limits the further optimization of the gasifier design. Therefore, a further investigation to clarify the evolution of particle morphology and its influence on heterogeneous processes plays an important role in the development of entrained-flow gasifiers with the purpose of increasing efficiency and adapting to low-grade feedstock [3]. The characteristics of hydrodynamics and reactions inside entrained-flow gasifiers are difficult to obtain using experimental tests. To overcome this challenge, the modeling of entrained-flow gasifers and numerical simulations allow us to investigate the gasifier characteristics in more detail with a massive volume of accessible data. The result is a reduction of experimental efforts and time expenditure for the optimal design of entrained-flow gasifiers.

1.2 Numerical Modeling of Entrained-Flow Gasifiers

The gasification process is characterized by a complex interplay between the gas phase and dispersed phase (particles) based on the principles of physical and chemical phenomena. These principles are described mathematically via conservation equations of mass, momentum, and energy. ANSYS-Fluent®, which combines the rule of fluid dynamics and chemical reactions, has become a well-established tool for understanding and optimizing the complex reactive multiphase flow inside entrained-flow gasifiers. In particular, computational fluid dynamics (CFD) simulation now plays an essential role in the design of advanced gasifiers.

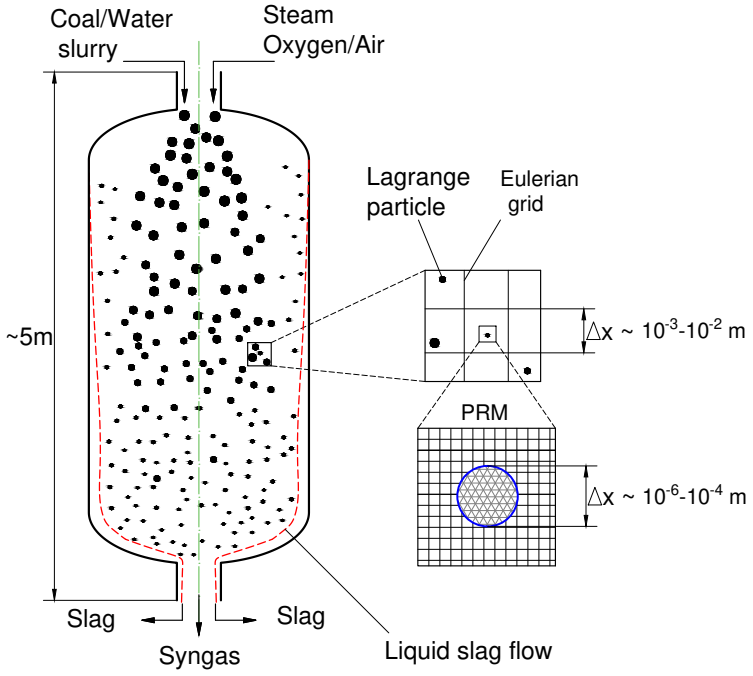

Fig. 1.2: Multiscale processes inside an entrained-flow gasifier [4]

As shown in Figure 1.2, the entrained-flow gasification process is inherently turbulent and multiscale due to the major difference in time and length scale, from several meters for the reactor to several micrometers for the particle [4]. In theory, it is possible to describe mathematically the processes occurring inside a gasifier at any length and time scale based on the principle of conservation of mass, momentum, and energy. However, solving the conservation equation system at all scales poses a challenge as it requires much more computational effort and time. Usually, this is not possible because of the lack of computing resources. For engineering applications, to overcome this challenge reliable sub models must be developed to describe complex physical and chemical phenomena at limited scales.

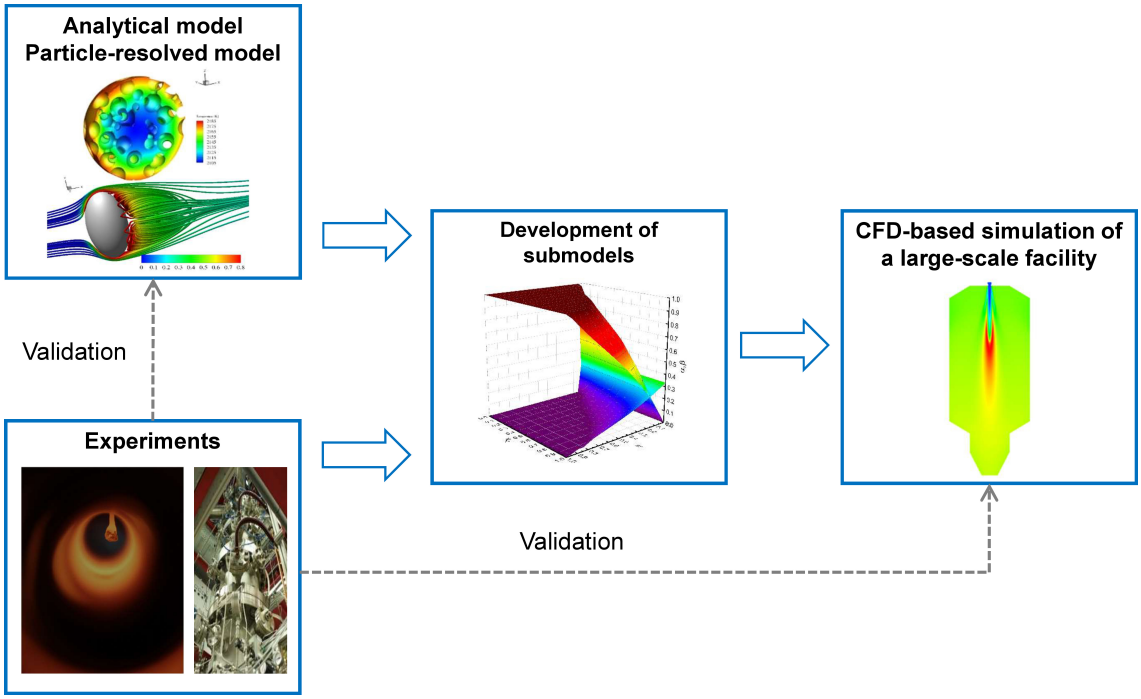

Fig. 1.3: Principle scheme of the process from the particle model to the CFD modeling of a large-scale facility

In particular, the sub models can be derived from: (1) the experiment with modern equipment and demanding techniques, (2) the analytical model, or (3) the particle-resolved model (PRM). The principle scheme of the development process from the particle model to the CFD modeling of a large-scale facility is shown in Figure 1.3. The PRM is cheaper and more flexible than the experimental tests. It can generate a massive volume of accessible data, but requires the complex conversion processes to be described in detail. The analytical model, a straightforward approach with simplified assumptions, is used to introducing new sub models. However, the sub models obtained from the analytical model should be improved by the PRM. The sub models gained from the analysis of experimental data are only valid around the experimental conditions, whereas the sub models gained from the PRM are applicable to a wide range of operation conditions. Generally, the sub models should meet the following, e.g.

- Sub models must be fast, robust and easy to implement and run many times in the simulation until the macro-scale simulation converges.
- The reliability of sub models has to be carefully validated by comparison with experimental data.

The quality of CFD simulation results depends directly on the applied sub models' quality, e.g. for heating, drying, pyrolysis, and char conversion. Among the fundamental processes taking place in an entrained-flow gasifier, the char conversion process is the slowest. Therefore, the

quality of particle sub model for the char conversion process is crucial to predict the gasifier's overall carbon conversion accurately. The efficiency of an entrained-flow gasifier is determined by both the characteristics of the hydrodynamics of the gasifier and the heterogeneous reaction rate, which are governed by the evolution of the particle morphology. It is expensive to use sophisticated equipment to record the morphology evolution of a single particle during its conversion process, moreover it is impossible to measure or observe processes that take place inside a micrometer particle. To overcome this challenge, the goal of this Ph.D. thesis is to develop reliable sub models describing the particle morphology evolution during the char conversion process based on the PRM. The developed sub models are validated by experimental data of an entrained-flow gasifier at the laboratory scale.

1.3 Scope of the Work

Against this background, the Ph.D. thesis aims to study in detail the conversion process of char particles based on the PRM. The evolution of particle morphology is captured over the char conversion process. Based on the analysis of numerical data, new sub models for the drag coefficient and conversion parameters are introduced to improve the accuracy of a CFD-based simulation of entrained-flow gasifiers.

1.4 Overview of the Work

The Ph.D. thesis can be summarized as the follows.

Chapter 1 The principle of an entrained-flow gasifier is briefly introduced. The challenges in numerical modeling of entrained-flow gasifiers are considered, with emphasis on the role of the PRM in developing sub models for the CFD modeling of large entrained-flow gasifiers.

Chapter 2 An overview of single particle modeling is provided. Several standard particle sub models are presented. The drag coefficient and Nusselt number for tracking particles and calculating the heat transfer between the particle and gas phase are outlined. Finally, the internal structure of char particles after the pyrolysis process and models of the particle morphology evolution are described in detail.

Chapter 3 The theoretical basis for the modeling a dilute particle flow is presented, focusing on the particle motion and the interaction between the particle and the gas phase.

Chapter 4 The changes in the shape of spherical and non-spherical particles due to heterogeneous reactions are studied in detail. The particle shape is tracked with the carbon conversion. Based on tracked shapes, dynamic drag models are derived to improve the accuracy of particle trajectories in entrained-flow gasifiers.

Chapter 5 Intraparticle phenomena are investigated. As a result, the complex physical and chemical processes taking place around and inside a char particle are observed in detail. The development of the particle's morphology over conversion time is tracked. Numerical data obtained from the particle-resolved transient simulation are analyzed to reveal advanced correlations of fundamental parameters for the char conversion model.

Chapter 6 A comprehensive model of the char conversion in combination with the sub models developed in Chapters 4 and 5 is implemented in the CFD modeling of an entrained-flow gasifier. A comparison between numerical and experimental data reveals the accuracy of the developed sub models. The influence of particle shape development, other particle sub models and ash inhibition on the char conversion rate is also studied in detail.

Chapter 7 Main conclusions were drawn.

2 Overview of Single-Particle Modeling

With the increasing availability of high-performance computing resources and available software, it is becoming practicle to solve Navier-Stokes equations of a fluid flow incorporated with chemical reactions. Based on the CFD framework combined with chemical reaction mechanisms, interactions between a chemically reacting particle and fluid flow have been studied, interpreted, visualized and understood more further, which significantly help us with improving the efficiency of technological processes. This chapter offers an overview of recent works related to the modeling of single char particles, as widely applied for the numerical calculation and optimization of coal combustion and gasification processes.

2.1 Non-Reacting Particle-Resolved Model

One aim of non-reacting particle-resolved model is to focus on physical phenomena taking place around a particle, such as heat and mass transfer, and the flow hydrodynamics. The accuracy of correlations related to the drag, heat and the mass transfer coefficient between the particle and fluid flow can be improved based on numerical data obtained from the particle-resolved model. The coefficients play important roles in calculating the heat flux exchanged between the particle and fluid flow, hence the particle temperature, and estimating particle trajectories, thus the particle residence time inside a pulverized coal combustor/gasifier. Recent works by Richter et al. [5] and Wittig et al. [6] are typical investigations on the drag coefficient and Nusselt number using high-quality CFD simulations for non-spherical particles, and spherical porous particles in laminar flow conditions.

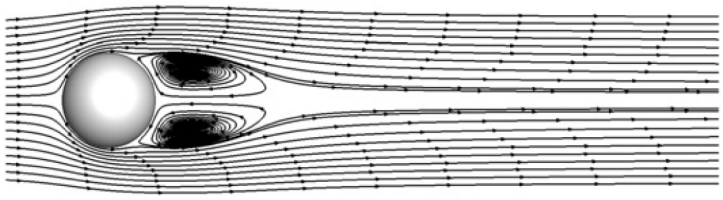

(a) spherical particle

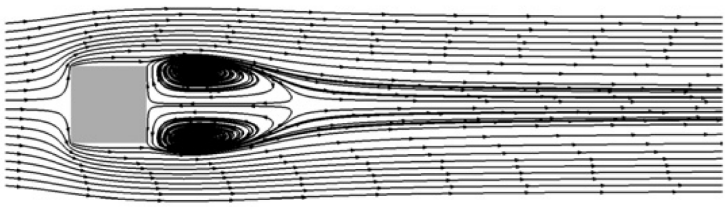

(b) cubic particle

Fig. 2.1: Flow patterns around non-reacting particles at Re=250 [5]

Figure 2.1 shows three-dimensional (3D) flow patterns around a cubic, and spherical particle [5]. The air flow with a constant temperature of 25 °C passes over the particles from left to right at the Reynolds number of 250. The particle temperature remains a constant value of 125 °C. It can be seen that the shape of the boundary layer around the particle depends on

its shape directly. This leads to that the drag, heat and mass transfer coefficient are governed by the particle shape. Therefore, effects of the shape must be considered in standard particle sub models, which are based on assumptions the particle to be non-porous and spherical shape, and are widely used for the CFD modeling of entrained-flow processes, to enhance the reliability of simulation results.

2.2 Chemically Reacting Particle-Resolved Model

A chemically reacting particle was first modeled based on analytical approaches. Nusselt introduced an analytical one-film model (OFM) in 1924 [7], and in 1931 Burke and Schuman improved on Nusselt's mode, presenting a two-film model (TFM) [8]. Nowadays, analytical solutions of those models are used to compared with numerical data obtained from computational calculations as the first step of validation process [9]. With the development of high-performance computing resources, the particle-resolved CFD simulation has been considered as a numerical experiment to interpret complex physical and chemical processes taking place in the vicinity and interior of a chemically reacting particle, where experimental measurements usually are impossible to carry out [4]. The particle-resolved CFD simulation of a chemically reacting particle is carried out following either the steady-state approach or the transient approach, depending on the purposes of investigations.

The steady-state CFD simulation has been widely used to study the structure of the boundary layer and the distribution of temperature and species around a particle, and the performance of a chemical reaction mechanism [10]. In addition, the influence of the Stefan flow, a mass flow from the outer particle surface due to heterogeneous reactions, on the process of heat and mass transfer can be studied in detail using the steady-state CFD simulation. The works by Richter et al. [11–13], Safronov et al. [14] and Kriebitzsch et al. [15] are representative examples of the steady-state CFD simulation of single reacting particles.

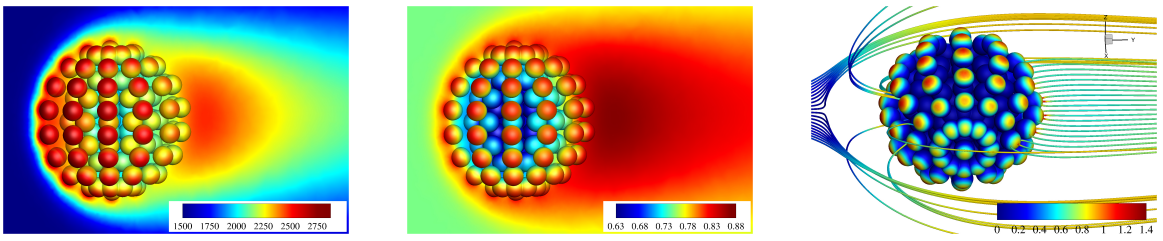

(a) temperature, K (b) Y_{CO_2}, kg/kg (c) Stefan flow, m/s

Fig. 2.2: Steady-state CFD simulation of a 200 µm chemically reacting porous carbon particle in a hot O_2/CO_2 atmosphere [12]

Figure 2.2 shows 3D distributions of the temperature, carbon dioxide mass fraction and Stefan flow obtained from a steady-state CFD simulation of a reacting porous carbon particle in a hot O_2/CO_2 atmosphere at Re=100, referred to the work by Richter et al. in [12]. It can be seen that the particle temperature, shown as Figure 2.2a, and the distribution of reactant species, such as CO_2 shown as Figure 2.2b, inside the reacting porous carbon particle are characterized by gradient distributions. However, the effect of these gradients is usually ignored in the estimation of the carbon consumption rate of standard particle sub models. In addition, the Stefan flow, shown as Figure 2.2c, features a velocity with the same magnitude as the ambient flow velocity. The Stefan flow affects the particle's boundary layer characteristics, which significantly influence the mass and heat transfer coefficients, especially at high-temperature conditions. Therefore, the effect of the Stefan flow on the estimation of heterogeneous reaction rates should be considered in particle sub models.

The transient CFD simulation allows us to track the morphology evolution of a chemically reacting particle, such as the shape, size, density, and pore structure, during its transformation process. Numerical data obtained from the transient CFD simulation can be analyzed to reveal new correlations describing changes in the particle morphology, which are not easily attained from experimental tests. The understanding of the particle morphology evolution during the conversion process plays a vital role in improving the reliability and accuracy of CFD simulation results of particulate flow reactors, e.g. entrained-flow gasifiers. Works devoted to the CFD transient approach are given in [16–20].

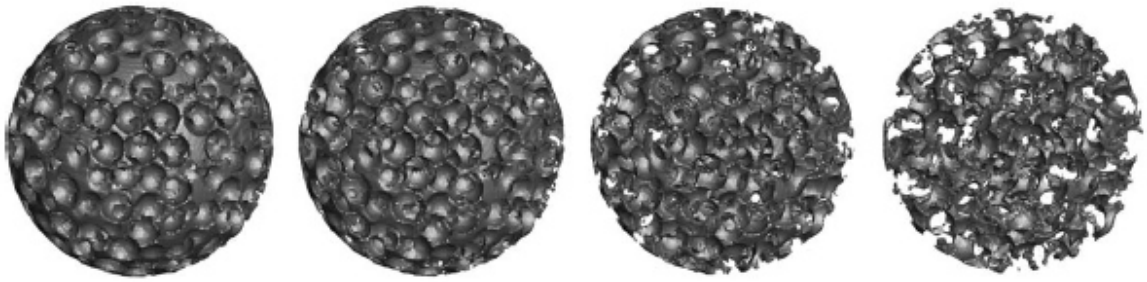

Fig. 2.3: The pore structure development of a porous carbon particle reacting with a mixture of CO_2 and N_2 (Y_{CO_2}=0.9) under atmosphere pressure condition and gas temperature T_∞=1200 K. Carbon conversion level from left to right: 0, 25, 50 and 75 % [16]

Figure 2.3 from the results given by Wittig et al. [16] shows the pore structure development of a porous carbon particle with an initial porosity of 0.7 reacting with a mixture of CO_2 and N_2, Y_{CO_2}=0.9, at a total pressure of 101.325 kPa and gas temperature T_∞=1200 K. Only, Boudouard reaction, $C + CO_2 \longrightarrow 2\,CO$, takes place. Under such conditions, the heterogeneous reaction occurs inside the porous particle in a kinetically controlled regime. It is clear that the particle's internal structure continuously changes during the carbon conversion process, and the particle fragmentation occurs when the carbon conversion reaches a certain level. In addition, works by Dierich et al. [17], Beckmann et al. [18] and Nguyen et al. [20] show that the particle shape, size and density change simultaneously over the conversion time in most operating conditions. The changes in the particle morphology need to be clarified and taken into account for the calculation of carbon consumption rate of particle sub models.

2.3 Particle Sub Model for Char Conversion Process

Since char particles are inherently porous, the carbon consumption rate is governed by the interplay of mass transport and char reactivity. The main processes of a gas-char particle reaction system can be described as (i) diffusion of gaseous species from the bulk to the outer particle surface, (ii) species diffusion inside the porous structure of the particle, (iii) heterogeneous reactions including adsorption, surface reaction, and desorption, and (iv) re-diffusion of species to the bulk phase [21, 22]. Usually, one of the steps is considerably slower than the rest, and becomes a rate-limiting step that controls the overall reaction rate of the gas-char particle system [13, 23]. Based on which is the controlling process, a gas-char particle reaction system is classified into three regimes [12], as shown in Figure 2.4.

Regime I Regime I, known as the kinetically controlled regime, exists at low ambient temperatures. The limiting step is heterogeneous reactions on the pore surface. As there is no pore resistance, and the concentration of the reactants is uniform over the particle volume and equal to that on the outer particle surface, the available surface on which heterogeneous reactions take place is utilized extremely efficiently. The particle size and shape remain its

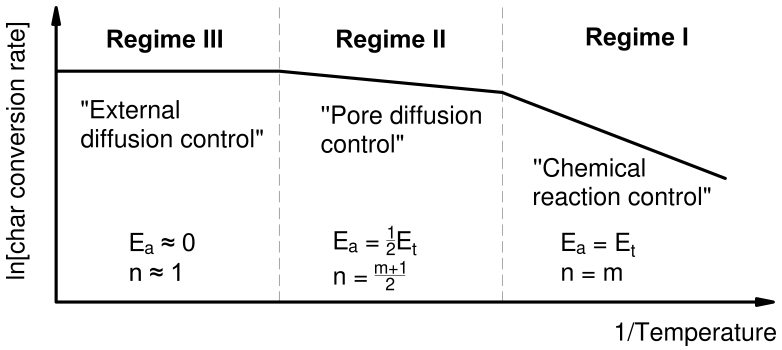

Fig. 2.4: Reaction regimes of the gas-particle reaction system [24]

original, while the carbon density is reduced in maximum during the char conversion process. The development of specific surface area is described using the Random Pore Model.

Regime II Regime II, called the pore-diffusion regime, is characterized by the reacting volume being shifted to the outer particle surface. Chemical reactions and the diffusion of reactants through the pores are of the same order of magnitude and influence the reaction rate. The concentration of reacting gaseous species decreases from the particle surface to the particle center. Therefore, in Regime II, the utilization of the available reaction surface is less efficient than that in Regime I. The morphology of a particle, such as its shape, size, carbon density and particle density, is changed during the char conversion process.

Regime III Regime III, known as the outer diffusion-controlled regime, occurs when the ambient temperature is high enough for the gaseous reactants to react with the solid carbon on the pore surface at an extremely fast rate. The zone, where heterogeneous reactions occur, is mostly located on the outer particle surface. Therefore, the particle size decreases due to carbon consumption while the carbon density and the particle's specific surface area remain constant. The particle density increases since an ash layer is formed, replacing the consumed particle volume.

The correct estimation of the reaction regime of the gas-char particle reaction system plays a vital role in selecting a suitable particle sub model for CFD modeling entrained-flow gasifiers. It is also important to analyze experimental data to gain kinetic parameters such as pre-exponential factors, activation energy and the reaction order. For example, in Regime II, the observed activation energy is equal to half of the real activation energy, while the experimental reaction order n and actual reaction order m are related as n=(m+1)/2.

Due to the lack of computational sources, usually it is impossible to apply directly detailed models of a chemically reacting particle to the CFD modeling of large-scale entrained-flow gasifiers with an acceptable simulation time [25]. For that reason, practical engineering applications require the development of particle sub models, which can be compiled with the CFD code to carry out the CFD simulation of reacting multi-phase flows inside large-scale entrained-flow gasifiers with the time consuming acceptable. The particle sub model is named the sub-gird model or 0D model. The following sections outline standard particle sub models that have been widely applied for the CFD modeling of entrained-flow processes.

2.3.1 The Diffusion-Limited Model

The diffusion-limited model introduced by Baum and Street [26] assumes that the heterogeneous reaction rate is very fast. The kinetic contribution to the overall rate is ignored. Hence, the rate of the gas-char particle reaction system is determined by the rate of the species diffusion from the gas phase to the outer particle surface. The carbon consumption rate $R_{het,j}$ due to

the heterogeneous reaction j is calculated by the following equation

$$R_{het,j} = \frac{4 D_{ox,m} Y_{ox} T_\infty \rho_g}{d_p \nu_{ox,j} (T_\infty + T_p)} \tag{2.1}$$

where d_p is the particle diameter, $D_{ox,m}$ denotes the diffusion coefficient of oxidant in the mixture, Y_{ox} stands for the local mass fraction of oxidant in the gas, ρ_g is the gas density and $\nu_{ox,j}$ is the reaction stoichiometry. The diffusion-limited model should correspond to Regime III. However, it assumes that the particle diameter is unchanged and the particle density is reduced during the char conversion process [27], which is inconsistent with the characteristics of Regime III. As the diffusion limits the rate of heterogeneous reactions, the diffusion-limited model is suitable for char conversion at high temperatures.

2.3.2 The Kinetic/Diffusion Model

The kinetic/diffusion model [26, 28] assumes that the influences of the diffusion rate and heterogeneous reaction rate on the overall rate are of the same magnitude. The following equation calculates the carbon consumption rate due to heterogeneous reaction j with a reaction order of 1.0

$$R_{het,j} = \frac{\rho_g R_G T_\infty Y_{ox}}{M_{w,ox}} \frac{D_0 \, k_{kin,j}}{D_0 + k_{kin,j}} \tag{2.2}$$

where R_G is the gas constant, $M_{w,ox}$ denotes the molecular weight of oxidant and D_0 stands for the diffusion rate coefficient in s/m, expressed in the following equation

$$D_0 = C_1 \frac{[(T_p + T_\infty)/2]^{0.75}}{d_p} \tag{2.3}$$

where C_1 is the mass diffusion rate constant, an input parameter of the model which is set to $10^{-12}\,\mathrm{s/K^{0,75}}$ by default in ANSYS-Fluent®. The reaction rate coefficient $k_{kin,j}$ in s/m is described using the Arrhenius equation as through

$$k_{kin,j} = k_{\infty,j} T_p^{n_T} \, e^{-\frac{E_{a,j}}{R_G T_p}} \tag{2.4}$$

where $k_{\infty,j}$ is the pre-exponential factor, n_T is the temperature exponent and $E_{a,j}$ is the activation energy. However, the model assumes that the available surface for heterogeneous reactions is only the outer particle surface, which is not suitable for a porous char particle, and the particle size remains constant while the particle density is allowed to decrease during the char conversion process. The kinetic/diffusion model is valid for char conversion under medium temperature conditions. Oxidant species can be O_2, H_2O and CO_2.

2.3.3 The Multiple Surface Reaction Model

The multiple surface reaction model, the most frequently applied approach and one which is available in ANSYS-Fluent®, is discussed in detail by Smith [29]. The particle surface where the heterogeneous reactions take place is considered as a wall surface on which carbon, as a reactant species, is depleted in terms of its content during the conversion process. The following equation calculates the carbon consumption rate due to reaction j

$$R_{het,j} = \eta_j Y_C \, R_{het,j,s} \tag{2.5}$$

where Y_C is the carbon mass fraction of the particle; η_j is the effectiveness factor, set to 1 by default and $R_{het,j,s}$ denotes the rate of the particle surface reaction j, which is defined in an iterative way

$$R_{het,j,s} = k_{kin} \Big(p_{ox} - \frac{R_{het,j,s}}{D_0} \Big)^{n_j} \tag{2.6}$$

where k_{kin} is the rate coefficient of reaction j, calculated by Eq. (2.4), p_{ox} stands for the bulk partial pressure of the oxidant and n_j is the order of reaction j.

2.3.4 The Shrinking Core Model

The shrinking core model (SCM) was developed by Wen and Chaung [30]. The char particle is assumed to compose an ash layer surrounding an un-reacted rich-carbon core. In addition to the Arrhenius kinetics and diffusion effects, diffusion through the surrounding ash layer is taken into account for the model. As the heterogeneous reactions occur only on the core's outer surface, the particle diameter decreases over conversion time. The following equation calculates the carbon consumption rate $R_{het,j}$ due to reaction j

$$R_{het,j} = \frac{p_{ox}}{\frac{1}{D_0} + \frac{1}{k_{kin}\left(\frac{d_p}{d_{p,0}}\right)^2} + \frac{1}{D_a}\left(\frac{d_{p,0}}{d_p} - 1\right)} \tag{2.7}$$

where d_p and $d_{p,0}$ are the instantaneous and original radius of an ash-char particle, respectively, and D_a is the effective diffusion rate coefficient through the ash layer, $D_a = \varepsilon_p^{2.5} D_0$. The SCM model is applied well for the gas-particle reaction system in very high-temperature conditions. Under such conditions, the mass transfer to the particle's outer surface is the rate-limiting step [31]. The shrinking core model is suitable for applying to the conversion of coal char with a high ash content under high temperature conditions.

2.3.5 The Carbon Burnout Kinetics Model

The Carbon Burnout Kinetics (CBK) model, a model with a detailed mechanism of reactions, was originally developed by Hurt et al. at Sandia National Laboratories and later at Brown University. Today, it is recognized as one of the most advanced models available and has been applied for modeling coal combustors over more than a decade [32]. Variants of the CBK model have been developed. The latest versions are CBK/E [33] for oxidation and CBK/G for gasification [34].

The CBK/G model takes into account the char gasification process based on an eight-step Langmuir–Hinshelwood kinetic formulation. Accompanied by a random pore model evolution of the intrinsic particle surface, pore diffusion, single film diffusion, thermal annealing, and ash inhibition, the CBK/G model can model the low rate in the latter part of the char conversion process. The models' kinetic parameters are determined based on a rank coal correlation, which is drawn by analyzing several experimental databases on the drop tube reactor under different process conditions. However, the direct use of CBK/G for CFD modeling a coal gasification reactor is generally too computationally expensive. For that reason, a simplified Single Nth-Order Reaction (SNOR) model, which takes into account inhibition by CO and H_2 and the structural evolution of char particles during the conversion process, was proposed by Liu and Niksa [34]. The rates of the reaction of char with CO_2, H_2O, H_2 and O_2 are expressed as

$$R_{C-CO_2} = \theta_g(X_c)\frac{k_{kin,CO_2} \cdot p_{CO_2,s}^{n_{CO_2,s}}}{1 + K_{CO} p_{CO_2,s}} \tag{2.8}$$

$$R_{C-H_2O} = \theta_g(X_c)\frac{k_{kin,H_2O} \cdot p_{H_2O,s}^{n_{H_2O,s}}}{1 + K_{H_2} p_{H_2O,s}} \tag{2.9}$$

$$R_{C-H_2} = \theta_g(X_c) k_{kin,H_2} \cdot p_{H_2,s}^{n_{H_2,s}} \tag{2.10}$$

$$R_{C-O_2} = \theta_o(X_c) k_{kin,O_2} \cdot p_{O_2,s}^{n_{O_2,s}} \tag{2.11}$$

where K_{CO}, K_{H_2} is the rate constants accounting for the inhibition due to CO and H_2, and $\theta_g(X_c)$ and $\theta_o(X_c)$ are an empirical factor accounting for the thermal annealing, random pore evolution and changes in the particle density. There are two main steps for applying the SNOR model for CFD modeling an entrained flow gasifier. First, the CBK/G model's kinetic parameters are determined based on the characteristics of the coal and the experimental data of the coal gasification. Second, the kinetic parameters of the SNOR are calibrated by the CBK/G model obtained from the first step. However, it should be noted that agreement between the CBK/G and the SNOR can only be obtained for the calibration conditions. The works by Richter et al. [13] and Vascellari et al. [21] are representative examples of the employment of CBK/G and SNOR for modeling the entrained-flow gasifiers.

2.3.6 The Intrinsic Model

Like the kinetic/diffusion model, the intrinsic model assumes that the overall carbon consumption rate for a gas-particle reaction system includes the effects of both the bulk diffusion rate and the effective reaction rate. However, the effective reaction rate is considered to be a result of the interplay between the pore diffusion and the chemical reaction occurring at the pore wall. This is important, as the surface area of pores and their diffusion effects have significant impacts on the overall carbon consumption rate in Regime II. The typical approach of the intrinsic model is based on the effectiveness factor, a ratio of the actual carbon conversion rate to the rate as if there was no pore diffusion effect [35, 36]. The effective reaction rate $R_{het,j}$ is determined in the equation

$$R_{het,j} = \eta_j \frac{|\nu_{ox,j}| M_{w,ox}}{|\nu_{C,j}| M_{w,C}} k_{j\infty} \exp\left\{-\frac{E_{aj}}{R_G\, T_p}\right\} p_{ox,s}^{n_j} \tag{2.12}$$

where $\nu_{ox,j}$ is the oxidant stoichiometric coefficient, $M_{w,C}$ denotes the carbon molecular weight and $p_{ox,s}$ is the partial pressure of the oxidant on the outer particle surface. As an analytical solution for the reaction-diffusion equation of the oxidant based on a spherical shape, the effectiveness factor is a function of the Thiele modulus Φ_j [27, 35] and is expressed as

$$\eta_j = \frac{1}{\Phi_j}\left(\frac{1}{\tanh(\,3\Phi_j)} - \frac{1}{3\Phi_j}\right) \tag{2.13}$$

The Thiele modulus is calculated by the equation

$$\Phi_j = \frac{d_p}{6}\sqrt{\frac{n_j+1}{2}\frac{|\nu_{ox,j}|\; S_V'''\, R_G\, T_p\, k_{j\infty} \exp\left\{-\frac{E_{aj}}{R_G\, T_P}\right\} p_{ox,s}^{n_j-1}}{M_{w,C}\, D_{ox,eff}}} \tag{2.14}$$

where $D_{ox,eff}$ denotes the effective diffusivity of the oxidant. The effective diffusivity is expressed as [18]

$$D_{ox,eff} = \frac{\varepsilon_p}{\tau_{tor}}\left(\frac{1}{D_{ox,Kn}} + \frac{1}{D_{ox,m}}\right)^{-1} \tag{2.15}$$

where ε_p is the particle porosity, τ_{tor} is the tortuosity of the pores, $D_{ox,Kn}$ denotes the Knudsen diffusion coefficient and $D_{ox,m}$ stands for the molecular diffusion coefficient. The Knudsen diffusion coefficient is

$$D_{ox,Kn} = \frac{1}{3}\bar{d}_{pore}\sqrt{\frac{8R_G\, T_P}{\pi\, M_{w,ox}}} \tag{2.16}$$

where $\bar{d}_{pore}$ is the mean pore diameter. The mean pore diameter is calculated by

$$\bar{d}_{pore} = 4\varepsilon_p \frac{\sqrt{\tau_{tor}}}{S_V'''} \tag{2.17}$$

Some studies express effective diffusivity by neglecting the influence of micro-porosity [37].

$$D_{ox,eff} = \varepsilon_p \frac{f_{pore}}{\tau} D_{ox,m} \tag{2.18}$$

where f_{pore} is the fraction of total porosity in feeder pores. The ratio of f_{pore}/τ_{tor} can be determined by experiment for each type of coal char. There are many models for the ratio in the literature. For typical applications, the ratio is equal to ε_p hence $D_{ox,eff} = \varepsilon_p^2 D_{ox,m}$ [25].

From Eq. (2.12) and Eq. (2.14), it can clearly be seen that the partial pressure of the oxidant on the outer particle surface $p_{ox,s}$ is an unknown variable and should be determined to calculate the effective reaction rate of the reaction j. The balance between the mass flux of the oxidant from the gas phase to the outer particle surface by film diffusion and the mass of the oxidant consumed by the chemical reaction referred to the outer particle surface is expressed as Eq. (2.19), which is solved to determine the partial pressure of the oxidant on the outer particle surface $p_{ox,s}$.

$$\frac{k_{diff,ox} M_{w,ox}}{R_G \bar{T}} (p_{ox} - p_{ox,s}) = \eta_j S_V''' \frac{d_p}{6} \frac{M_{w,ox}|\nu_{ox,j}|}{M_{w,C}|\nu_{C,j}|} k_{j\infty} \exp\left\{-\frac{E_{aj}}{R_G T_p}\right\} p_{ox,s}^{n_j} \tag{2.19}$$

where $\bar{T}$ denotes the mean temperature of the particle and gas phase; $k_{diff,ox}$ is the film diffusion coefficient, calculated based on the Sherwood number Sh as

$$k_{diff,ox} = \frac{Sh\, D_{ox,m}}{d_p} \tag{2.20}$$

$$Sh = 2 + 0.6 Re^{\frac{1}{2}} Sc^{\frac{1}{3}} \tag{2.21}$$

where Sc is the Schmidt number.

The effective factor approaches zero at very high temperature conditions, where the intrinsic surface does not participate to the char consumption. Consequently, the char conversion rate calculated based on the intrinsic model reaches zero. This is a limitation of the intrinsic model. However, such conditions is suitable to apply the diffusion-limited model or the shrinking core model to calculate the char consumption rate.

2.4 Drag Coefficient and Nusselt Number

At entrained-flow conditions e.g. combustion and gasification, the particle trajectory is mainly driven by the drag force which arises to the relative motion between the spherical particle and gas phase, and calculated as [38].

$$|\vec{F}_d| = \frac{c_d \pi d_p^2 (u - u_p)^2}{8} \tag{2.22}$$

where d_p is particle diameter, u is the fluid phase velocity, u_p denotes the particle velocity, and c_d is drag coefficient. c_d depends on the particle Reynolds number Re, which is defined as follows

$$Re = \frac{\rho_g d_p |u - u_p|}{\mu} \tag{2.23}$$

where μ is the molecular viscosity of the fluid and ρ_g is gas density. On the other hand, the particle temperature results from the balance of convective and radiative heat transfer between the particle and surrounding gas and the heat released or absorbed by heterogeneous chemical reactions taking place in the particle. The radiative heat transfer coefficient depends on the radiative properties of the particle and the ambient gas, such as emission, absorption

and scatter, while the convective heat transfer coefficient h_{conv} relates to the Nusselt number, including the effect of the Stefan flow as the equation [39]

$$h_{conv} = \frac{Nu\lambda_g}{d_p} \tag{2.24}$$

The Stokes drag is applicable to the creeping flow regime (Stokes regime) with low particle Reynolds numbers ($Re \leq 1.0$). The drag coefficient for a spherical particle in Stokes regime is calculated by the following [38].

$$c_d = \frac{24}{Re} \tag{2.25}$$

Recently, Kriebitzsch et al. [15] used LES simulations for a spherical particle to investigate the drag coefficient and Nusselt number at Reynolds numbers up to 1000. For laminar flow regimes ($1.0 \leq Re \leq 250$) typical of entrained-flow processes, different models for the drag coefficient c_d and Nusselt number Nu are described in the following sections.

2.4.1 Drag Coefficient and Nusselt Number for Spherical Solid Particles

The drag coefficient for smooth spherical particles can be taken from

$$c_d = a_1 + \frac{a_2}{\sqrt{Re}} + \frac{a_3}{Re} \tag{2.26}$$

where a_1, a_2, and a_3 are constants that apply over several ranges of relative particle Reynolds numbers.

Drawing on different references, the drag force coefficient for laminar flow regimes proposed by Clift et al. [40] was

$$c_d = \frac{24}{Re}\left(1 + 0.15Re^{0.687}\right) \tag{2.27}$$

Haider and Levenspiel [41] proposed a formula for a drag force coefficient given as

$$c_d = 0.3 + \frac{4.6}{\sqrt{Re}} + \frac{23.5}{Re} \tag{2.28}$$

Based on experimental work, Ranz and Marshall [42] provided a simple relation between the Nusselt number and the Reynolds and Prandtl numbers which took the form

$$Nu = 2 + 0.6\sqrt{Re}Pr^{\frac{1}{3}} \tag{2.29}$$

where Pr is the Prandtl number.

Another relationship was presented by Whitaker [43] based on experimental data from different references:

$$Nu = 2 + Pr^{0.4}\left(0.4\sqrt{Re} + 0.006Re^{\frac{2}{3}}\right) \tag{2.30}$$

2.4.2 Drag Coefficient and Nusselt Number for Porous Spherical Particles

Wittig et al. [6] generated spherical particles of different porosity using the packed-bed technique and performed a three-dimension CFD simulation of them to determine the influence of their porosity on drag coefficient and Nusselt number. As a result, the new formulas of the drag coefficient and Nusselt were worked out.

The drag coefficient is given as

$$c_d = 0.686\varepsilon_p + \frac{2.35}{\sqrt{Re}} + \frac{51.3 - 18.4\varepsilon_p}{Re} \tag{2.31}$$

The Nusselt number is expressed as

$$Nu = 7.14 - 20.1\varepsilon_p + 19\varepsilon_p^2 + (-9.16 + 32\varepsilon_p - 26.9\varepsilon_p^2)Re^{\frac{1}{2}}Pr^{\frac{1}{3}} + (4.71 - 15.3\varepsilon_p + 12.6\varepsilon_p^2)Re^{\frac{2}{3}}Pr^{\frac{1}{3}} \tag{2.32}$$

2.4.3 Drag Coefficient and Nusselt Number for Non-Spherical Particles

Focusing on interpreting the influences of particle shape on the drag coefficient and Nusselt number, Richter et al. [5] carried out a three-dimensional CFD simulation of several non-reacting particles with different shapes. As a result, correlations for the drag coefficient and Nusselt number for non-spherical particles were worked out as follows

The drag coefficient is given as

$$c_d = 0.21 + \frac{20}{Re}\left(\frac{l}{d_p}\right)^{0.58} + \frac{6.9}{\sqrt{Re}}\left(\frac{l}{d_p}\right)^{-1.4} \tag{2.33}$$

where l is the longitudinal particle length.

The Nusselt number is expressed as

$$Nu = 1.76 + 0.55\phi Pr^{\frac{1}{3}}\sqrt{Re}\phi_{\perp}^{0.075} + 0.014Pr^{\frac{1}{3}}Re^{\frac{2}{3}}\left(\frac{\phi}{\phi_{\perp}}\right)^{7.2} \tag{2.34}$$

where ϕ is the sphericity of the particle and $\phi_{\perp}$ is its crosswise sphericity, denoting the ratio between the projected area of the particle (in the flow direction) and the cross-section area of the volume-equivalent sphere.

2.5 Morphology Evolution of Char Particles

The morphology of a char particle influences both its trajectory and carbon consumption rate. Therefore, it plays a fundamental role in the char conversion. The morphology depends primarily on the initial pore structure of the char particle [44, 45], and its evolution during the char conversion process is not fully understood. After the pyrolysis process, coal particles turn into char particles consisting of carbon and inorganic material (ash). Depending on the process conditions such as total pressure and heating rate, the internal structure of the char particle has different characteristics and can be divided into three groups, as shown in Figure 2.5 [46].

(a) Group I (b) Group II (c) Group III

Fig. 2.5: The internal char structures [46]

The char particles of Groups I and II are characterized by a high internal void ($\varepsilon_{p,0} \geq 0.7$, swelling ratio $C_{sw} \geq 1.3$ for Group I and $\varepsilon_{p,0} = 0.4 - 0.7$, $C_{sw} \leq 1.0$ for Group II), and are modeled by a highly porous sphere with a thin, porous layer at the outer surface. In contrast, the char particles of Group III are characterized by a high density ($\varepsilon_{p,0} \leq 0.4$, $C_{sw} \leq 0.9$) and are considered to be a homogeneous porous medium with a spherical shape. The influence of parent coal petrography and pyrolysis pressure on the structure and intrinsic reactivity of its char was studied in [47, 48]. The structure corresponding to each char group is illustrated in Figure 2.6 [48, 49].

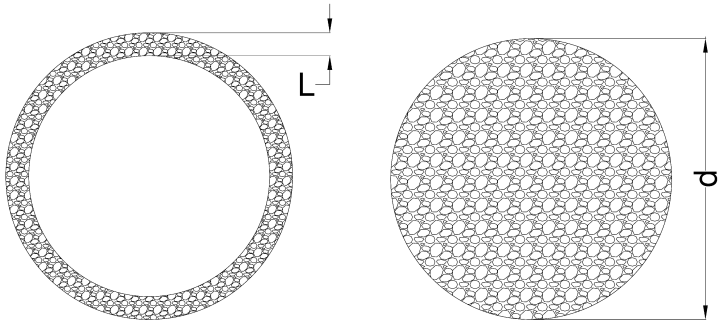

(a) Group I, II (b) Group III

Fig. 2.6: The geometry shapes modeling the internal char structures [48, 49]

The char particle sample formed after the coal pyrolysis is a mixture of three char groups. The fraction of Groups I, II and III char in the mixture depends on the vitrinite content of the parent coal and process conditions. Increasing the pressure, the fraction of Group I char increases, while char belonging to Group III decreases [47]. Due to very porous structure with large interior voids fraction and thin wall of pore, the char particle of Group I and II convert with constant size and decreasing density. They are also more likely to experience fragmentation when their carbon conversion reaches a critical level. In contrast, the fragmentation rarely occurs to the char of Group III. The diameter, density and internal structure of the char particle belonging Group III reduce simultaneously with the carbon conversion process [24, 49]. However, the morphology evolution of Group III char is not fully understood and needs further study. For that reason, the morphology evolution of the char particle of Group III is the objective of this dissertation. Two types of Australian bituminous coal (CRC-272 and CRC-274 [50, 51]) with the detailed analyses of the initial char morphology and char reactivity are used to input parameters of particle models in the next chapters.

One aspect of the particle morphology is the shape, which dominates the drag coefficient, hence the particle trajectory inside an entrained-flow gasifier. The investigations on a chemically reacting particle using particle-resolved models [11, 12, 20] show that at high Reynolds numbers there are temperature and reactant species gradients across the outer particle surface. Consequently, the carbon consumption rate distributes non-uniformly on the outer surface of the particle. This leads to the particle shape should be changed with the conversion process. However, the studies on the particle shape development during the conversion process are not complete. Hence, the particle shape development needs to be investigated further. This is one of the motivations of this Ph.D. thesis.

Other aspects of the particle morphology are the diameter, density, and specific surface area, which decide the rate-limiting process by governing the interplay of pore diffusion and chemical rate. The Random Pore Model, proposed by Bhatia and Perl-Mutter [52, 53], is widely applied for describing the evolution of the internal surface of a porous particle, such as a char particle, shown as the equation

$$S_V''' = S_{V,0}'''(1 - X_c)\sqrt{1 - \Psi \ln(1 - X_c)} \tag{2.35}$$

where $S'''_{V,0}$ is the initial specific surface area, X_c is the char conversion level and Ψ denotes the structure parameter. However, the Random Pore Model is only valid for Regime I. The particle diameter and density change in different ways, depending on the reaction regime. Now we consider an ash-free char particle with an initial carbon mass $m_{C,0}$, volume $V_{p,0}$, and carbon density $\rho_{C,0}$ consumed by heterogeneous reactions. During the conversion process, the instantaneous carbon mass, volume, and carbon density are m_C, V_p, and ρ_C, respectively. The ratio of the initial to the instantaneous mass of carbon is

$$\frac{m_C}{m_{C,0}} = \frac{V_p \rho_C}{V_{p,0} \rho_{C,0}} = \left(\frac{d_p}{d_{p,0}}\right)^3 \cdot \left(\frac{\rho_C}{\rho_{C,0}}\right) \tag{2.36}$$

where $d_{p,0}$ and d_p as the initial and instantaneous diameter of the particle (volume-equivalent to a spherical particle). With two positive variables α and β satisfying the condition, $3\beta + \alpha = 1$, Eq. (2.36) is rewritten as

$$\left(\frac{m_C}{m_{C,0}}\right)^{3\beta} \cdot \left(\frac{m_C}{m_{C,0}}\right)^{\alpha} = \left(\frac{d_p}{d_{p,0}}\right)^3 \cdot \left(\frac{\rho_C}{\rho_{C,0}}\right) \tag{2.37}$$

Substituting $m_C/m_{C,0}$ by $(1 - X_c)$ into Eq. (2.37), Eq. (2.37) is written as

$$\left(1 - X_c\right)^{3\beta} \cdot \left(1 - X_c\right)^{\alpha} = \left(\frac{d_p}{d_{p,0}}\right)^3 \cdot \left(\frac{\rho_C}{\rho_{C,0}}\right) \tag{2.38}$$

Accordingly, the well-known forms of single power law functions for the changes in particle diameter and density are derived and expressed as

$$\frac{d_p}{d_{p,0}} = \left(1 - X_c\right)^{\beta} \tag{2.39}$$

$$\frac{\rho_C}{\rho_{C,0}} = \left(1 - X_c\right)^{\alpha} \tag{2.40}$$

$$3\beta + \alpha = 1 \tag{2.41}$$

The diameter exponent β varying in the range of $0 \leq \beta \leq 1/3$ and the density exponent α in the range of $0 \leq \alpha \leq 1$ are considered as parameters of the char conversion model. When the char particle is not ash-free, the power law can be used to describe how the morphology of the reacting carbon core inside the particle evolves during the char conversion process. For Regime I, α is equal to 1 and β is zero, while for Regime III, α is zero and β is equal to 1/3. Most of the authors recommend that for the regime II, α and β need to vary as a function of the effectiveness factor η during char conversion. There are many works devoted to clarifying the functional relationships of the conversion parameters α and β with process conditions and particle properties. The following provides a brief review of those works.

Essenhigh was the first among authors working on theoretical correlation of the change in diameter and density with mass loss. He examined the correlation between the relative density and diameter of a particle.

$$\frac{\rho_C}{\rho_{C,0}} = \left(\frac{d_p}{d_{p,0}}\right)^{\alpha'} \tag{2.42}$$

The exponent α' is defined as the ratio of the internal to outer reaction rate, and governed by the initial particle density $\rho_{c,0}$. The expressions of the exponent α' corresponding to different reaction regimes are given in [54]. Essenhigh also defined a second effectiveness factor η', which indicates particle burning behavior, as in the following equation [55]

$$\eta' = 1 + \frac{r_{int}}{r_{ext}} = 1 + \frac{\alpha}{3\beta} \tag{2.43}$$

where r_{int} and r_{ext} stand for the internal and outer reaction rate, respectively. Based on the works of Essenhigh, Ma described the ratio of α to β as a function of the effectiveness factor η and reaction surfaces, using the following formula [56].

$$\frac{\alpha}{\beta} = 3\eta \frac{A_{int}}{A_p} \tag{2.44}$$

where A_{int} and A_p are the internal and outer surface of the char particle.

Ma [56] also developed a detailed particle burning model, where the effectiveness factor and model parameters depend on the particle's structure. In his work, the changes in the diameter and density were suggested as

$$\frac{\rho_C(\rho_{C,t} - \rho_{C,0})}{\rho_{C,0}(\rho_{C,t} - \rho_C)} = \left(\frac{d_p}{d_{p,0}}\right)^{\xi} \tag{2.45}$$

$$\frac{m_C}{m_{C,0}} = \frac{\rho_C}{\rho_{C,0}} \left[\frac{\rho_C(\rho_{C,t} - \rho_{C,0})}{\rho_{C,0}(\rho_{C,t} - \rho_C)}\right]^{3/\xi} \tag{2.46}$$

where $\rho_{C,t}$ is the true density of carbon, while m_C and $m_{C,0}$ are the instantaneous and initial mass of carbon in the carbon particle. The burning mode parameter ξ can be calculated from the particle's properties and the Thiele modulus using the formula

$$\xi = \frac{3 d_p \rho_C S_m'''}{2\Phi\varepsilon_p} \tag{2.47}$$

Based on the work of Essenhigh [54], Liu and Niksa [34] calculated the density exponent α as a function of a particle's properties,

$$\alpha = \frac{\chi}{3 + \chi} \tag{2.48}$$

with the density parameter χ

$$\chi = \frac{d_p \eta S_V'''}{2} \tag{2.49}$$

Halama [57] proposed that the exponent β was linearly dependent on the effectiveness factor η for numerical models integrated in CFD codes.

$$\beta = \frac{1 - \eta}{3} \tag{2.50}$$

However, most of the works discussed above are based on 0D models to describe the mass loss of a porous carbon particle. The particle's properties, e.g. the density, are homogeneous at every carbon conversion level. Therefore, the reduction in particle volume is related directly to the amount of carbon consumed on the outer particle surface and the instantaneous density. However, in Regime II the carbon conversion distributes non-uniformly inside the porous particle. This lead to the particle's properties being in-homogeneous. The decrease in particle volume is mainly related to the density gradient. Therefore, correlations between conversion parameters, such as the diameter and density exponent, and parameters characterizing the reaction regime, for example the effectiveness factor, are not fully understood and requires further investigations. This is the next aim of this Ph.D. thesis.

3 Modeling of Dilute Particulate Flow

There are two main approaches for numerical simulations of multiphase flows, based on either the Euler-Lagrange approach or the Euler-Euler approach. The difference between the two approaches lies in the different techniques describing the movement of the particles. For entrained-flow processes, the diluted particulate flow is typically treated based on the Lagrangian model, while the fluid phase is treated as a continuum by solving the Navier–Stokes equations. As the volume fraction occupied by the solid phase in entrained-flow reactors is less than 10 %, the particle-particle interactions and the effects of the particle volume fraction on the fluid phase are negligible. The following section offers a basic theory of the framework of the Euler-Lagrange model.

3.1 Governing Equation System for Fluid Phase

3.1.1 Conservation of Mass

The mass conservation equation, also known as the continuity equation, is based on the mass balance for an element volume of fluid flow. For compressible flows, the continuity equation can be written as follows:

$$\frac{\partial \rho_g}{\partial t} + \nabla \cdot (\rho_g \, \vec{u}) = M_S \tag{3.1}$$

where M_S is a mass source, which represents the mass exchange between the particulate flow and fluid flow.

3.1.2 Conservation of Momentum

The momentum conservation equation, also known as the Navier-Stokes equation, is based on Newton's second law. It expresses the change in momentum due to forces acting on an element volume of fluid flow, and can be written as follows:

$$\frac{\partial (\rho_g \vec{u})}{\partial t} + \nabla \cdot (\rho_g \vec{u} \vec{u}) = -\nabla p + \nabla \cdot \boldsymbol{\tau} + \vec{F}_S \tag{3.2}$$

where p is the pressure and $\vec{F}_S$ is a momentum source which represents the momentum exchange between the particulate flow and fluid flow. The stress tensor comprises the dynamic viscosity μ and is calculated as

$$\boldsymbol{\tau} = \mu \left(\left(\nabla \vec{u} + (\nabla \vec{u})^{\mathsf{T}} \right) - \frac{2}{3} \nabla \cdot \vec{u} \mathbf{I} \right) \tag{3.3}$$

3.1.3 Conservation of Energy

The energy conservation equation is a result of the first law of thermodynamics. That means that the rate of change in the energy of an element volume of fluid flow equals the rate

of additional heat plus the rate of work done by the element volume. Hence, the energy conservation equation takes the form

$$\rho_g \frac{\partial h}{\partial t} + \nabla \cdot (\vec{u}(\rho_g h + p)) = \nabla \cdot (\lambda_g \nabla T - \vec{q}_{rad} - \sum_i h_i \vec{J}_i + \tau \cdot \vec{u}) + \sum_{j=1}^{N_{hom}} \frac{\Delta H_j^0}{M_w} R_{hom,j} + H_S \tag{3.4}$$

In the energy conservation equation, λ denotes the thermal conductivity, h stands for the total enthalpy, h_i is the sensible enthalpy of species i, J_i is the diffusion flux of species i, ΔH_j^0 is the heat of homogeneous reaction j, $\vec{q}_{rad}$ is the gas-phase radiation source, M_w is the molecular weight, $R_{hom,j}$ is the rate of the homogeneous chemical reaction j, N_{hom} is the number of homogeneous reactions and H_S is the heat exchange between the particles and fluid flow.

3.1.4 Transport of Species

The species transport equation is derived from the principle of the conservation of mass, applied to each chemical species in a fluid flow. The following equation expresses the species conservation equation

$$\rho_g \frac{\partial Y_i}{\partial t} + \nabla \cdot (\rho_g \vec{u} Y_i) = \nabla \cdot (\rho_g D_{i,m} \nabla Y_i + + D_{T,i} \frac{\nabla T}{T}) + \sum_{j=1}^{N_{hom}} R_{hom,i,j} + M_{S,i} \tag{3.5}$$

where Y_i is the mass fraction and $D_{i,m}$ is the mass diffusion coefficient of species i in the fluid phase, $D_{T,i}$ is the thermal diffusion coefficient of species i, $R_{hom,i,j}$ denotes the consumption/formation rate of species i in the reaction j and $M_{S,i}$ stands for the source (sink) of species i due to heterogeneous reactions.

3.1.5 Radiative Heat Transfer

At high temperatures and pressures with robust radiative species such as water vapour and carbon dioxide, the transfer of incident radiation should be included in the energy conservation equation to accurately describe the gas temperature, enhancing the reliability of the reactor's CFD simulation result. For coal combustion and gasification applications, the P-1 Radiation Model is robust, works reasonably well, and can easily be applied to complicated geometries with curvilinear coordinates. The following section will present the theory behind the P-1 radiation model when the particulate effects are taken into account for radiative heat transfer. The transport equation for incident radiation is given as

$$\nabla \cdot (\Gamma \nabla G) + 4\pi \left(a\, n_{ind}^2 \frac{\sigma T^4}{\pi} + E_p \right) - (a + a_p) G = G_S \tag{3.6}$$

where G is the incident radiation, a is the absorption coefficient, n_{ind} denotes the refractive index of the medium, σ is the Stefan-Boltzmann constant, E_p and a_p are the equivalent emission and the equivalent absorption coefficient of particle, respectively, and G_S stands for a user-defined radiation source. The equivalent emission and equivalent absorption coefficient of the particles are defined as

$$E_p = \lim_{V \to 0} \sum_{n=1}^{N_p} \epsilon_{pn} A_{pn} \frac{\sigma T_{pn}^4}{\pi V_{cv}} \tag{3.7}$$

$$a_p = \lim_{V \to 0} \sum_{n=1}^{N_p} \epsilon_{pn} \frac{A_{pn}}{V_{cv}} \tag{3.8}$$

where ϵ_{pn} and T_{pn} are the emissivity and temperature of the n^{th} particle, respectively, $A_{pn} = \pi d_{pn}^2/4$ is the projected area of particle, and N_p is the number of particles in the control volume V_{cv}. The quantity Γ in Eq. (3.6) is defined as

$$\Gamma = \frac{1}{3(a + a_p + \sigma_p)} \tag{3.9}$$

The equivalent particle scattering factor is defined as

$$\sigma_p = \lim_{V \to 0} \sum_{n=1}^{N_p} (1 - f_{pn})(1 - \epsilon_{pn}) \frac{A_{pn}}{V_{cv}} \tag{3.10}$$

where f_{pn} is the scattering factor associated with the n^{th} particle. The radiative heat flux q_{rad} is calculated as

$$q_{rad} = -\Gamma \nabla G \tag{3.11}$$

The radiative flux is given as

$$-\nabla \cdot q_{rad} = -4\pi \left(a\, n_{ind}^2 \frac{\sigma T^4}{\pi} + E_p \right) + (a + a_p) G + G_S \tag{3.12}$$

The radiative heat flux is embodied in the energy conservation equation to account for heat sources (or sinks) due to radiative heat transfer.

3.2 Turbulence Treatment and Turbulence-Chemistry Interaction

3.2.1 Turbulence Treatment

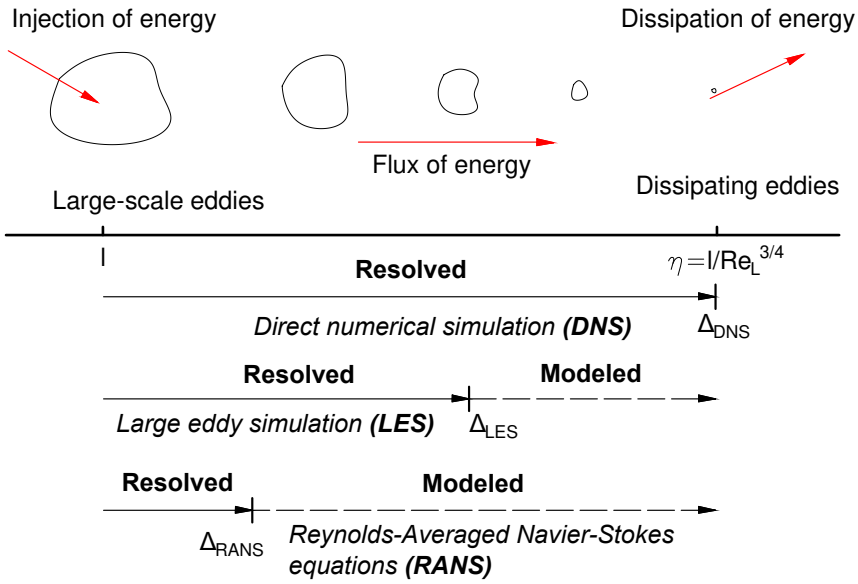

Fig. 3.1: General turbulence model applied for the range of eddy length scales [58]

In contrast to laminar flow, where fluid flow moves smoothly and parallel to each other, turbulence flow is characterized by the fluctuating and chaotic movement of the fluid particles in every direction at a small scale and high frequency [59]. These fluctuations significantly enhance

the mixing of transported quantities such as momentum, energy and species concentration, leading to fluctuating transported quantities. As a result, dramatic changes in the flow field patterns and acceleration in the rate of chemical reactions are observed. These fluctuations generate eddies with a wide range of lengths and time scales, ranging from those compatible with the level of mean flow to the smallest level corresponding to the Kolmogorov scale [60]. There are three approaches typically used to describe the turbulent flow, as shown in Figure 3.1 with the short following description [58].

Direct numerical simulation (DNS) Exact Navier-Stokes equations are solved directly at every scale. This approach requires a fine grid and tiny time steps to resolve the Kolmogorov length scale and the period of the fastest fluctuations. Hence, direct numerical simulation is very computationally intensive, but it provides the most accurate prediction of turbulence flow behavior.

Large eddy simulation (LES) Navier-Stokes equations are filtered by mathematical manipulation to compute larger eddies' turbulence effects, which are an isotropic and heavily affected by boundary conditions. On the other hand, the impact of small eddies, which tend to be more isotropic and universal, are computed using a subgrid-scale model. Therefore, LES is not as computationally intensive as DNS, and this approach is becoming increasingly feasible for practical engineering problems.

Reynolds-Averaged Navier-Stokes (RANS) As Navier-Stokes equations are time-averaged, additional unknown variables covering the turbulence effects that emerge in time-averaged flow equations need to be modeled in terms of known quantities. That means that all of the eddy scales are modeled. Therefore, the RANS approach dramatically reduces the required computational effort and resources, and it is widely applied for practical engineering applications.

As turbulence accelerates the momentum, heat and mass transport in the body of a fluid flow, it significantly enhances the overall chemical reaction rate. The turbulence-chemistry interaction is described using the following models.

3.2.2 Turbulence-Chemistry Interaction

Among the models describing the interaction between turbulence and the chemical reaction process, the Eddy Dissipation Concept (EDC) is a typical model including detailed chemical mechanisms in turbulent flows [61]. The model considers small, turbulent scales (at Kolmogorov scale) as fine homogeneous reactors (concept reactors) where chemical reactions take place. The reactors exchange mass and energy with the surrounding fluid. The length and time scale of the concept reactor are provided by Gran et al. [62]

$$\xi^* = C_\xi \left(\frac{\nu_k \epsilon}{k^2}\right)^{1/4} \tag{3.13}$$

$$\tau^* = C_\tau \left(\frac{\nu_k}{\epsilon}\right)^{0.5} \tag{3.14}$$

where ξ^* and τ^* are the length scale and time scale of the concept reactor, respectively; C_ξ=2.1377 and C_{τ^*}=0.4082 are the volume fraction constant and time scale constant, respectively. The k and ϵ are the kinetic energy and the kinetic dissipation rate of turbulent flow, respectively. The consumption/formation rate of species i is calculated based on integrating the Arrhenius rates over the length and time scale as

$$R_{hom,i} = \frac{\rho_g (\xi^*)^2}{\tau^* [1 - (\xi^*)^3]} (Y_i^* - Y_i) \tag{3.15}$$

where Y_i^* is the mass fraction species i in the concept reactor after reacting over the time τ^*.

3.3 Particle Motion

The particle's trajectory significantly influences its residence time, one of the important parameters controlling the degree of particle conversion, and hence affects the efficiency and performance of an entrained-flow gasifier. The Euler-Lagrange approach is commonly used to predict the particle trajectory, based on the balance of forces acting on the particle.

3.3.1 Particle Force Balance

According to Newton's second law, the change in particle momentum equals the total forces acting on the particle.

$$\frac{d\vec{u}_p}{dt} = \sum_i \vec{F}_i \tag{3.16}$$

where $\vec{u}_p$ and $\vec{F}$ are the absolute particle velocity and acting force per unit particle mass, respectively.

Gravity force

The gravity force $\vec{F}_{grav}$ is calculated using the following formula:

$$\vec{F}_{grav} = \vec{g} V_p (\rho_p - \rho_g) \tag{3.17}$$

where $|\vec{g}|$=9.81 m/s^2 is the gravitational acceleration and V_p is particle volume.

Drag force

The drag force $\vec{F}_d$ always acts opposite to the direction of the particle's velocity, and is the most dominant force influencing the trajectory of the particle inside entrained-flow gasifiers. The magnitude of the drag force acting on a spherical particle is calculated by Eq. (2.22).

Thermophoretic force

The thermophoretic force mainly influences small particles ($d_p < 10\,\mu$m) [27]. The force is generated when the particle experiences a change in the temperature of the surrounding fluid. The thermophoretic force acts on the particle in the direction opposite to the temperature change and is calculated as

$$\vec{F}_{th} = -D_{th} \frac{1}{m_p T} \nabla T \tag{3.18}$$

where D_t as the thermophoretic coefficient is suggested by Talbot [63].

$$D_t = \frac{6\pi d_p \mu^2 C_s (K + C_t K_n)}{\rho_g (1 + 3C_m K_n)(1 + 2K + 2C_t K_n)} \tag{3.19}$$

where $Kn = 2\delta/d_p$ denotes the Knudsen number with δ as the mean fee path of the fluid; $K = \lambda_g/\lambda_p$ with λ_p as the particle thermal conductivity; and C_s=1.17, C_t=2.18 and C_m=1.14 are constant values. This expression assumes that the particle is a sphere and the fluid is an ideal gas.

Other forces

Brownian motion and Saffman's lift have a strong influence on sub micron particles. Hence, for the typical coal size distribution fed into a pressured gasifier, the two forces can be neglected [64].

3.3.2 Particle Trajectory

The particle trajectory inside an entrained-flow gasifier is yielded by solving a set of coupled ordinary differential equations, Eq. (3.20) and Eq. (3.21), over the particle time steps [27].

$$\frac{du_p}{dt} = \frac{1}{\tau_p}(u - u_p) + a_{tf} \tag{3.20}$$

$$\frac{dx_p}{dt} = u_p \tag{3.21}$$

The term τ_p, which is used to calculate the acceleration due to the drag force acting on the particle, takes a different formula depending on the flow regime. For example, in Stokes regime τ_p is calculated as

$$\tau_p = \frac{\rho_p d_p^2}{18\mu}\frac{24}{c_d Re} \tag{3.22}$$

The term a_{tf} accounts for accelerations due to all other forces except the drag force. Two approaches can be used to solve the set of equations; either analytical integration or numerical integration, such as the Euler implicit, trapezoidal, and Runge-Kutta schemes. For example, here, the Euler implicit scheme is applied to predict the particle trajectory. When Euler implicit discretization is applied, the new particle velocity and particle position, denoted as $(n+1)$, are calculated based on the current situation, denoted as n, using the following equations:

$$u_p^{n+1} = \frac{u_p^n + \Delta t(a_{tf} + \frac{u^n}{\tau_p})}{1 + \frac{\Delta t}{\tau_p}} \tag{3.23}$$

$$x_p^{n+1} = x_p^n + \frac{1}{2}\Delta t\left(u_p^n + u_p^{n+1}\right) \tag{3.24}$$

3.3.3 Stochastic Tracking for Particles in Turbulent Flow

The instantaneous velocity of the turbulent flow $u(t)$ can be broken down into the mean velocity u and its fluctuating component $u^{'}$. By default, the CFD computes particle trajectories using the mean velocity u as in Eq. (3.23). To take the effect of fluctuating velocity component $u^{'}$ into account for the particle trajectories, a stochastic tracking sub model, the DRW model, is used. The interaction between a particle and an eddy containing it is characterized by two parameters: a Gaussian distributed random velocity fluctuation $u^{'}$, $v^{'}$ and $w^{'}$ and a time interaction, τ_{inter}=min(τ_e t_{cross}) [27]. The values of the random velocity fluctuations during the lifetime of the turbulent eddy obey a Gaussian probability distribution.

$$u^{'} = \zeta\sqrt{\overline{u^{'2}}} = \zeta\sqrt{\frac{2}{3}k} \tag{3.25}$$

This is similar to the remaining random velocity fluctuations: $v^{'} = w^{'} = \zeta\sqrt{\frac{2}{3}k}$. The eddy's lifetime, τ_e, is defined as a random variation about T_L, the integral time scale describing the time spent in turbulent motion along the particle path.

$$\tau_e = -T_L ln(\varsigma) \tag{3.26}$$

where ς is a random number between 0 and 1; $T_L = C_L(k/\epsilon)$ with C_L is an input parameter, C_L=0.3 for the $k-\epsilon$ turbulent model and its variants. The particle eddy crossing time, t_{cross}, is defined as

$$t_{cross} = -\tau_{relax} ln\left[1 - \left(\frac{L_e}{\tau_{relax}|u - u_p|}\right)\right] \tag{3.27}$$

where τ_{relax} is the particle relaxation time and L_e denotes the eddy length scale. The particle is assumed to interact with the eddy during the time of the interaction τ_{inter}. When this time is reached, a new value of ζ in Eq. (3.25) is used to calculate a new value of the instantaneous velocity, u', v' and w'.

3.4 Momentum, Heat and Mass Exchange Between a Particle and Fluid Phase

Interactions between particles and gas phase in an entrained-flow process are exchanges of mass, momentum, and energy, as depicted qualitatively in Figure 3.2. When particles leave a control volume, these exchanges are considered source terms in the related conservation equations. The particulate and fluid flow are solved iteratively until both reach convergence states.

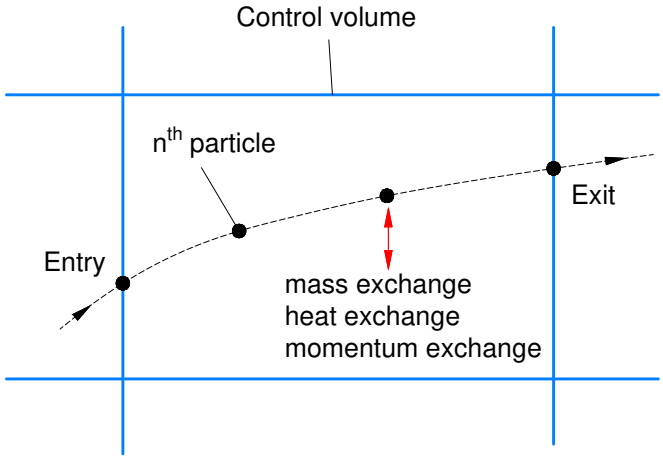

Fig. 3.2: Illustration of mass, heat and momentum exchange between continuous phase and particle [4, 27]

The mass exchange is embodied in the continuity equation Eq. (3.1), the mass source being M_S, which is calculated as the following equation [4]

$$M_S = -\frac{1}{V_{cv}} \sum_{n=1}^{N_p} \frac{1}{\Delta t^*} (m_{p,n,out} - m_{p,n,in}) \tag{3.28}$$

where $m_{p,n,in}$ and $m_{p,n,out}$ denote the n^{th} particle mass on the control volume entry and exit respectively, Δt^* is the time required for the particle to traverse the control volume and V_{cv} is the volume of the control cell.

The exchange of momentum is put in the momentum conservation equation Eq. (3.2) as the momentum source $\vec{F_S}$, which is determined using the following equation [27]

$$|\vec{F_S}| = \frac{1}{V_{cv}} \sum_{n=1}^{N_p} \left[\frac{c_d \pi d_p^2 (u - u_p)^2}{8} + F_{other} \right] \dot{m}_p \tag{3.29}$$

where F_{other} is other interaction forces and $\dot{m}_p$ is the mass flow rate of the particles through the control volume.

The exchange of energy is considered to be an energy source in the energy equation Eq. (3.4), which is regarded as changes in the thermal energy of each particle passing through a control

volume [4].

$$H_S = \frac{1}{V_{cv}} \left\{ \sum_{n=1}^{N_p} \frac{1}{\Delta t^*} \left[(m_{p,n,in} - m_{p,n,out})(-h_{fg} + h_{devol}) + \sum_{j=1}^{N_{het}} (1 - f_{h,j}) \Delta m_{p,n,j} \Delta H_{R_{het,j}} \right] + \sum_{n=1}^{N_p} \frac{1}{\Delta t^*} \left[m_{p,n,in} \int_{T_{ref}}^{T_{p,in}} c_{p,p} dT - m_{p,n,out} \int_{T_{ref}}^{T_{p,out}} c_{p,p} dT \right] \right\} \tag{3.30}$$

where T_{ref} is the reference temperature for enthalpy; h_{fg} and h_{devol} are the latent and devolatilization heat; a fraction, $f_{h,j}$, of heat produced by the heterogeneous reaction j is absorbed directly by the particle; $T_{p,in}$ and $T_{p,out}$ are the temperature of the particle on the control volume entry and exit, respectively.

4 Particle Shape Development and Dynamic Drag Model

The shape of a particle affects its trajectory and residence time in an entrained-flow gasification significantly. The impact of the particle shape on the drag has been studied intensively using CFD simulation in recent decades [5, 6, 65–69]. These studies have primarily focused on non-reactive, non-spherical particles moving at a constant Reynolds number in a quiescent flow field, while the development of the particle shape due to heterogeneous chemical reactions has been neglected. For that reason, this chapter focuses on the shape development of several spherical and non-spherical particles at the flame zone conditions of an entrained-flow gasifier, where the temperature and species concentration gradient across the particle is the highest. Based on the shape development, dynamic models of the drag coefficient for the particles studied are introduced.

4.1 Numerical Strategy

Several particles with initially different shapes are considered, as shown in Figure 4.1.

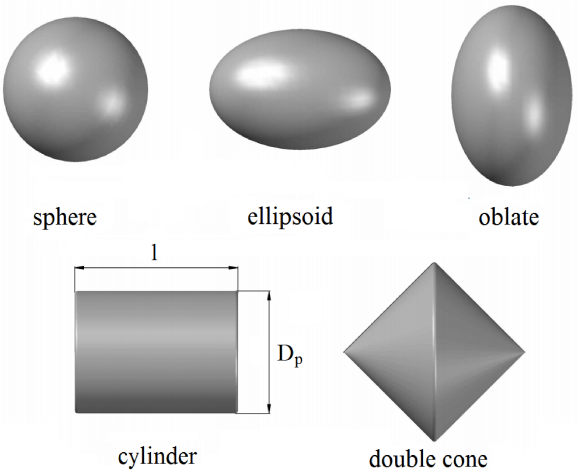

Fig. 4.1: Initial particle shapes considered [20]

Tab. 4.1: Sphericity, length-to-diameter ratio, and geometry ratio for the shapes of the non-spherical particles shown in Figure 4.1

Characteristics	sphere	ellipsoid	oblate	cylinder	double cone
ϕ	1	0.973	0.970	0.866	0.952
$\frac{l}{d_p}$	1	0.900	1.168	0.820	1.162
$\frac{l}{D_p}$	1	$\frac{3}{2}$	$\frac{2}{3}$	$\frac{4}{3}$	1

The particles' initial characteristics are shown in Table 4.1, where l is the characteristic particle length, d_p is the diameter of the volume-equivalent sphere and D_p is the characteristic

particle diameter. The flow inside entrained-flow gasifiers under typical operation conditions is fully turbulent. However, at the particle scale the particles experience a laminar flow during most of their residence time [70]. Thus, particle shape development in the laminar flow regime is examined in this study. Due to the particles embodied in the laminar flow regime, the flow surrounding isolated particles is axis-symmetric. Therefore, the computational domain with boundary conditions is defined in Figure 4.2. To avoid blockage effects, the computational domain was constituted by extending $40\,d_p$ in the radial direction, $30\,d_p$ in the upstream direction and $100\,d_p$ in the downstream direction [11].

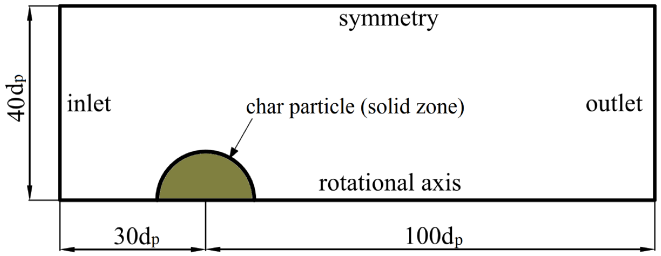

Fig. 4.2: Computational domain and boundary conditions investigation of particle shape development [20]

The flame zone of an entrained-flow gasifier is characterized by the highest temperature and species concentration gradients across the particle, which have the greatest effect on the particle shape. For that reason, this work focuses on char conversion in oxygen-rich conditions. The gas conditions and main gas components extracted from a CFD model of a Siemens-type gasifier [2] are used to set the inlet conditions for modeling single reacting particles in this work, as shown in Table 4.2. For simplicity, the gas conditions and components are assumed to be homogeneously distributed over the inflow boundary and constant in time. This allows analyzing how the reaction conditions affect the change in particle shape. The gas flow consists of six reactant species, O_2, CO, CO_2, H_2, H_2O, and N_2, and enters the domain with an inlet velocity magnitude corresponding to the particle Reynolds number under consideration. It is assumed that the orientation of the particle in the flow field is fixed. The particle Reynolds number is defined as

$$Re = \frac{\rho_{g,in} |\vec{u}|_{in} d_p}{\mu_{in}} \tag{4.1}$$

where, $\rho_{g,in}$ is the gas density, $\vec{u}_{in}$ denotes the gas velocity vector, d_p is the particle diameter, and μ_{in} stands for the dynamic viscosity of the gas phase at the inlet.

Tab. 4.2: Inlet and operation conditions for the study of particle shape development: gas conditions extracted from a CFD model of an entrained-flow gasifier [2]

T_{in}	p_{op}	Re	$Y_{CO_2,in}$	$Y_{O_2,in}$	$Y_{H_2O,in}$	$Y_{CO,in}$	$Y_{H_2,in}$
1480 K	30 bar	1-200	0.223	0.187	0.221	0.0	0.0

A semi-global mechanism and a detailed mechanism (DRM22, 22 reactive species, 104 reactions) were studied and compared to each other. The comparison showed that the species distribution around single particles exhibits very good agreement for these applied mechanisms [12]. Therefore, the semi-global mechanism applied for the homogeneous reactions in this work for

the purpose of simplification is expressed as the follows [12, 71].

$$\mathrm{CO} + \frac{1}{2}\mathrm{O_2} + \mathrm{H_2O} \longrightarrow \mathrm{CO_2} + \mathrm{H_2O} \tag{R1}$$

$$\mathrm{CO} + \mathrm{H_2O} \longrightarrow \mathrm{CO_2} + \mathrm{H_2} \tag{R2}$$

$$\mathrm{CO_2} + \mathrm{H_2} \longrightarrow \mathrm{CO} + \mathrm{H_2O} \tag{R3}$$

A simple power law was used to compute the reaction rate for R1, R2, and R3. The parameters of these homogeneous reactions are given in Table 4.3.

Tab. 4.3: Reaction rates for homogeneous and heterogeneous reactions

Reac.	$k_{j\infty}$	$E_{a,j} \,/\, \mathrm{J/kmol}$	n_j	Reference
R1	$2.24 \times 10^{12}\,\mathrm{m}^{2.25}/(\mathrm{kmol}^{0.75}\,\mathrm{s})$	1.6736×10^{8}	-	[12]
R2	$2.75 \times 10^{9}\,\mathrm{m}^{3}/(\mathrm{kmol\,s})$	8.368×10^{7}	-	[12]
R3	$9.98 \times 10^{10}\,\mathrm{m}^{3}/(\mathrm{kmol\,s})$	1.205×10^{8}	-	[12]
R4	$0.3979\,\mathrm{kg}/(\mathrm{m}^2\,\mathrm{s\,Pa}^{\mathrm{n}})$	2.11×10^{8}	0.4	[72]
R5	$29.842\,\mathrm{kg}/(\mathrm{m}^2\,\mathrm{s\,Pa}^{\mathrm{n}})$	2.31×10^{8}	0.4	[72]
R6	$0.0297\,\mathrm{kg}/(\mathrm{m}^2\,\mathrm{s\,Pa}^{\mathrm{n}})$	1.36×10^{8}	0.8	[72]

Because the development the outer particle shape is considered as an isolated effect, the particle was defined as a solid zone accompanying the wall surface reaction model accounting for the carbon consumption due to heterogeneous chemical reactions. Thus, heterogeneous reactions cause a reduction in particle size and change in the particle shape but have no effect on the particle's pore structure. The particle density and specific surface area are constant during the char conversion process. Three heterogeneous chemical reactions describe the char conversion. Their chemical mechanism is written as

$$\mathrm{C} + \mathrm{CO_2} \longrightarrow 2\,\mathrm{CO} \tag{R4}$$

$$\mathrm{C} + \mathrm{H_2O} \longrightarrow \mathrm{CO} + \mathrm{H_2} \tag{R5}$$

$$\mathrm{C} + 0.5\,\mathrm{O_2} \longrightarrow \mathrm{CO} \tag{R6}$$

The work in this chapter focuses on an Australian coal (type CRC272) widely studied at CSIRO in recent years. The corresponding intrinsic kinetics for the heterogeneous reactions introduced by Hla et al. [72] are converted into $\mathrm{kg}/(\mathrm{m}^2\,\mathrm{s\,Pa}^{\mathrm{n}})$ and given in Table 4.3. The carbon consumption rate on the outer particle surface results from the interplay between the intrinsic kinetic and the pore diffusion, and it is approximated using the efficiency factor approach. Hence, the heterogeneous reaction rates referred to the outer particle surface are calculated by the following equations [15].

$$R_{het,4} = \eta_4 \frac{V_p S'''_{m,0}\,\rho_{p,0}}{A_p} \frac{|\nu_{\mathrm{CO_2},4}|M_{w,\mathrm{CO_2}}}{|\nu_{C,4}|M_{w,C}} k_{4\infty} \exp\left\{-\frac{E_{a,4}}{R_G\,T_{p,s}}\right\} p_{CO_2,s}^{n_4} \tag{4.2}$$

$$R_{het,5} = \eta_5 \frac{V_p S'''_{m,0}\,\rho_{p,0}}{A_p} \frac{|\nu_{\mathrm{H_2O},5}|M_{w,\mathrm{H_2O}}}{|\nu_{C,5}|M_{w,C}} k_{5\infty} \exp\left\{-\frac{E_{a,5}}{R_G\,T_{p,s}}\right\} p_{H_2O,s}^{n_5} \tag{4.3}$$

$$R_{het,6} = \eta_6 \frac{V_p S'''_{m,0}\,\rho_{p,0}}{A_p} \frac{|\nu_{\mathrm{O_2},6}|M_{w,\mathrm{O_2}}}{|\nu_{C,6}|M_{w,C}} k_{6\infty} \exp\left\{-\frac{E_{a,6}}{R_G\,T_{p,s}}\right\} p_{O_2,s}^{n_6} \tag{4.4}$$

Here, $T_{p,s}$ is the outer surface temperature, and $p_{i,s}$ denotes the partial pressure of species i (i=$\mathrm{CO_2}$, $\mathrm{H_2O}$ and $\mathrm{O_2}$) on the outer particle surface. The effectiveness factor for species i and reaction j is estimated as

$$\eta_j = \frac{1}{\Phi_j}\left(\frac{1}{\tanh(\,3\Phi_j)} - \frac{1}{3\Phi_j}\right) \tag{4.5}$$

The Thiele modulus Φ_j is defined as

$$\Phi_j = \frac{V_p}{A_p}\sqrt{\frac{n_j+1}{2}\frac{|\nu_{i,j}|\ S'''_{m,0}\,\rho_{p,0}\,R_G\,T_{p,s}k_{j\infty}\exp\left\{-\frac{E_{aj}}{R_G\,T_{p,s}}\right\}p_{i,s}^{n_j-1}}{M_{w,C}\,D_{i,m}\,\varepsilon_{p,0}^2}} \tag{4.6}$$

where, V_p is the particle volume, A_p is the outer particle surface, $S'''_{m,0}$ denotes the specific mass surface area of the char particle, $\rho_{p,0}$ is the apparent density of the particle, ν_{ij} is the stoichiometric coefficient, $D_{i,m}$ is the laminar diffusion coefficient of species i in the mixture, and $\varepsilon_{p,0}$ is the particle porosity. These parameters were taken from measurements of a bituminous char sample, given in Table 4.4.

Tab. 4.4: Char properties used to investigate particle shape development [15]

Apparent density	$\rho_{p,0}$	$766.4\,\mathrm{kg/m^3}$
Specific mass surface area	$S'''_{m,0}$	$354.9\,\mathrm{m^2/g}$
Particle porosity	$\varepsilon_{p,0}$	0.5
Particle diameter	$d_{p,0}$	$8-263\,\mu\mathrm{m}$

The heterogeneous reaction kinetics were applied in the CFD solver employing user-defined functions. For the gas flow, the RANS equations coupled with the energy conservation equation and species transport equations were solved in the transient simulation to obtain the flow field, temperature field and species distribution in the gas flow:

$$\frac{\partial\rho_g}{\partial t} + \nabla\cdot(\rho_g\,\vec{u}) = 0 \tag{4.7}$$

$$\frac{\partial(\rho_g\vec{u})}{\partial t} + \nabla\cdot(\rho_g\vec{u}\vec{u}) = -\nabla p + \nabla\cdot\boldsymbol{\tau} \tag{4.8}$$

$$\rho_g\frac{\partial Y_i}{\partial t} + \nabla\cdot(\rho_g\vec{u}Y_i) = \nabla\cdot(\rho_g D_{i,m}\nabla Y_i + D_{T,i}\frac{\nabla T}{T}) + \sum_{j=1}^{N_{hom}} R_{hom,i,j} \tag{4.9}$$

$$\rho_g\frac{\partial h}{\partial t} + \nabla\cdot(\vec{u}(\rho_g h + p)) = \nabla\cdot(\lambda_g\nabla T - \vec{q}_{rad} - \sum_i h_i\vec{J}_i + \tau\cdot\vec{u}) + \sum_{j=1}^{N_{hom}}\frac{\Delta H_j^0}{M_w}R_{hom,j} \tag{4.10}$$

The gas density follows the ideal-gas law. The heat capacity of each species is based on a fourth-order polynomial expression [73], and the heat capacity of the mixture is based on the mass-weighted average of the individual heat capacities. The thermal conductivity for the single species were calculated using kinetic theory, and the mole-weighted average was used for the mixture. Details are given in [74]. Gas-to-gas and particle-to-gas radiation was taken into account by applying a P-1 radiation model [75]. Boundary conditions have to be stated at the inlet and outlet boundary as well as at the axis of symmetry and the upper side of the computational domain. Neumann boundary conditions are applied for the axis of symmetry and the upper side:

$$\frac{\partial p}{\partial r} = 0, \quad \frac{\partial\vec{u}}{\partial r} = 0, \quad \frac{\partial Y_i}{\partial r} = 0, \quad \frac{\partial T}{\partial r} = 0 \tag{4.11}$$

At the inlet boundary, the values of the gas velocity, mass fractions and temperature are given as

$$\vec{u} = \vec{u}_{in}, \quad Y_i = Y_{i,in}, \quad T = T_{in} \tag{4.12}$$

At the particle surface, the convective and diffusive mass fluxes are balanced by the heterogeneous reaction rates. The surface temperature of the particle depends on the balance

between the heat release due to the heterogeneous reactions, the convective heat exchange with the surrounding gas, the heat conduction inside the particle and in the gas phase, and the radiative heat exchange:

$$\rho_{g,s}\, D_{i,m} \frac{\partial Y_{i,s}}{\partial \vec{n}} - \dot{m}_C'' Y_{i,s} = R_{het,j} \tag{4.13}$$

$$\dot{m}_C'' = \sum_{j=1}^{N_{het}} \frac{|\nu_{C,j}| M_{w,C}}{|\nu_{i,j}| M_{w,i}} R_{het,j} \tag{4.14}$$

$$\vec{n} \cdot \lambda_g \nabla T_g = \sum_{j=1}^{N_{het}} \Delta H_{R_{het,j}} \frac{|\nu_{C,j}| M_{w,C}}{|\nu_{i,j}| M_{w,i}} R_{het,j} + \epsilon_p \sigma \left(T_{p,s}^4 - \theta_R^4 \right) \tag{4.15}$$

where $\vec{n}$ is the normal vector, $\dot{m}_C''$ is the carbon mass flux (Stefan flow), $\rho_{g,s}$ is the gas density at the outer particle surface, and θ_R is radiation temperature.

During the char conversion process, an ash layer can be formed at the outer particle surface. For high ash contents and temperatures below the ash's melting point, the ash layer significantly influences the overall reaction rate at the last stages of char conversion. At high temperatures, the ash layer becomes softer and can quickly be released from the particle surface due to the Stefan flow and shear stress of the flow, especially if the ash content is low. For that reason, the influence of the ash layer on the particle shape has been neglected in the study, so the particle is assumed to consist of pure carbon. Furthermore, the particle's rotation and buoyancy effects are neglected. A detailed discussion of the impact of buoyancy can be found in [12].

4.2 Discretization, Numerical Scheme and Validation

The Reynolds numbers considered in this work are below 250. For that reason, the flow field is axis-symmetric [5], and the Navier-Stokes equations are solved in their axis-symmetric form. ANSYS™ Fluent™ V17.2 [27] was used to solve the governing equations, with second-order discretization in space and in time. To ensure that all the temperature, velocity, and species gradients were adequately resolved, especially in the boundary layer around the reacting particle, structured, quadrilateral control volumes were applied. Convergence and mesh independent study also was carried in [5]. The optimal initial mesh consists of 24000 control volumes, with the carbon particle considered as a solid zone, as illustrated in Figure 4.3.

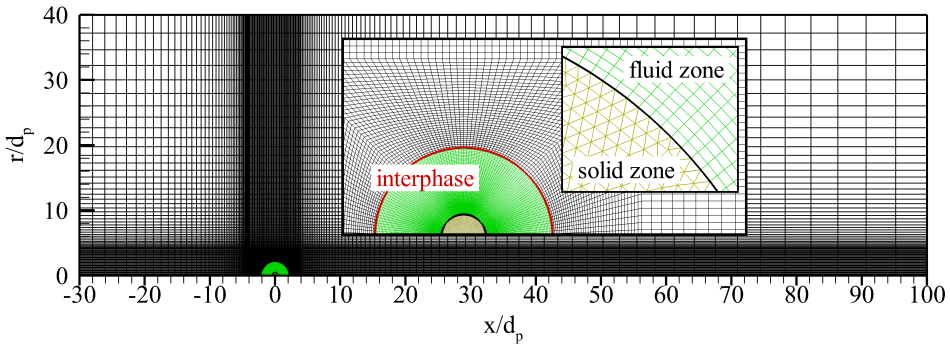

Fig. 4.3: Initial numerical mesh and zone definition investigation of particle shape development [20]

The numerical model applied was initially validated against the analytic one-film and two-film model, as reported in [14, 76]. In [77, 78], two research groups independently studied the

conversion of coal-char particles in different O_2/CO_2 and O_2/N_2 atmospheres. In [11], the numerical model was carefully validated against these experimental data and demonstrated very good agreement for different atmospheres and different oxygen concentrations. Additionally, the particle burning rates were compared against the data reported by Stauch and Maas [79] for a 100 µm particle in a quiescent atmosphere, and also demonstrated good agreement. It is worth noting that future validation work focuses on the HITECOM reactor, which allows single particles to be studied at defined gas velocities, compositions, and temperatures at pressures up to 40 bar [80]. To capture the changes in a particle's morphology, the computational mesh was adapted during the particle conversion process based on the local carbon consumption rate at the particle surface. The outer particle surface is discretized into a large number N_{sub} of sub surfaces $A_{p,k}$ as shown in Figure 4.4.

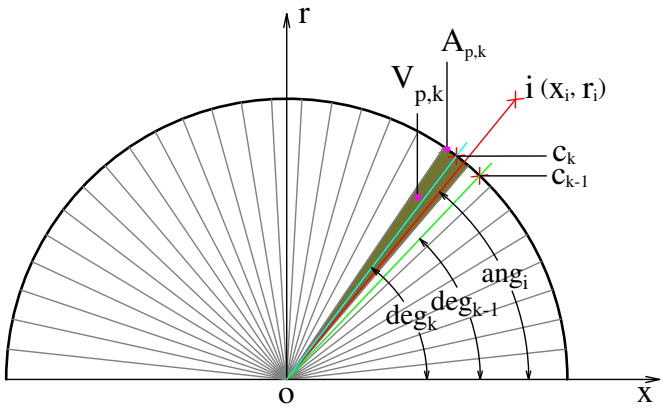

Fig. 4.4: Particle discretization [20]

The larger the sub surfaces, the more accurate the particle shape development obtained, but the more time is required. Here, 120 sub surfaces are used for an optimized solution. The corresponding particle sub volumes $V_{p,k}$ were estimated approximately based on the vertex coordinates. The consumed char at $A_{p,k}$ was used to estimate the decrease in $V_{p,k}$. Consequently, the $V_{p,k}$ after an interval of time Δt was calculated as

$$V_{p,k}^{t+\Delta t} = V_{p,k}^{t} - \dot{m}_{C,k} \frac{\Delta t}{\rho_{p,0}} \tag{4.16}$$

with

$$\dot{m}_{C,k} = A_{p,k} \sum_{j=1}^{N_{het}} \frac{|\nu_{C,j}| M_{w,C}}{|\nu_{i,j}| M_{w,i}} R_{het,j,k} \tag{4.17}$$

The decrease in volume leads the central point c_k of the sub surface $A_{p,k}$ to move towards the origin of the particle with the movement factor $scale_k$

$$scale_k = \sqrt[3]{\frac{V_{p,k}^{t+\Delta t}}{V_{p,k}^{t}}} \tag{4.18}$$

To adapt the mesh to the new particle shape, the vertex $i\,(x_i^t, r_i^t)$ with $deg_{k-1} \leq ang_i \leq deg_k$ (see Figure 4.4) in the dynamic zones is transposed to a new position $i\,(x_i^{t+\Delta t}, r_i^{t+\Delta t})$.

$$x_i^{t+\Delta t} = b\, x_i^t, \quad r_i^{t+\Delta t} = b\, r_i^t \tag{4.19}$$

The factor b is calculated based on the $scale_k$ and $scale_{k-1}$

$$b = a\, scale_k + (1 - a)\, scale_{k-1}, \quad a = \frac{ang_i - deg_{k-1}}{deg_k - deg_{k-1}} \tag{4.20}$$

In the case of $ang_i \leq deg_0$ or $deg_{N_{sub}-1} \leq ang_i$, the factor b equals to $scale_0$ or $scale_{N_{sub}-1}$, respectively. The particle shrinking results in compressed or stretched control volumes, producing a significantly lower mesh quality. To overcome this, the computational mesh was divided into a fixed mesh zone and a moving mesh zone, which are separated by the inter-phase line, as illustrated in Figure 4.3. The moving mesh zone contains the particle mesh and the control volumes around the particle. At the interface between the zones, additional control volume layers are inserted based on several adaptation criteria. This strategy results in an almost optimal mesh quality with up to 99 % conversion. The effects of the layering method and details of the mesh in the vicinity of the particle are illustrated in Figures 4.5 and 4.6 at 0 and 50 % particle conversion.

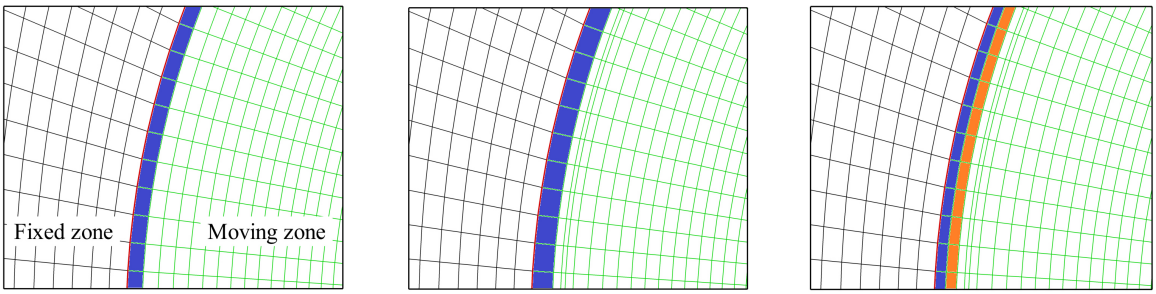

(a) initial situation (b) mesh deformation (c) adapted mesh

Fig. 4.5: Effect of layering method [20]

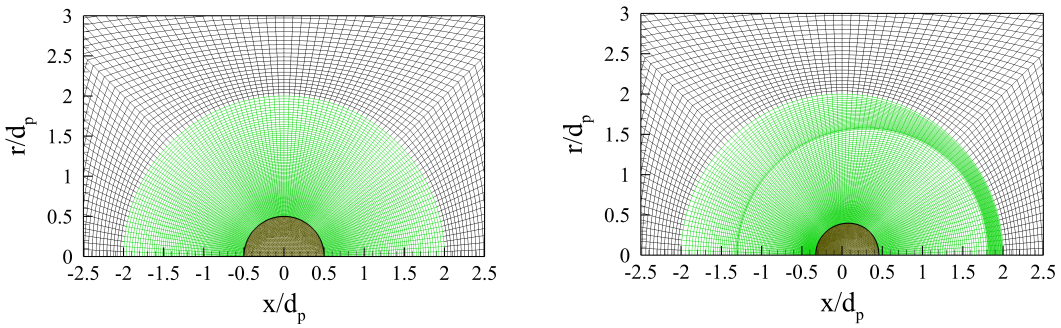

(a) 0 % conversion (b) 50 % conversion

Fig. 4.6: Computational mesh at 0 and 50 % carbon conversion. Only the dynamic mesh zone is illustrated [20]

4.3 Results

As indicated in the above description of the CFD model, the particle shape development depends on how the carbon consumption rate is distributed on the particle surface. The distribution of the carbon consumption rate is directly related to the structure of the boundary layer around the particle, which depends on the particle shape, particle size and particle Reynolds number.

4.3.1 Shape Development of an Isolated Small Char Particle

The conversion process undergone by a small spherical particle with a diameter of 8 µm as it traveled along its trajectory in the BYU entrained-flow gasifier was studied in detail by

Richter et al. [13]. However, particle shape development was not considered. For this reason, in this section the development of the shape of an 8 µm spherical particle was studied at low and high Reynolds numbers, Re=1 (u_{in}=1.049 m/s) and Re=150 (u_{in}=157.35 m/s). The gas conditions surrounding the particle are given in Table 4.2, corresponding to the point located in the lean zone. This explains why the inlet temperature is set relatively low (1480 K). An additional case with the gas velocity and components identical to the case of Re=150 but with a higher inlet temperature of 2400 K, representing the point located in the flame zone, was also investigated. The increase in the temperature condition leads to the decrease in the Reynolds number from 150 to 70. The speed of sound in the reacting gas flow at the temperature of 1480 K and 2400 K approximates 772.3 m/s and 983.0 m/s, respectively. Hence, the subsonic flow model is applicable to the gas flow.

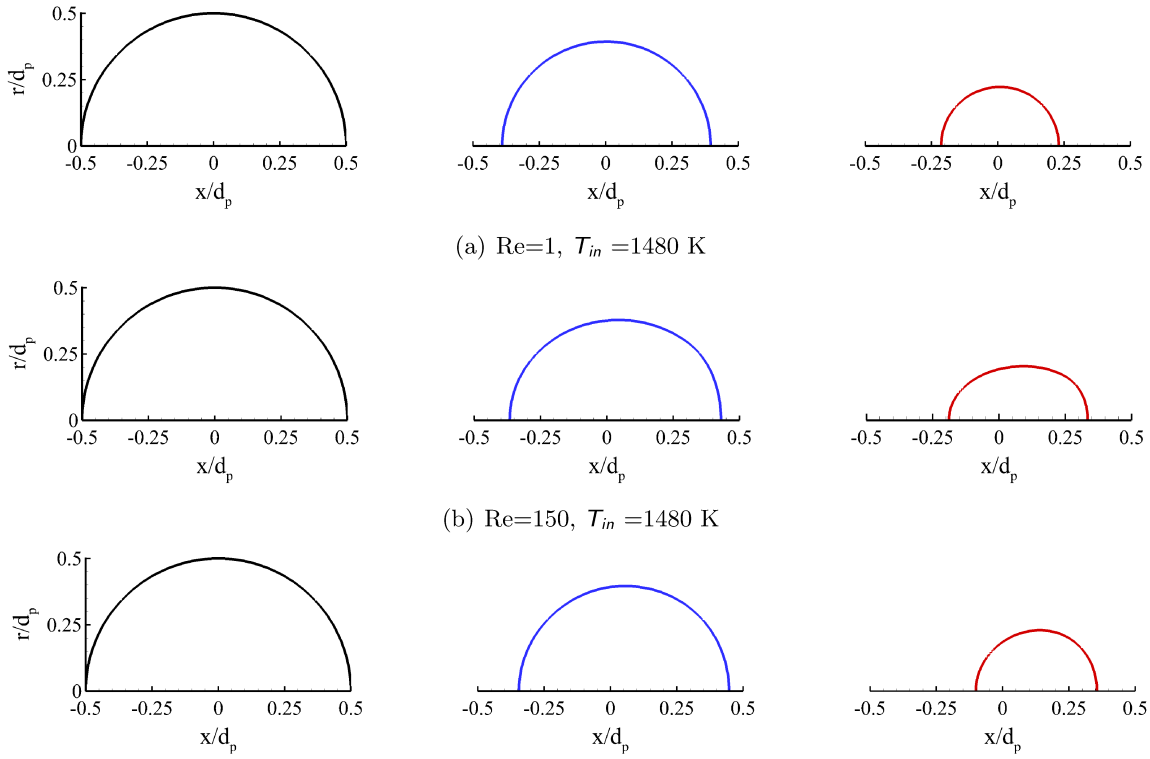

(a) Re=1, T_{in} =1480 K

(b) Re=150, T_{in} =1480 K

(c) Re=70, T_{in} =2400 K

Fig. 4.7: Shape development of a spherical char particle with an initial diameter of 8 µm at different Reynolds numbers and different char conversion levels: black lines – 0 %, blue lines – 50 %, red lines – 90 % [20]

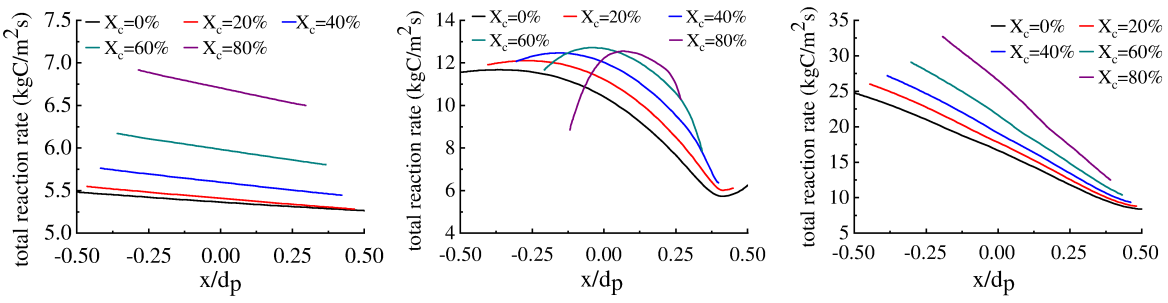

(a) Re=1, T_{in} =1480 K (b) Re=150, T_{in} =1480 K (c) Re=70, T_{in} =2400 K

Fig. 4.8: Char consumption rate over the conversion process on the outer surface of a spherical particle with an initial diameter of 8 µm corresponding to three cases in Figure 4.7 [20]

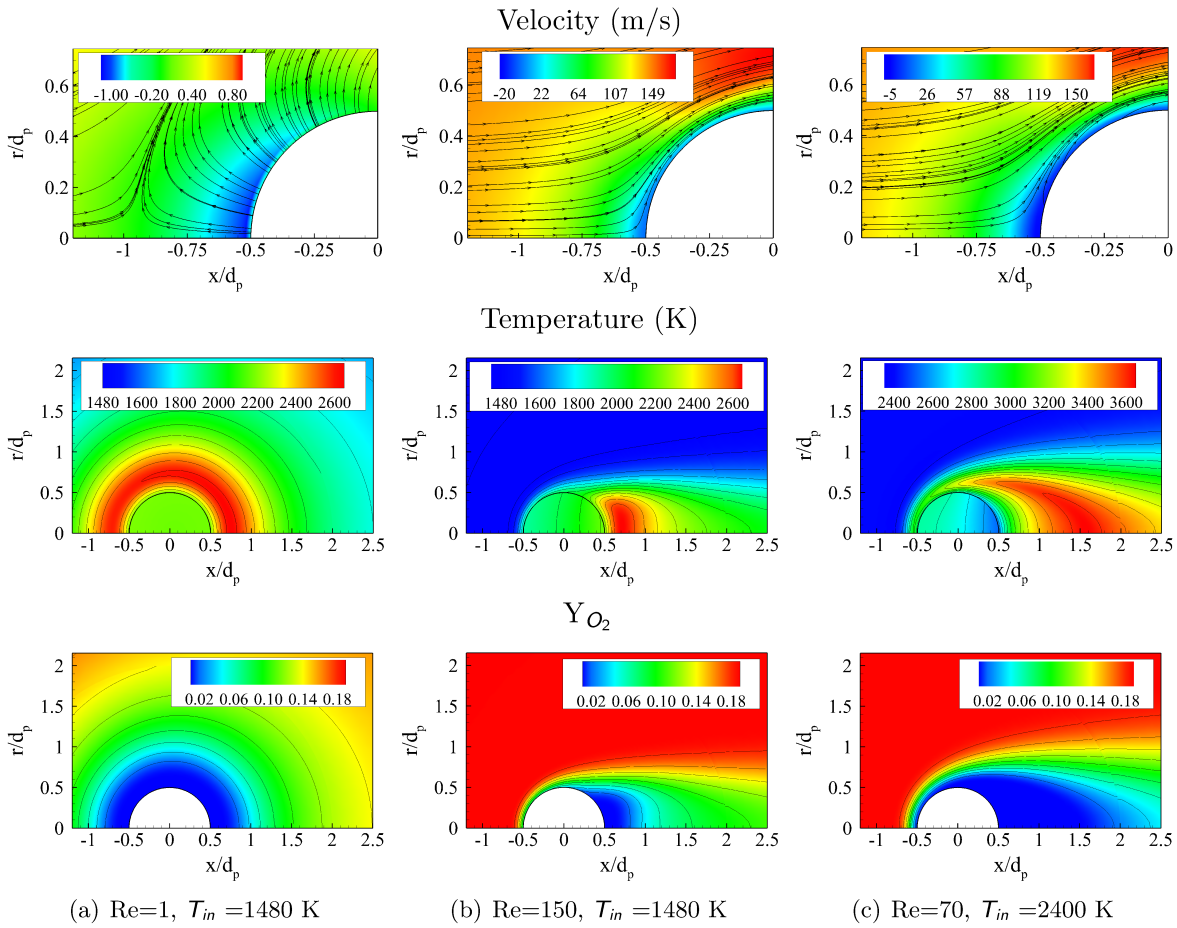

Fig. 4.9: Velocity, temperature, and oxygen distribution around an initial 8 µm spherical char particle at different conditions [20]

Figure 4.7 shows the resulting shape development for the 8 µm particle in the different reaction conditions. It can be seen that at a Reynolds number of 1 (Figure 4.7a) the particle remains spherical in a wide range of char conversion levels while at a Reynolds number of 150, the change in the particle shape is observed clearly at a high char conversion level, e.g. at 90 % in Figure 4.7b. The sphericity ϕ and the ratio of the longitudinal particle length to the diameter of the volume-equivalent sphere $\frac{l}{d_p}$, introduced in [5], are calculated based on the obtained numerical data to quantify the change in the particle shape. For Re=150 and T_{in}=1480 K at 90 % of the char conversion level, ϕ and $\frac{l}{d_p}$ decrease from 1 to 0.988 and from 1 to 0.917, respectively. When the particles enter the flame zone of a pressurized entrained-flow gasifier, a higher temperature is observed due to the oxidation of the volatile matters released from the particles during the pyrolysis process. At the higher temperature, the carbon consumption rate increases exponentially. The significantly enhanced carbon consumption rate has only a minor effect on shape development. As shown in Figure 4.7c, for the moderate Re of 70 and the inlet gas temperature of 2400 K, the particle shape remains nearly spherical (ϕ=0.9996 and $\frac{l}{d_p}$=1.0221 at 90 % of the char conversion level). The particle shape development depends directly on the carbon consumption rate distribution across the outer particle surface during the partial oxidation process.

Correspondingly, Figure 4.8 illustrates these distributions at different carbon conversion levels. These distributions indicate that the upstream side of the particle is consumed faster than the downstream side. As a result, the particle center shifts slightly in the direction of the flow. A considerable difference in the distribution between high and low Reynolds

numbers can be observed. The distribution is nearly linear for a Reynolds number of 1, while for a Reynolds number of 150 the distribution is non-linear, as shown in Figure 4.8a and Figure 4.8b, respectively. When the inlet temperature increases from 1480 K to 2400 K the carbon consumption rate becomes a linear distribution, as shown in Figure 4.8c. It can be seen that for linear distributions, the particle shape remains spherical. Only for distinct non-linear distributions can a deviation from a spherical particle shape be observed.

In addition, Figure 4.9 shows the velocity, temperature, and oxygen distribution in the vicinity of the particle. It can be seen clearly that the boundary layer is uniformly distributed across the particle at low Reynolds numbers. The boundary layer's thickness increases at lower Reynolds numbers and increases further due to the Stefan flow. The reaction regime corresponds to a classical two-film regime, e.g. as discussed in [11]. In this regime, oxygen is consumed in a flame sheet around the particle, and the process is significantly controlled by the diffusive mass transport towards the particle surface. At the particle surface, only the Boudouard reaction and the gasification reaction occur. As the Reynolds number increases, the system is shifted towards a kinetically controlled regime. The boundary layer's thickness is reduced, and the flame is shifted into a small region in the particle wake. The resulting non-uniform temperature and species distribution across the particle are responsible for the non-uniform char consumption and, therefore, its deviation from a spherical shape. Figure 4.10 shows the corresponding reaction rates, which substantiate the discussed results.

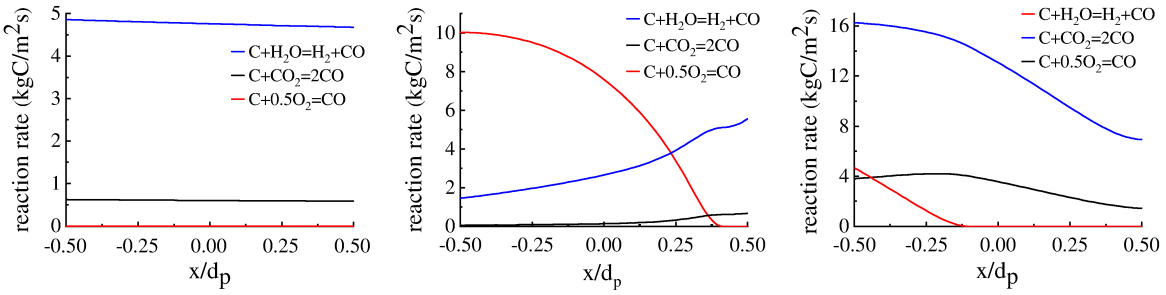

(a) Re=1, T_{in} =1480 K (b) Re=150, T_{in} =1480 K (c) Re=70, T_{in} =2400 K

Fig. 4.10: The distribution of the heterogeneous reaction rates on the outer surface of the spherical char particle with an initial diameter of 8 µm for different Reynolds numbers and inlet temperature conditions at t=0 s [20]

The question is: How is the overall char consumption affected by the particle shape? To answer that question, Figure 4.11 compares three cases.

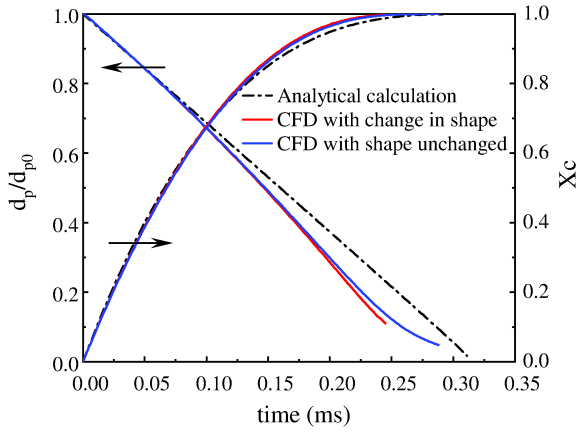

Fig. 4.11: The influence of particle shape development on the overall char conversion rate of an initial 8 µm spherical particle, Re =150, T_{in} =1480 K [20]

The first case (in red lines) is based on the results discussed above for an 8 µm particle at a Reynolds number of 150 and T_{in}=1480 K. The second case (in blue lines) is based on a similar model, but the particle shape was kept spherical. For this purpose, a global char consumption rate was estimated to define the particle size change so that the particle shrank uniformly. As a reference case (in dashed lines), described here as an analytic calculation, the carbon flux was estimated at the beginning of the conversion and averaged across the particle surface. If it is assumed that the carbon flux remains constant over time, the particle shape remains spherical, and the char conversion can be calculated directly with no need for CFD. From Figure 4.11 it can be seen that relatively slight deviations between the two CFD cases occur at conversion degrees above 85 %. It can be concluded that for a Reynolds number of 150, the shape development is not important for calculating the char conversion, but it becomes evident that the assumption of a constant carbon flux is not valid. The impact on the drag coefficient is discussed in detail in Section 4.4.

4.3.2 Shape Development of Larger Char Particles

The shape development of a spherical particle with a diameter of 263 µm was studied in this section. This diameter is the largest particle size in the underlying gasifier study [2]. According to Section 4.3.1, the particle's shape remains spherical at low Reynolds numbers, since the flame sheet around it is homogeneous. This was also confirmed for a 200 µm particle in [11]. For that reason, this section focuses on high Reynolds numbers. The particle Reynolds numbers were set to 100, 150, and 200 corresponding to the inlet velocity of 3.192 m/s, 4.786 m/s and 6.384 m/s, respectively. The gas temperature and composition are given in Table 4.2. The change in the particle shape for the 263 µm particle is shown in Figure 4.12.

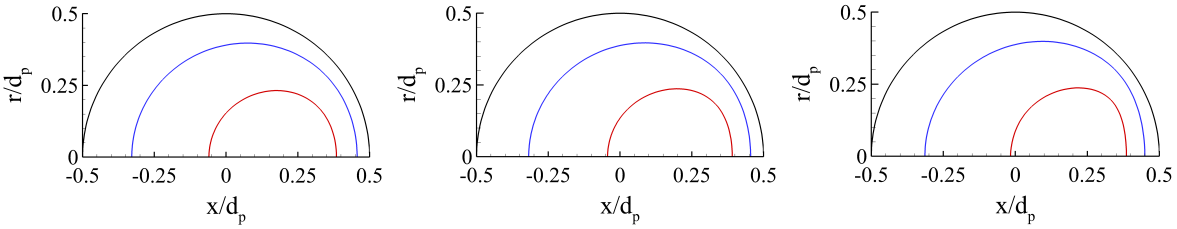

(a) Re=100 (b) Re=150 (c) Re=200

Fig. 4.12: Shape development of an initial 263 µm spherical particle at different Reynolds numbers and char conversion levels, T_{in} =1480 K: black lines – 0 %, blue lines – 50 % and red lines – 90 % [20]

From Figure 4.12a, it can be seen that at Reynolds numbers smaller than 100 the particle's shape remains almost spherical during the char conversion process. At Reynolds numbers above 100, as shown in Figure 4.12b and Figure 4.12c, the shape becomes non-spherical, with a different shape compared to the 8 µm particle. At a char conversion of 90 %, the particle sphericity and length-to-diameter ratio (ϕ , $\frac{l}{d_p}$) are (0.9990, 1.0320), (0.9970, 1.0540) and (0.9920, 1.0760) for Reynolds numbers of 100, 150, and 200, respectively.

Figure 4.13 shows the carbon consumption rate across the outer surface of the 263 µm spherical particle. A comparison with Figure 4.8b at t=0 s reveals a significant change in the characteristic distribution of the carbon consumption rate. For the large particle, the char consumption rate across the particle surface is nearly linear, except for the wake region, where a strongly non-linear distribution can be found. This reason accounts for the different shape development compared to an 8 µm particle.

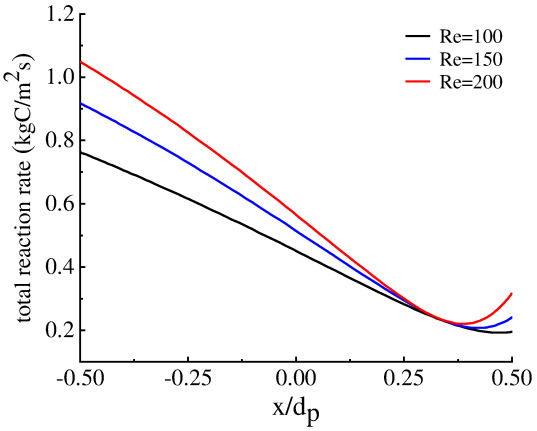

Fig. 4.13: Char consumption rate on outer surface of an initial 263 µm spherical particle at different Reynolds numbers, T_{in} =1480 K, t=0 s [20]

4.3.3 Shape Development of Non-Spherical Particles

The particle shape differs significantly from a spherical particle in several technical applications, e.g. biomass or waste gasification. For that reason, this section studies the shape development of typical non-spherical but axis-symmetric particles such as ellipsoids, oblates, cylinders, and double cones, as shown in Figure 4.1. As studied in previous works (e.g. see [13]), large particles mostly experience heating, drying and pyrolysis, and pass through the flame zone with only low or moderate char conversion. The transport and conversion of large particles play an important role in the reactor's overall performance. Therefore, the shape development of large particles is examined. All non-spherical particles feature a diameter of 263 µm (volume-equivalent to a spherical particle) and were embedded in the reacting flow parallel to their axis of symmetry under the ambient conditions given in Table 4.2.

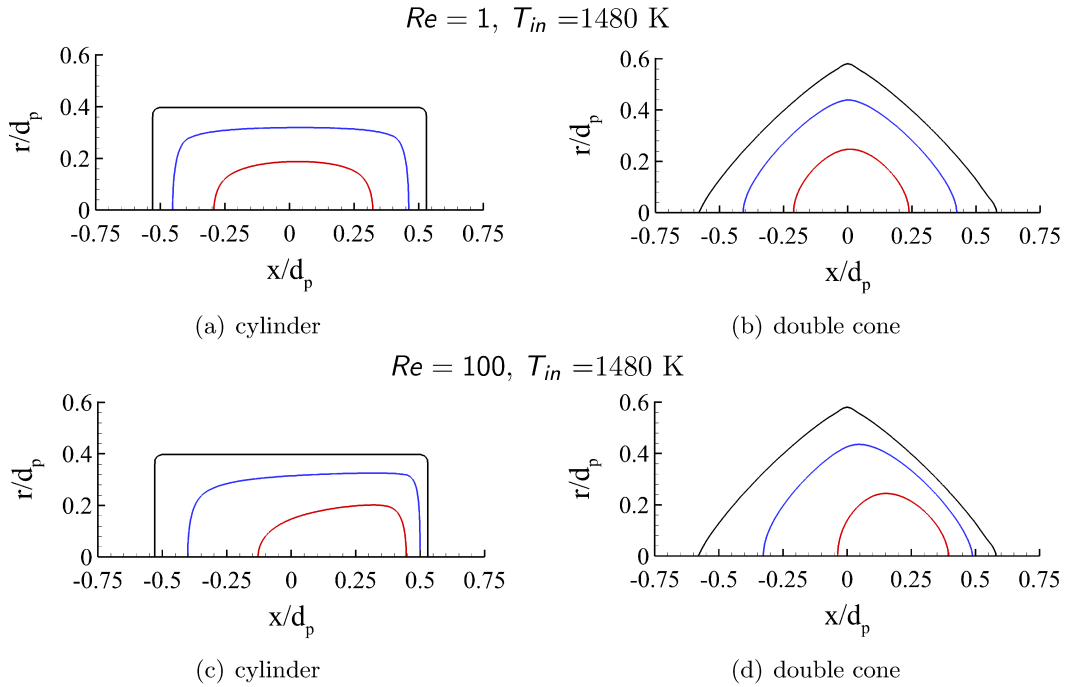

Fig. 4.14: The shape development of the cylindrical and double-conical particle at low and high Reynolds numbers, T_{in} =1480 K: black lines – 0 %, blue lines – 50 %, red lines – 90 % [20]

Figures 4.14a,b illustrate the shape evolution of cylindrical and double-conical particles at a Reynolds number of 1. From these illustrations, it can be seen that the shape of both particles is nearly constant, and all that happens during the conversion process is that sharp edges are rounded off. The particle sphericity ϕ and aspect ratio $\frac{l}{d_p}$ were (0.9520, 0.8400) for the cylinder and (0.9940, 1.107) for the double cone at a char conversion level of 90 %. At higher Reynolds numbers (Re=100), the flow field has a significant impact on the particle shapes, as shown in Figures 4.14 c,d. The final shape results from the non-constant char consumption rates across the particle surface, as shown in Figure 4.15. Especially at the particle edges, peaks in the carbon mass flux occur. As a result, the particles lose their sharp edges and their symmetry plane perpendicular to the axis of symmetry. At a 90 % conversion level, the sphericity and aspect ratios change to (0.9490, 0.9140) for the cylinder and (0.9930, 1.0860) for the double cone.

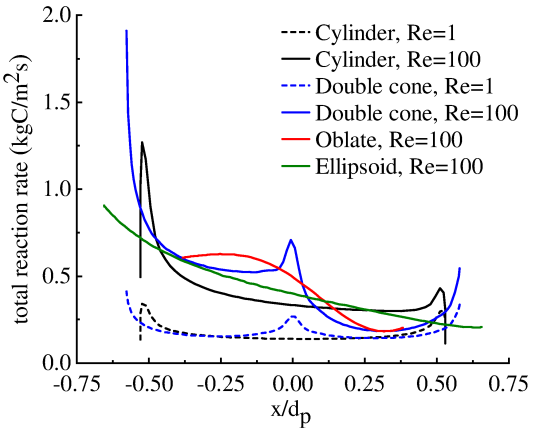

Fig. 4.15: Char consumption rate across the outer surface of non-spherical particles at different Reynolds numbers, T_{in} =1480 K, t=0 s [20]

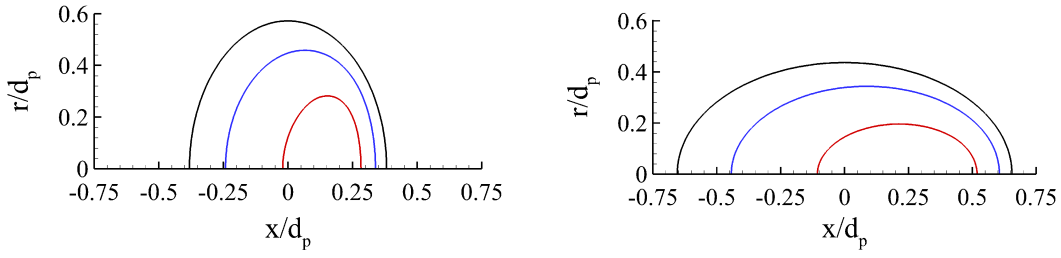

(a) oblate (b) ellipsoid

Fig. 4.16: The shape development of the oblate and ellipsoidal particle at Re =100 and T_{in} =1480 K: black lines – 0 %, blue lines – 50 %, red lines – 90 % [20]

Finally, the shape development of the oblate and ellipsoidal particle at a Reynolds number of 100 is shown in Figures 4.16. It can be seen that the flow field has only a moderate impact on the final shape. The particle sphericity ϕ and aspect ratio $\frac{l}{d_p}$ at a char conversion level of 90 % were (0.9290, 1.2450) and (0.9650, 0.8960) for the oblate and ellipsoidal particle, respectively. The shape development of the non-spherical particles reveals that the cylindrical particle and the double cone significantly change their shape, while the oblate and the ellipsoidal particles nearly retain their initial shapes even at higher Reynolds numbers.

4.4 Influence of Shape Development on the Drag Coefficient

In addition to the shape development of the large spherical and non-spherical particle studied above, an estimation of the relative deviation of the drag force coefficient between the particle shapes at the char conversion of 90 % and initial shapes under Re=100 is listed in Table 4.5, which shows the difference in the drag coefficients between the beginning of the char conversion process and at 90 %. The highest deviation of 11.6 % is for the double cone, and the lowest of 0.3 % corresponds to the ellipsoid. It can be seen that the change in the drag coefficient is not directly connected with the change in the sphericity of the particle but exhibits a correlation with the change in streamlines around the particle.

Tab. 4.5: Relative deviation of drag force coefficient between particle shapes at char conversion of 90 % and the initial shape under Re=100 for 263 µm particles [20]

shape	sphere	ellipsoid	oblate	cylinder	double cone
$\frac{\lvert\Delta\phi\rvert}{\phi}$, %	0.10	0.82	4.23	9.58	4.31
$\frac{\lvert c_{d,0}-c_d\rvert}{c_{d,0}}$, %	3.7	0.3	1.6	7.5	11.6

It is impossible to predict the shape development of a feedstock fed the entrained-flow gasifier accurately because of the following reasons: (1) The feedstock is characterized by inhomogeneous distributions in terms of the particle shape and size. (2) The particle Reynolds number in the entrained-flow gasifier is not constant due to the motion of the particle and differently local gas conditions. (3) Even if the feedstock has a homogeneous particle shape, and the Reynolds number is assumed to be constant during the conversion process of each particle, the shape of small particles develops differently from the shape of large particles.

As mentioned in [2, 70], the particle Reynolds number can be higher than 2500 under the operation conditions of elevated entrained-flow gasifiers, but the particle experiences laminar flows at most of its residence time. According to [13], small particles are completely converted but larger particles, for example those above the mean size, leave the entrained-flow gasifier with a low conversion level. Thus, the conversion process of the larger particles plays an important role in deciding the performance and efficiency of the entrained-flow gasifier. From these points of view, the shape development of the particle with an average diameter in the laminar flow regime can approximately represent the shape development of the feedstock during the conversion process.

The Pressurized Entrained Flow Reactor (PEFR) developed by the Commonwealth Scientific and Industrial Research Organization (CSIRO) [50] have been used as a laboratory reactor to validate a new char conversion model and to estimate the effect of the particle shape development. The particle size of the PEFR's feedstock ranges from 30 µm to 250 µm [15, 81]. Therefore, several particles with a mean diameter of 125 µm (volume-equivalent to a spherical particle) are studied in terms of how their shape development affects the drag coefficient.

Tab. 4.6: Drag coefficient $c_{d,0}$ depending on particle Reynolds number for different initial particle shapes

Shape Re	10	25	50	75	100	150	200	250
Sphere	4.285	2.355	1.570	1.259	1.085	0.886	0.771	0.692
Cylinder	4.251	2.270	1.472	1.159	0.985	0.788	0.676	0.602
Double cone	4.681	2.662	1.848	1.530	1.350	1.135	1.000	0.899

First, the drag coefficient for initial shape $c_{d,0}$ depending on the Reynolds number for the particles in question, such as a sphere, cylinder and double cone, is calculated and given in

Table 4.6. Next, the conversion process of those particles at different Reynolds numbers from 1 to 250 is studied. Consequently, the change in the sphericity of those particle is tracked with the carbon conversion level for each Reynolds number concerning. The Reynolds numbers, under which the change in the sphericity reaches limitations, are determined for each of the particles. The limitation of change in the sphericity shows the limitation of change in the shape. Finally, the shapes corresponding to different carbon conversion levels obtained from the conversion process under the determined Reynolds numbers are conducted to calculate the drag coefficient in a range of Reynolds numbers from 10 to 250. As a result, the limitations of both the drag coefficient and the particle sphericity in the laminar flow regime are revealed. Average values of the drag coefficient and sphericity limitation are considered as dynamic models to track particle's trajectories, and to calculate the heat and mass transfer coefficient between those particles and gas phase in a CFD-based modeling of the PEFR in Chapter 6.

4.4.1 Drag Coefficient for Initially Spherical Shape

The development of the sphericity and the shape of an initially 125 µm spherical particle during the char conversion process at different particle Reynolds numbers are illustrated in Figure 4.17. During the calculation, to isolate the effect of Reynolds numbers and to capture the effects of shape change only, the Reynolds number was kept constant by adjusting the inlet velocity while the particle diameter was reduced due to the char conversion.

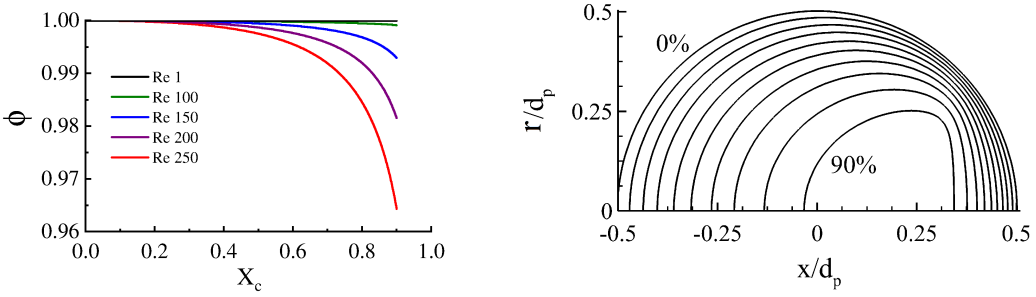

(a) particle sphericity

(b) particle shape development at Re=250

Fig. 4.17: The development of sphericity of an initially 125 µm spherical char particle at different Reynolds numbers and the shape development of that particle at Re =250 at different char conversion levels

Tab. 4.7: Drag coefficient $c_{d,max}$ based on the shape development of the initial spherical particle with a diameter of 125 µm at Re=250 (see Figure 4.17b)

Re	X_c	0.1	0.2	0.3	0.4	0.5	0.6	0.7	0.8	0.9
10		4.294	4.298	4.314	4.316	4.339	4.357	4.405	4.442	4.613
25		2.360	2.363	2.373	2.375	2.390	2.401	2.433	2.459	2.572
50		1.574	1.576	1.583	1.585	1.596	1.605	1.628	1.650	1.737
75		1.263	1.265	1.271	1.272	1.281	1.289	1.309	1.328	1.403
100		1.088	1.089	1.095	1.096	1.104	1.111	1.129	1.146	1.213
150		0.889	0.890	0.894	0.895	0.902	0.907	0.921	0.936	0.992
200		0.773	0.774	0.777	0.778	0.783	0.788	0.800	0.811	0.859
250		0.693	0.694	0.697	0.698	0.702	0.706	0.716	0.726	0.767

The changes in the particle sphericity with the char conversion process corresponding to different particle Reynolds numbers are shown in Figure 4.17a. It is clear that the particle

sphericity remains nearly constant during the conversion process at Reynolds numbers below 100. In contrast, at particle Reynolds numbers higher than 100, the particle sphericity decreases gradually until 40 % of the char conversion and decreases rapidly at the high carbon conversion levels. The maximum reduction in particle sphericity occurs at the particle Reynolds number of 250. The dependency of the particle sphericity to the char conversion level for particle Reynolds number of 250 is expressed in Eq. (4.21). The coefficients of Eq. (4.21) were determined by least-squares fitting using Matlab software.

$$\begin{aligned}\phi_{min}^{sph} = &-4.461X_c^8 + 13.460X_c^7 - 16.640X_c^6 + 10.710X_c^5 \\ &- 3.799X_c^4 + 0.709X_c^3 - 0.066X_c^2 + 0.0014X_c + 1.0 \quad (R^2 = 1)\end{aligned} \tag{4.21}$$

Figure 4.17b shows the shapes corresponding to the different char conversion levels from 0 to 90 %, obtained from a CFD simulation of the initially 125 µm spherical particle at the constant Reynolds number of 250.

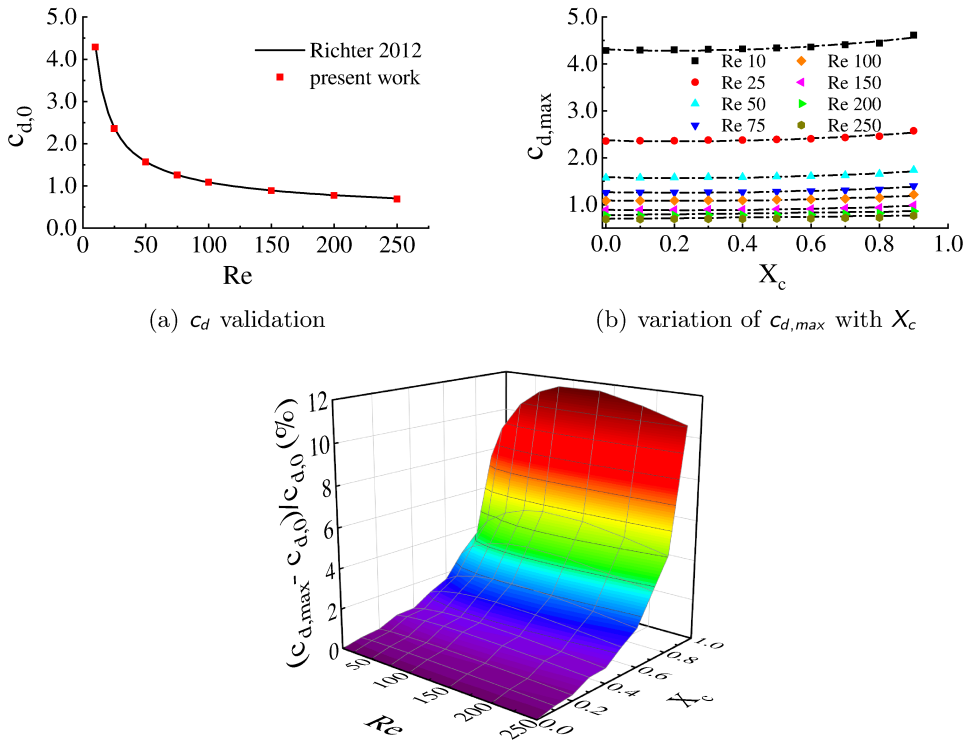

(a) c_d validation

(b) variation of $c_{d,max}$ with X_c

(c) relative deviation

Fig. 4.18: The dependent function of the drag coefficient on the shape development of an initial 125 µm spherical particle

Figure 4.18a shows that the drag coefficients $c_{d,0}$ for a spherical shape (Table 4.6) are in good agreement with the published data [5]. At Re=250 where the particle sphericity reduction is the highest for all char conversion levels, the change in the particle shape is strongest, consequently, the drag coefficient increase is the highest. Hence, to determine the maximum possible drag coefficients, $c_{d,max}$, at different char conversion levels and Reynolds numbers in the laminar flow regime, the particle shapes at different conversion levels from the calculation with a constant Reynolds number of 250 (see Figure 4.17b) were used to conduct steady-state calculations for Reynolds numbers of 10 to 250. The results of drag coefficient are shown in Table 4.7 and Figure 4.18b. Correspondingly, the relative differences of the drag coefficient are illustrated in Figure 4.18c. The maximum possible drag coefficients depend on both the

Reynolds number and char conversion level. A correlation for the maximum possible drag coefficients, $c_{d,max}$, as a function of the char conversion level, X_c, and Reynolds number, Re, can be expressed as Eq. (4.22). The coefficients of Eq. (4.22) are determined by least squares fitting using Matlab software, and the results are as in Eq. (4.23) with $R^2 = 0.9999$.

$$c_{d,max} = a_0 + a_1 X_c + a_2 X_c^2 + \frac{b_0 + b_1 X_c}{Re} + \frac{c_0 + c_1 X_c}{\sqrt{Re}} \tag{4.22}$$

$$c_{d,max} = 0.1626 - 0.1163 X_c + 0.1245 X_c^2 + \frac{17.67 - 1.733 X_c}{Re} + \frac{7.449 + 1.038 X_c}{\sqrt{Re}} \tag{4.23}$$

Figure 4.18c shows the relative difference in the drag coefficient, $(c_{d,max} - c_{d,0})/c_{d,0}$. The maximal is 11.7 % at Re=100 and X_c=90 %. The particle Reynolds number depends on the gas-phase local conditions and particle size. Therefore, it changes continuously with the movement of the particle inside an entrained-flow gasifier. It is thus impossible to know the particle shape, and hence the particle sphericity and drag coefficient, at a given char conversion level exactly. However, it is certain that in a laminar flow regime, the particle sphericity ϕ and the drag coefficient c_d at a given Re and X_c can be in a range from ϕ_{min}^{sph} to 1 and from $c_{d,0}$ to $c_{d,max}$, respectively. Hence, their average values of them, $\bar{\phi}$ and $\bar{c}_d$, can be used for tracking particles in an entrained-flow gasifier.

$$\bar{\phi}_{sph} \approx 0.5(1 + \phi_{min}^{sph}) \tag{4.24}$$

$$\bar{c}_d = 0.5(c_{d,0} + c_{d,max}) \tag{4.25}$$

Based on the data in Table 4.6, the drag coefficient $c_{d,0}$ corresponding to a spherical particle as a function of Reynolds number is

$$c_{d,0,sph} = 0.1678 + \frac{18.01}{Re} + \frac{7.407}{\sqrt{Re}} \quad (R^2 = 1) \tag{4.26}$$

4.4.2 Drag Coefficient for Initially Non-Spherical Particles

First, the shape development of a 125 µm cylinder and its sphericity at different particle Reynolds numbers during the char conversion process are illustrated in Figure 4.19. Figure 4.19a shows changes in the relative particle sphericity with the conversion process at different particle Reynolds numbers from 1 to 250. The particle sphericity of the cylinder increases with the char conversion level at all the particle Reynolds numbers. Obviously, the higher the particle sphericity is, the closer the particle shape is to a sphere, and the lower the drag coefficient is. The highest increase in sphericity ratio occurs at Re=1 (corresponding to the minimum possible drag coefficient) and the lowest happens at Re=250 (corresponding to the maximum possible drag coefficient). A polynomial function could be used to demonstrate the dependency of particle sphericity ratio on the char conversion level as it is expressed as Eq. (4.27) for Re=1, and Eq. (4.28) for Re=250.

$$\begin{aligned}\left(\frac{\phi_{max}}{\phi_0}\right)_{cy} = &- 0.765 X_c^7 + 2.441 X_c^6 - 3.255 X_c^5 + 2.261 X_c^4 - 0.806 X_c^3 \\ &+ 0.0277 X_c^2 + 0.170 X_c + 1.0 \quad (R^2 = 1)\end{aligned} \tag{4.27}$$

$$\begin{aligned}\left(\frac{\phi_{min}}{\phi_0}\right)_{cy} = &0.368 X_c^6 + 1.091 X_c^5 - 1.374 X_c^4 + 0.961 X_c^3 \\ &- 0.472 X_c^2 + 0.211 X_c + 1.0 \quad (R^2 = 1)\end{aligned} \tag{4.28}$$

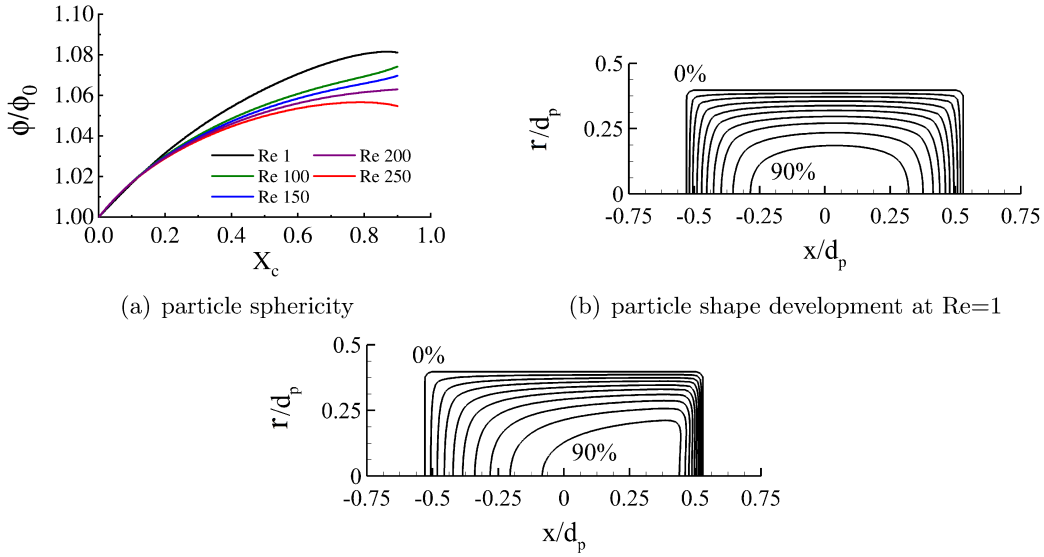

(a) particle sphericity

(b) particle shape development at Re=1

(c) particle shape development at Re=250

Fig. 4.19: The development of the shape and sphericity of an initial 125 µm cylinder at different Reynolds numbers over the char conversion process

The shape development at Re=1 (Figure 4.19b) and Re=250 (Figure 4.19c) were used to determine the minimum and maximum limits of the drag coefficient for the cylinder, respectively. Similar to spherical particles, for each shape extracted from Figure 4.19b and Figure 4.19c, steady-state simulations with the Reynolds numbers from 10 to 250 were conducted to calculate the drag coefficient limits. As a result, these limiting drag coefficients c_d are shown in Table 4.8.

From the data in Table 4.8 and Table 4.6, the ratio of $c_d/c_{d,0}$ is calculated and illustrated in Figure 4.20. Figure 4.20a shows the relative drag coefficient, based on the limiting drag

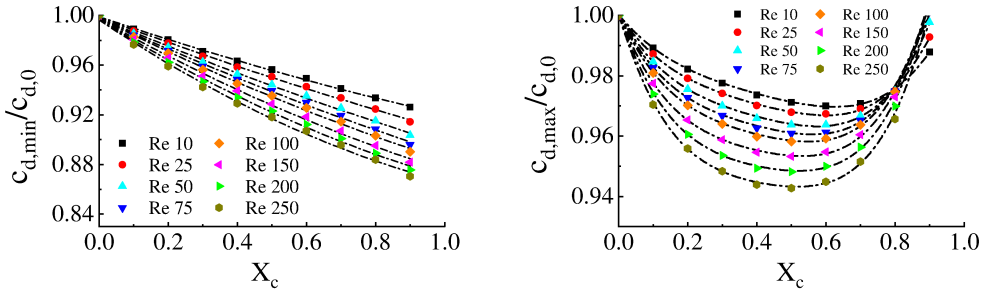

(a) minimal ratio of $c_d/c_{d,0}$

(b) maximal ratio of $c_d/c_{d,0}$

Fig. 4.20: The dependence of the ratio of $c_d/c_{d,0}$ on the carbon conversion level X_c and Reynolds number Re of an initial 125 µm cylinder

coefficients c_d corresponding to the shapes in Figure 4.19b, as a minimal ratio, $c_{d,min}/c_{d,0}$. A polynomial function with an order of 2 regarding the char conversion level X_c is used to express the minimum ratio in the form of Eq. (4.29). The coefficients of Eq. (4.29) are determined by least squares fitting using Matlab software as shown in Eq. (4.30) ($R^2 = 0.996$)

$$\left(\frac{c_{d,min}}{c_{d,0}}\right)_{cy} = a_0 + a_1 X_c + a_2 X_c^2 + \frac{bX_c}{1+Re} + \frac{cX_c}{1+\sqrt{Re}} \tag{4.29}$$

Tab. 4.8: Drag coefficient c_d based on the shape development of the initial cylindrical particle with a diameter of 125 µm at Re=1 and Re=250 (see Figure 4.19b, c)

Re	X_c	0.1	0.2	0.3	0.4	0.5	0.6	0.7	0.8	0.9
(Re=1)										
10		4.204	4.169	4.128	4.094	4.065	4.035	4.001	3.969	3.937
25		2.241	2.219	2.195	2.175	2.158	2.139	2.119	2.098	2.075
50		1.450	1.434	1.417	1.402	1.390	1.377	1.362	1.347	1.330
75		1.141	1.127	1.112	1.100	1.089	1.078	1.066	1.053	1.039
100		0.968	0.955	0.941	0.931	0.921	0.911	0.901	0.889	0.877
150		0.773	0.761	0.750	0.740	0.732	0.724	0.715	0.706	0.695
200		0.662	0.651	0.640	0.632	0.624	0.617	0.609	0.601	0.592
250		0.588	0.577	0.567	0.559	0.553	0.546	0.539	0.532	0.524
(Re=250)										
10		4.205	4.176	4.156	4.139	4.129	4.124	4.127	4.144	4.200
25		2.240	2.222	2.211	2.202	2.197	2.195	2.199	2.213	2.253
50		1.449	1.436	1.428	1.422	1.419	1.419	1.423	1.435	1.469
75		1.139	1.128	1.121	1.116	1.114	1.115	1.119	1.130	1.161
100		0.966	0.955	0.949	0.945	0.943	0.944	0.949	0.960	0.988
150		0.770	0.761	0.756	0.752	0.751	0.752	0.757	0.767	0.792
200		0.659	0.650	0.645	0.642	0.641	0.642	0.647	0.656	0.679
250		0.584	0.575	0.571	0.568	0.567	0.596	0.573	0.581	0.603

$$\left(\frac{c_{d,min}}{c_{d,0}}\right)_{cy} = 0.9987 - 0.2188X_c + 0.0327X_c^2 - \frac{1.151X_c}{1+Re} + \frac{0.9014X_c}{1+\sqrt{Re}} \tag{4.30}$$

Similarly, Figure 4.20b, based on the limiting drag coefficients c_d corresponding to the shapes in Figure 4.19c, shows the maximum of the relative drag coefficient $c_{d,max}/c_{d,0}$. A polynomial function with an order of 4 regarding char conversion level X_c is used to express the maximal ratio as shown in Eq. (4.31). After fitting, the maximal function is read as in Eq. (4.32) ($R^2 = 0.965$)

$$\left(\frac{c_{d,max}}{c_{d,0}}\right)_{cy} = a_0 + a_1X_c + a_2X_c^2 + a_3X_c^3 + a_4X_c^4 + \frac{bX_c^{1.6}}{1+Re^{0.7}} + \frac{cX_c}{1+\sqrt{Re}} \tag{4.31}$$

$$\left(\frac{c_{d,max}}{c_{d,0}}\right)_{cy} = 1 - 0.3729X_c + 0.888X_c^2 - 1.251X_c^3 + 0.7537X_c^4 - \frac{1.495X_c^{1.6}}{1+Re^{0.7}} + \frac{1.068X_c}{1+\sqrt{Re}} \tag{4.32}$$

Next, an initial 125 µm double cone was studied in terms of how its shape development affects its sphericity and drag coefficient. Figure 4.21 shows the relative sphericity and shape of that particle at different carbon conversion levels and different Reynolds numbers. The relative sphericity increases with carbon conversion level for all Reynolds numbers with the highest value at Re=100 (corresponding to the minimum possible drag coefficient) and the lowest value at Re=250 (corresponding to the maximum possible drag coefficient), as shown in Figure 4.21a. The limiting relative sphericity of ϕ_{max}/ϕ_0 and ϕ_{min}/ϕ_0 are considered as polynomial functions of the carbon conversion level X_c. The finding functions of relative sphericity are shown as in the following equations

$$\left(\frac{\phi_{max}}{\phi_0}\right)_{dc} = -0.043X_c^4 + 0.107X_c^3 - 0.116X_c^2 + 0.099X_c + 1.0 \quad (R^2 = 1) \tag{4.33}$$

$$\left(\frac{\phi_{min}}{\phi_0}\right)_{dc} = \frac{-38.48X_c^2 + 19.40X_c + 20.39}{X_c^3 - 36.90X_c^2 + 17.36X_c + 20.40} \quad (R^2 = 0.998) \tag{4.34}$$

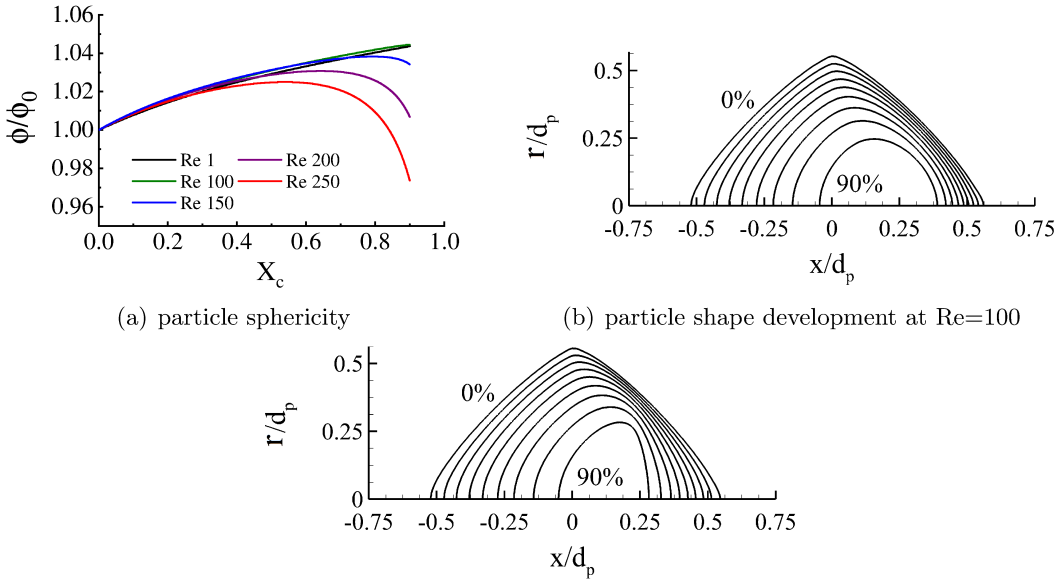

(a) particle sphericity

(b) particle shape development at Re=100

(c) particle shape development at Re=250

Fig. 4.21: Shape and sphericity development of an initial 125 µm double cone at different Reynolds numbers

Similar to the cylindrical particle, the shape development at Re=100, Figure 4.21b, and Re=250, Figure 4.21c, were used to determine the minimum and maximum limits of the drag force coefficient, respectively. For each shape extracted from Figure 4.21b and Figure 4.21c, steady-state simulations with the Reynolds numbers from 10 to 250 were conducted to calculate the drag force coefficient limits. As a result, these limiting drag force coefficients c_d are shown in Table 4.9.

From the data on the limiting drag coefficients c_d in Table 4.9 and $c_{d,0}$ for the double cone in Table 4.6, the ratio of $c_d/c_{d,0}$ was calculated and illustrated in Figure 4.22.

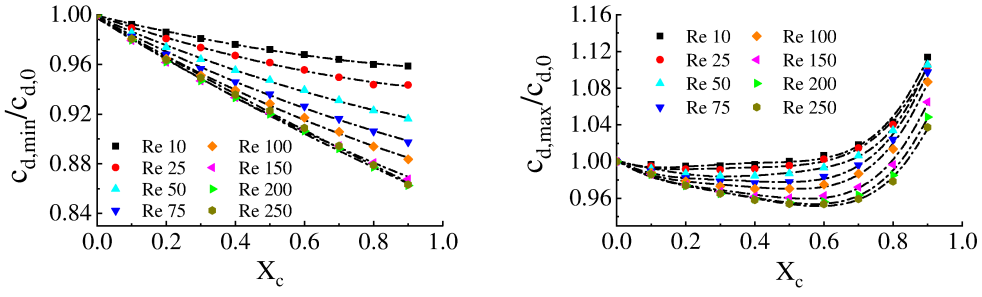

(a) minimal ratio of $c_d/c_{d,0}$

(b) maximal ratio of $c_d/c_{d,0}$

Fig. 4.22: The dependence of the ratio of $c_d/c_{d,0}$ on the carbon conversion level X_c and Reynolds number Re for an initially 125 µm double cone

According to Figure 4.22a, $c_{d,min}/c_{d,0}$ at different Reynolds numbers is a second-order polynomial function of X_c, and based on Figure 4.22b, $c_{d,max}/c_{d,0}$ is a fourth-order polynomial function of X_c. Using the Matlab software fitting tools, the fitting functions of $c_{d,min}/c_{d,0}$ and $c_{d,max}/c_{d,0}$ were determined and expressed as Eq. (4.35) ($R^2 = 0.997$) and Eq. (4.36) ($R^2 = 0.995$), respectively.

$$\left(\frac{c_{d,min}}{c_{d,0}}\right)_{dc} = 1 - 0.2696X_c + 0.0352X_c^2 - \frac{1.604X_c}{1+Re} + \frac{1.417X_c}{1+\sqrt{Re}} \tag{4.35}$$

Tab. 4.9: Drag coefficient c_d based on the shape development of the initial double cone with a diameter of 125 µm at Re=100 and Re=250 (see Figure 4.21b, c)

Re	X_c	0.1	0.2	0.3	0.4	0.5	0.6	0.7	0.8	0.9
(Re=100)										
10		4.644	4.615	4.591	4.570	4.550	4.531	4.512	4.493	4.488
25		2.633	2.2610	2.591	2.574	2.559	2.543	2.528	2.515	2.511
50		1.821	1.799	1.781	1.765	1.751	1.736	1.720	1.705	1.693
75		1.503	1.481	1.463	1.447	1.432	1.417	1.402	1.386	1.373
100		1.323	1.302	1.284	1.268	1.253	1.238	1.222	1.206	1.192
150		1.112	1.092	1.075	1.060	1.045	1.031	1.016	1.000	0.985
200		0.979	0.961	0.946	0.933	0.920	0.906	0.892	0.877	0.862
250		0.882	0.867	0.854	0.841	0.830	0.817	0.804	0.790	0.776
(Re=250)										
10		4.665	4.657	4.658	4.665	4.682	4.713	4.767	4.881	5.213
25		2.648	2.640	2.638	2.641	2.650	2.668	2.701	2.796	2.938
50		1.833	1.823	1.819	1.819	1.823	1.836	1.860	1.911	2.042
75		1.514	1.502	1.496	1.494	1.496	1.505	1.524	1.567	1.679
100		1.333	1.321	1.313	1.309	1.310	1.316	1.332	1.368	1.467
150		1.119	1.106	1.098	1.092	1.090	1.093	1.104	1.131	1.209
200		0.985	0.973	0.965	0.958	0.955	0.956	0.963	0.984	1.048
250		0.887	0.876	0.868	0.862	0.858	0.858	0.863	0.880	0.933

$$\left(\frac{c_{d,max}}{c_{d,0}}\right)_{dc} = 1 - 0.3504X_c + 0.7164X_c^2 - 1.437X_c^3 + 1.089X_c^4 - \frac{3.252X_c}{1+Re^{0.7}} + \frac{3.096X_c}{1+\sqrt{Re}} \tag{4.36}$$

Based on the 2D graph in Figure 4.20 and Figure 4.22, 3D limiting surfaces of the drag coefficient are plotted on the Cartesian coordinate in Figure 4.23.

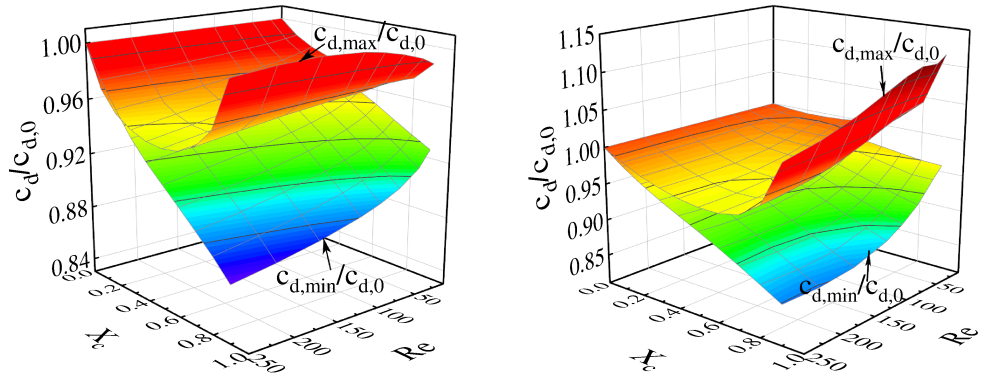

(a) cylinder (b) double cone

Fig. 4.23: Limiting surfaces of the relative drag coefficient for the cylinder and double cone

$c_d/c_{d,0}$ for the non-spherical particles investigated in this study could vary in the range of $c_{d,min}/c_{d,0}$ to $c_{d,max}/c_{d,0}$. Moreover, ϕ/ϕ_0 lies in the range of ϕ_{min}/ϕ_0 to ϕ_{max}/ϕ_0. Therefore, the mean values, $\bar{c}_d$ and $\bar{\phi}$, should be used for drag force calculation and the heat and mass transfer coefficients between the particle and gas phase.

$$\bar{\phi} = 0.5\left(\frac{\phi_{min}}{\phi_0} + \frac{\phi_{max}}{\phi_0}\right)\phi_0 \tag{4.37}$$

$$\bar{c}_d = 0.5\left(\frac{c_{d,min}}{c_{d,0}} + \frac{c_{d,max}}{c_{d,0}}\right) c_{d,0} \tag{4.38}$$

Based on the data in Table 4.6, the drag coefficients $c_{d,0}$ corresponding to the initial shape of the cylinder and double cone are given in Eq. (4.39) and Eq. (4.40), respectively.

$$c_{d,0,cy} = 0.07327 + \frac{19.03}{Re} + \frac{7.192}{\sqrt{Re}} \quad (R^2 = 1) \tag{4.39}$$

$$c_{d,0,dc} = 0.3269 + \frac{17.12}{Re} + \frac{8.343}{\sqrt{Re}} \quad (R^2 = 1) \tag{4.40}$$

4.5 Discussion

First, the particle shape development study is aimed at high-temperature conversion processes, where the ash material is melted and becomes dynamic, enabling it can be removed from the outer particle surface due to the drag force and Stefan flow. Therefore, the presence of the ash material can be ignored when the particle shape development is considered in the drag model. At lower temperatures than the ash melting point, an ash layer around a rich-carbon core can be formed. In that case, the particle shape should be kept constant during the char conversion process when the fragmentation of the ash layer does not occur.

Second, focusing on the laminar flow regime, where the gas flow surrounding an isolated chemically reacting particle is axis-symmetric, the 2D model presented in the current work is suitable to study the particle shape development. In the transient and turbulent flow regimes, the gas flow around the particle becomes asymmetric, leading to an asymmetric distribution of the carbon consumption rate on the outer particle surface. Hence, a 3D model should be developed to predict the change in the particle shape during the char conversion process.

Finally, since the char conversion is considered in the bulk diffusion-controlled regime (Regime III), the carbon consumption only occurs at the outer surface of the particle. Therefore, the changes in the particle volume and shape reach a maximum for each char conversion level. When the char particle is consumed in the pore-diffusion regime (Regime II), the carbon is consumed on the outer particle surface and inside the volume of the particle . Therefore, the change in particle shape does not relate to the char conversion level but directly involves the change in the particle volume, hence the particle size. For that reason, the char conversion level X_c in the correlation of the drag coefficient c_d and the particle sphericity ϕ should be replaced by a term of $\left[1 - (d_p/d_{p,0})^3\right]$.

4.6 Conclusion

The present work considers the development of spherical and non-spherical particles' shape under conditions similar to the flame zone in an industrial entrained-flow gasifier. Due to the high temperatures around the particle, the heterogeneous reactions occur in a regime controlled by pore diffusion and film diffusion, which legitimates the model's assumption that the particle shrinks during the conversion while its properties such as density, porosity, and specific surface area are assumed to be constant. Based on particle-resolved studies that examine the change in the particle shape during its conversion process, the following conclusions can be drawn:

1. The particle shape development depends on the particle Reynolds number and its initial shape.
2. Spherical particles remain nearly constant at low Reynolds numbers.

3. Non-spherical particles with low initial sphericity can significantly change their shape during the conversion process.
4. Even if the development of the char particles' shape significantly influences their trajectory, its influence on the overall char conversion is only minor.
5. Dynamic models for the drag coefficient and the particle sphericity, taking the particle shape development into account, are introduced to improve the accuracy of particle trajectories inside an entrained-flow gasifier and the char conversion rate.

5 Intraparticle Phenomena and Advanced Parameters for Char Conversion Models

In Chapter 4, the shape development of spherical and non-spherical particles during the char conversion was studied and discussed in detail. As a result, dynamic drag coefficient models for these particles, depending on the char conversion level and particle Reynolds number, were introduced to enable the particle trajectory, and hence the particle residence time in an entrained-flow gasifier, to be predicted more accurately. However, the final carbon conversion of a char particle is decided not only by its residence time but also by its char conversion rate. Of the main processes taking place inside an entrained-flow gasifier, the char conversion is the most fundamental. Therefore, the char conversion rate is crucial to predict overall carbon conversion of the gasifier. The char conversion rate is a result of the interplay of intrinsic kinetics, char reactivity, and pore diffusion, which is governed by the particle morphology, such as the particle shape, size, density and specific surface area. The particle morphology changes continuously over the char conversion process. As mentioned in Section 2.5, the density and diameter exponent α and β are important parameters of a char conversion model. They significantly influence the reliability and accuracy of CFD simulation results of an entrained-flow gasifier. Various models of α and β can be found in the literature. However, most of them are derived from analytical 0D models, and it is not clear what model offers the best accuracy. The Random Pore Model, widely used to describe the development of specific surface area, is only valid for the chemically controlled regime (Regime I). In particular, the pore-diffusion regime (Regime II) is typical for entrained-flow gasifiers. Motivated by these points of view, this chapter studies the morphology evolution of char particles in a wide range of reaction conditions to reveal advanced sub models for the char conversion parameters.

5.1 Numerical Strategy, Discretization and Assumptions

Focusing on the laminar flow, where an axis-symmetric flow exists around a particle, the numerical strategy and boundary conditions are similar to those in Chapter 4, as shown in Figure 5.1.

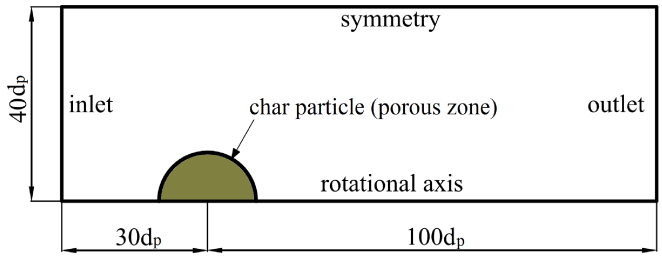

Fig. 5.1: Computational domain and boundary conditions for studying the particle morphology evolution [82]

In contrast to the study of the particle shape development, where the char particle is presented as a solid zone, the char particle is considered a porous zone, and the pore diffusion directly

modeled during the char conversion process. As shown in Figure 5.2, the computational domain was discretized into 24000 control volumes and consists of a porous zone and a fluid zone representing the char particle and the gas flow, respectively. The reaction regime dominates the conversion characteristics of a char particle. Hence, different process conditions are defined at the inlet of the computational domain. These process conditions, given in Table 5.1, are examples of conditions for a flame zone with oxygen-rich conditions (Case 1 [2]) and a post-flame zone with oxygen-poor conditions (Case 2) inside an entrained-flow gasifier, and a gasification condition without oxygen (Case 3). The higher the oxygen concentration is, the higher the gas temperature surrounding the particle, and the closer char conversion process is to Regime III. The sets of the inlet condition above allow us to observe the particle morphology evolution under a wide range of the regime condition. For simplicity, the inlet velocity is kept constant for all cases.

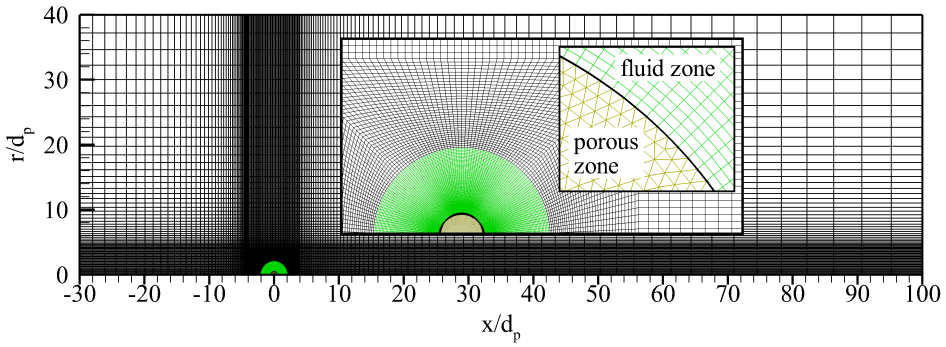

Fig. 5.2: Initial numerical mesh and zone definition for investigating the particle morphology evolution [82]

Tab. 5.1: Inlet and operation conditions for the CFD setup of the different cases

Case	T_{in}(K)	P_{op}(bar)	u_{in}(m/s)	$Y_{CO_2,in}$	$Y_{O_2,in}$	$Y_{H_2O,in}$
1	1480	30	3.192	0.223	0.187	0.221
2	1480	30	3.192	0.323	0.087	0.221
3	1950	30	3.192	0.410	0.000	0.221

To remain consistent and comparable with the model based on the effectiveness factor approach in Chapter 4, the mechanisms of the homogeneous and heterogeneous reactions in this study are similar to those presented in Section 4.1. The kinetic parameters of the chemical reactions are taken from Table 4.3. The char properties are given in Table 4.4. To obtain a wide range for the effectiveness factor, different initial diameters ranging from 50 µm to 400 µm are considered. In [23], the structural parameter Ψ is estimated as 3.0 and 4.7 for two groups of coal char, and as mentioned in [34], it is in a range of 2.2–7.7 for eight types of coal char. Thus, the structure parameter Ψ is set at 4.0 as an average value. Since the char conversion process at high temperatures is considered, the thermal annealing effect is considered for char deactivation. The loss of char reactivity is modeled as a single Arrhenius expression, taken from the work of Tremel and Spliethoff [83],

$$k_{ta} = 1 + f_{ta}(\Lambda_{max} - 1) \tag{5.1}$$

where k_{ta} is the annealing coefficient and Λ_{max} denotes the maximal reactivity ratio, which is defined as the ratio of the reactivity of a fresh char to a strongly deactivated char. The annealing function f_{ta} ($0 < f_{ta} \leq 1$) is calculated as

$$f_{ta} = \exp\left[- A_{ta} \exp\left\{ -\frac{E_{a,ta}}{R_G\, T_p} \right\} t \right] \tag{5.2}$$

where A_{ta} and $E_{a,ta}$ are the pre-exponential factor and activation energy for the thermal annealing effect, respectively, and t is the char conversion time. The thermal annealing parameters are given in Table 5.2 as an approximation of the coal char used.

Tab. 5.2: Thermal annealing parameters [83]

Max. reactivity ratio	Λ_{max}	23.4
Pre-exponentional factor	A_{ta}	2.10×10^{10}/s
Activation energy	$E_{a,ta}$	1.17×10^{8} J/kmol

In the present work, the following assumptions are made in the numerical model regarding the reacting char particle:

- The internal char structure belongs to Group III.
- The char particle is a homogeneous porous medium and initially isotropic.
- The char particle is spherical and consists of carbon only.
- No char fragmentation occurs.
- The thermal conductivity and heat capacity of the solid phase are constant.
- The solid and gas phases inside the char particle are in thermal equilibrium.
- The gas flow is laminar and the flow field is axis-symmetric.
- The particle does not participate in the radiation transport.

First, the ash-free char particle is considered as a simplified case. Then, the ash effect is studied in Section 5.4.5.

5.2 Governing Equations for a Porous Medium

Since a porous medium is applied to model a porous reacting char particle, the system of governing equations for the gas phase inside the porous medium requires several additional sources to take into account the influences of the heterogeneous processes taking place on the char particle's pore surface. A mass source is added to the continuity equation to represent the carbon mass flux released from the char particle to the gas phase. Thus, the continuity equation reads

$$\frac{\partial(\varepsilon_{cell}\,\rho_g)}{\partial t} + \nabla\cdot(\varepsilon_{cell}\,\rho_g\,\vec{u}) = M_S \tag{5.3}$$

The mass source is calculated based on the heterogeneous reaction rates, expressed as

$$M_S = \sum_{j=1}^{N_{het}} R_{C,j,cell} = \sum_{j=1}^{N_{het}} S'''_{V,cell} R_{int,j} \tag{5.4}$$

where $R_{int,j}$ is the intrinsic rate of the heterogeneous reaction j. The mass source also influences the momentum balance by introducing a momentum source to the momentum equation, expressed in the following equation.

$$\frac{\partial(\varepsilon_{cell}\,\rho_g\vec{u})}{\partial t} + \nabla\cdot(\varepsilon_{cell}\,\rho_g\vec{u}\vec{u}) = -\varepsilon_{cell}\,\nabla p + \nabla\cdot(\varepsilon_{cell}\boldsymbol{\tau}) - \left(\frac{\mu}{P_m} + \frac{C_2}{2}\rho_g|\vec{u}|\right)\vec{u} + \vec{F}_S \tag{5.5}$$

The stress tensor comprises the dynamic viscosity and is calculated as

$$\boldsymbol{\tau} = \mu\left(\left(\nabla\vec{u} + (\nabla\vec{u})^{\mathsf{T}}\right) - \frac{2}{3}\nabla\cdot\vec{u}\mathbf{I}\right) \tag{5.6}$$

P_m and C_2 denote the permeability and inertial loss coefficient of flow, respectively. To take into account momentum sink due to inertial and viscous resistance, the Ergun equation is applied for the porous medium, with the permeability and the inertial loss coefficient defined by [27] as

$$P_m = \frac{D_h^2}{150} \frac{\varepsilon_{cell}^3}{(1-\varepsilon_{cell})^2} \tag{5.7}$$

$$C_2 = \frac{3.5}{D_h} \frac{(1-\varepsilon_{cell})}{\varepsilon_{cell}^3} \tag{5.8}$$

The mean hydraulic diameter is calculated by [84]

$$D_h = \frac{6}{S'''_{V,cell}} \tag{5.9}$$

The momentum source is related to the mass source, as in the following formula.

$$\vec{F}_S = M_S \vec{u} \tag{5.10}$$

The species sources are added to the species transport equations to represent the reactant and the product species, which are consumed and produced due to the heterogeneous reactions. Hence, the species transport equation reads

$$\frac{\partial(\varepsilon_{cell}\,\rho_g\,Y_i)}{\partial t} + \nabla\cdot(\varepsilon_{cell}\,\rho_g\,\vec{u}Y_i) = \nabla\cdot\left(\varepsilon_{cell}(\rho_g\,D_{eff,i}\nabla Y_i + D_{T,i}\frac{\nabla T}{T})\right) + \varepsilon_{cell}\sum_{j=1}^{N_{hom}} R_{hom,i,j} + M_{S,i} \tag{5.11}$$

The effective diffusion coefficient of the species in the porous medium is calculated in [25].

$$D_{eff,i} = \varepsilon_{cell}^2\; D_{i,m} \tag{5.12}$$

The mass source of the species is defined as

$$M_{S,i} = \sum_{j=1}^{N_{het}} \frac{\nu_{i,j}}{|\nu_{C,j}|} \frac{M_{w,i}}{M_{w,C}} R_{C,j,cell} \tag{5.13}$$

The heat released or absorbed from the heterogeneous reactions influences the enthalpy balance of the porous medium. If thermal equilibrium is assumed to exist between the solid and gas phases, an energy equation is needed for the porous medium's energy balance. The energy source is added to the energy equation, expressed as

$$\frac{\partial(\varepsilon_{cell}\rho_g h_g + (1-\varepsilon_{cell})\rho_{sol}h_{sol})}{\partial t} + \nabla\cdot\left(\varepsilon_{cell}(\vec{u}\rho_g h_g + p)\right) = \nabla\cdot(\lambda_{eff}\nabla T - \sum_i h_i\vec{J}_i + \tau\cdot\vec{u}) + \varepsilon_{cell}\sum_{j=1}^{N_{hom}}\frac{\Delta H_j^0}{M_w}R_{hom,j} + H_S \tag{5.14}$$

with the effective thermal conductivity in the porous medium

$$\lambda_{eff} = \varepsilon_{cell}\lambda_g + (1-\varepsilon_{cell})\lambda_{sol} \tag{5.15}$$

The energy source is defined as

$$H_S = \sum_{j=1}^{N_{het}} \Delta H_{R_{het,j}} R_{C,j,cell} \tag{5.16}$$

The heat capacity of each species is based on a fourth-order polynomial expression [73], and the heat capacity of the mixture is based on the mass-weighted average of the individual heat capacities. The single species' thermal conductivities are calculated using kinetic theory, and the mole-weighted average is used for the mixture. Details can be found in [74]. The P-1 radiation model is used to examine the distribution of radiation depending on the gas temperature [75].

Due to the pore diffusion's influence on the distribution of species inside the porous char particle, the carbon consumption rate is not uniform across the porous particle, depending on the local temperature, reactant concentration, and specific surface area. The local char conversion at a given reaction time is calculated as

$$X_{c,cell}^{t+\Delta t} = X_{c,cell}^{t} + \frac{\sum_{j=1}^{N_{het}} R_{C,j,cell}^{t+\Delta t} \Delta t}{\rho_{C,0}} \tag{5.17}$$

Within a computational cell, the temperature distribution, species concentration, and specific surface area are uniform. The Random Pore Model is used to depict the development of the local specific surface [17, 52, 53].

$$S_{V,cell}''' = S_{m,0}''' \rho_{p,0} (1 - X_{c,cell}) \sqrt{1 - \Psi \ln(1 - X_{c,cell})} \tag{5.18}$$

The local char density

$$\rho_{C,cell} = (1 - \varepsilon_{cell}) \rho_{c,t} \tag{5.19}$$

is dependent on the local porosity

$$\varepsilon_{cell} = \varepsilon_{p,0} + (1 - \varepsilon_{p,0}) X_{c,cell} \tag{5.20}$$

The mean characteristics based on the volumetric integration were used to calculate the particle morphology with the following formulas.

The particle diameter is given as

$$d_p = \sqrt[3]{\frac{6 V_p}{\pi}} \tag{5.21}$$

with

$$V_p = V_{p,0} - \sum V_{cell} \,|_{X_{c,cell}=1} \tag{5.22}$$

and the carbon density of the char particle is given as

$$\rho_C = \frac{m_p}{V_p} \tag{5.23}$$

with

$$m_p = \sum m_{cell} \,|_{X_{c,cell}<1} \tag{5.24}$$

The char particle porosity is calculated as

$$\varepsilon_p = 1 - \frac{\rho_C}{\rho_{c,t}} \tag{5.25}$$

and the char specific surface area is determined as

$$S_V''' = \frac{\sum (S_{V,cell}''' V_{cell})}{V_p} \Big|_{X_{c,cell}<1} \tag{5.26}$$

with the overall char conversion

$$X_c = \frac{m_{p,0} - m_p}{m_{p,0}} \tag{5.27}$$

5.3 Validation

The utilization of the porous zone model to depict complex physical and chemical phenomena occurring in the vicinity and interior of a char particle was initially carried out and was validated against the experimental data by Beckmann et al. [18]. The validation shows that the model is capable not only of revealing the evolution of the particle morphology but also of reproducing the experimental data, and especially the carbon consumption rate. Fong et al. [19] developed and implemented the porous zone model in three dimensions to examine how structural voids inside the char particle influence the interior flow field and the carbon consumption rate. In addition, the numerical results of the steady-state CFD calculation for an isolated 263 µm particle utilizing the porous zone model and the effectiveness factor model are compared. The comparison shows that under the same boundary and operation conditions and chemical mechanisms, the deviation in the carbon consumption rates between the two models is minor: only 2.7 %. The velocity, temperature, and species distribution surrounding the char particle demonstrate a good agreement between the two models, as shown in Figure 5.3.

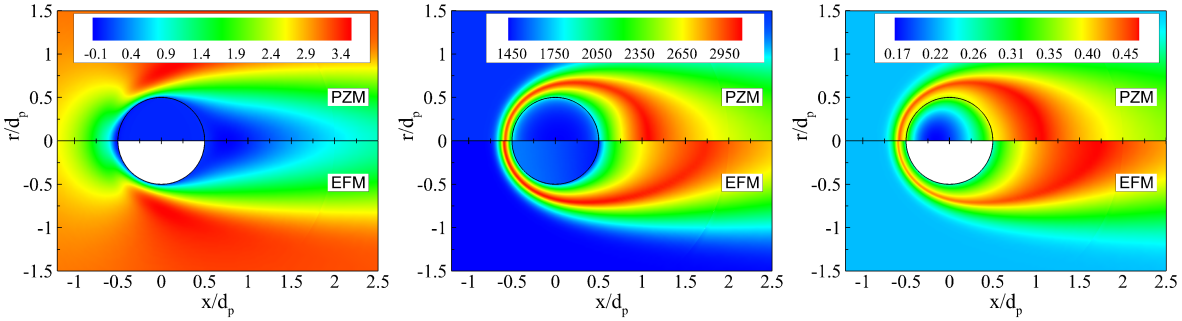

(a) velocity, m/s (b) temperature, K (c) Y_{CO_2} kg/kg

Fig. 5.3: The comparison of the porous zone model (PZM) to the effectiveness factor model (EFM) is derived from the steady state calculation of a 263 µm particle at Case 1 conditions. Kinetics of chemical reactions and char properties are given in Table 4.3 and Table 4.4, respectively

5.4 Results

5.4.1 Conversion Behavior of a Single Reacting Char Particle

In this section, the conversion behavior of single char particles is studied using the numerical model introduced in Section 5.1. The numerical results improve our knowledge about what physical and chemical phenomena take place around and inside a porous char particle and how the char particle morphology evolves during the carbon conversion process. This knowledge plays an important role in establishing a reliable sub grid model for calculating and optimizing entrained-flow gasifiers.

The conversion behavior of an isolated 200 µm char particle in oxygen-rich conditions, Case 1 in Table 5.1, was studied. Figure 5.4 shows the temperature field, distribution of carbon dioxide mass fraction, and Boudouard reaction rate corresponding to 10, 50, and 95 % of carbon conversion on average. Under these conditions, the particle diameter and particle density decrease simultaneously during the carbon conversion process. The reactant species, e.g. CO_2, diffuses towards the particle center with high-gradient distributions at a low carbon conversion level. With an increase in the conversion level, the distributions become more homogeneous over the particle volume. As a result, the heterogeneous reactions, e.g. the

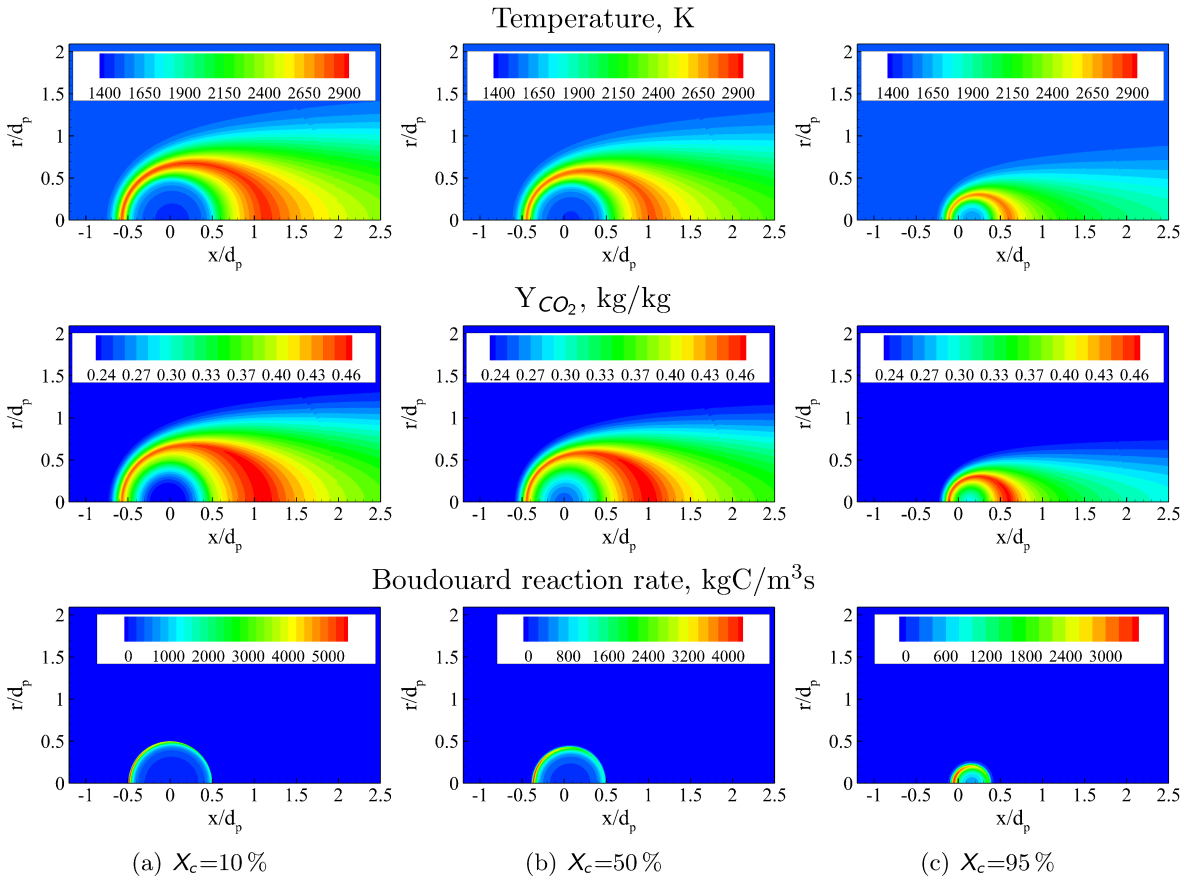

Fig. 5.4: Distribution of temperature, mass fraction of CO_2 and Boudouard reaction rate for a 200 µm char particle at different global carbon conversion levels under oxygen-rich conditions (Case 1)[82]

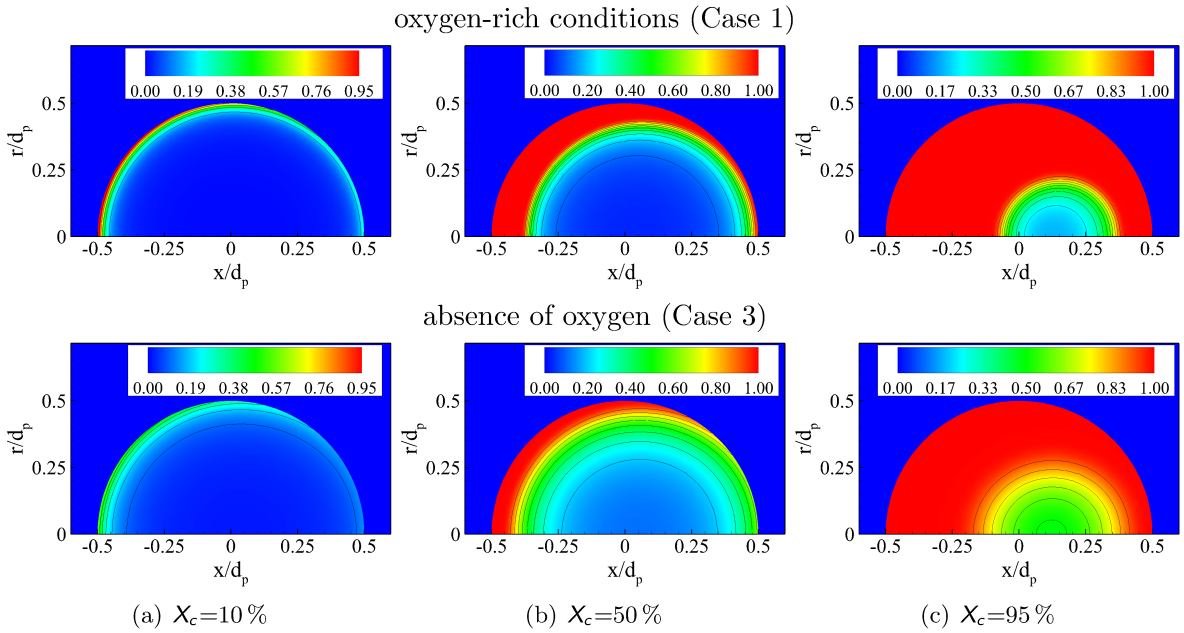

Fig. 5.5: Distribution of local carbon conversion inside a 200 µm char particle at different global conversion levels under different reaction conditions [82]

Boudouard reaction, reach the particle's center. However, the region with the highest carbon conversion rate is located inside the particle, close to the outer surface, which reflects the Random Pore Model's effect on the development of char reactivity. Since Case 2 has a lower oxygen level than Case 1, the temperature around the particle drops, which affects the particle conversion behavior. The influence of low oxygen conditions on the particle morphology evolution in comparison with high oxygen conditions will be illustrated in Section 5.4.3.

In addition, the conversion behavior of the 200 µm char particle in the absence of oxygen, Case 3 in Table 5.1, was investigated. The carbon conversion distribution across the particle is compared for Case 1 and Case 3 to demonstrate the influence of reaction conditions on the particle's morphological development, as shown in Figure 5.5. It can be seen that when the temperature of the flame sheet surrounding the char particle is high, as in Case 1, the carbon conversion distribution shows a large gradient, whereas in the absence of oxygen, the carbon conversion is distributed more uniformly over the particle volume.

5.4.2 Morphology Evolution of Single Particles During Char Conversion

This section aims to quantify the evolution of a particle's morphology and the correlations of the fundamental conversion parameters such as the density and diameter exponent, α and β, with the effectiveness factor η during the conversion process undergone by a char particle. The carbon conversion level and global characteristics of a char particle such as the diameter, density, porosity and specific surface area were determined based on the equations from Eq. (5.21) to Eq. (5.27).

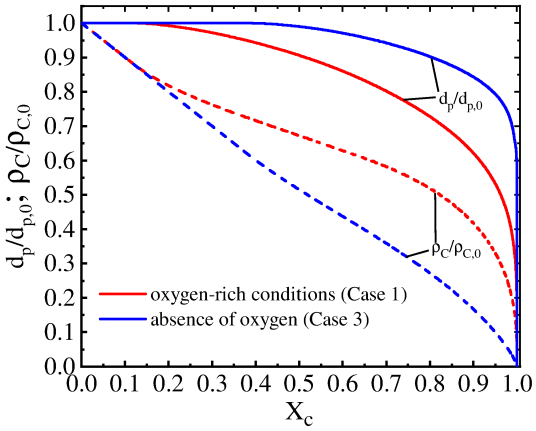

Fig. 5.6: The change in density and diameter of a 200 µm char particle during the conversion process [82]

Figure 5.6 shows the relative diameter $d_p/d_{p,0}$ and carbon density $\rho_C/\rho_{C,0}$ of the 200 µm particle studied in Section 5.4.1 as a function of the carbon conversion X_c. It is clear that both the char diameter and density decrease during the carbon conversion process. However, during the early stage of the conversion process, the particle diameter remains constant. The point at which the particle starts to shrink depends on the reaction conditions. The exponents of the particle diameter and the particle density are calculated by Eq. (5.28) and Eq. (5.29), which are derived from Eq. (2.39) and Eq. (2.40), respectively

$$\beta = \frac{\ln\left(\frac{d_p}{d_{p,0}}\right)}{1 - X_c} \tag{5.28}$$

$$\alpha = \frac{\ln\left(\frac{\rho_C}{\rho_{C,0}}\right)}{1 - X_c} \tag{5.29}$$

To obtain effectiveness factors from the transient calculations, the particle properties are extracted at different carbon conversion levels. For each carbon conversion level, a new particle model was set up, at which the particle properties are defined as uniform across the particle. For every model, steady-state calculations were carried out. The effectiveness factor is calculated directly using the definition expressed in Eq. (5.30), based on the carbon consumption rate obtained from the steady-state numerical calculation.

$$\eta = \frac{R_{eff}}{R_{max}} = \frac{\frac{\iiint_V S_V''' \sum(R_{int,j}) dV_p}{\iiint_V S_V''' dV_p}}{\frac{\iint_S \sum(R_{int,j}) dA_p}{\iint_S dA_p}} \tag{5.30}$$

Tab. 5.3: Density and diameter exponent α and β and effectiveness factor η of a 200 µm char particle vary with char conversion level X_c from 0.1 to 0.95 in different process conditions

X_c		0.1	0.2	0.3	0.4	0.5	0.6	0.7	0.8	0.9	0.95
Case 1											
	α	1	0.901	0.762	0.654	0.573	0.507	0.451	0.408	0.380	0.370
	β	0	0.033	0.079	0.115	0.142	0.164	0.183	0.197	0.207	0.210
	η	0.118	0.123	0.126	0.130	0.134	0.139	0.146	0.158	0.179	0.206
Case 3											
	α	1	1	1	0.997	0.957	0.903	0.852	0.808	0.778	0.768
	β	0	0	0	0.001	0.014	0.032	0.049	0.064	0.074	0.077
	η	0.331	0.330	0.332	0.337	0.344	0.356	0.374	0.404	0.471	0.563

As shown in Figure 5.6, the beginning of the conversion process mainly causes a decrease in the particle density, while the particle volume remains constant ($\beta \approx 0$, $\alpha \approx 1$), and at higher carbon conversion levels the particle volume starts to decrease. The results of the steady-state calculations for the density and diameter exponent α, β and effectiveness factor η are collected in Table 5.3. Based on the data shown in Table 5.3, Figure 5.7a depicts α, β and X_c as a function of the effectiveness factor η. In oxygen-rich conditions, the reaction rate limitation due to pore diffusion is more pronounced than that in oxygen-free conditions. α and β strongly depend on the carbon conversion X_c.

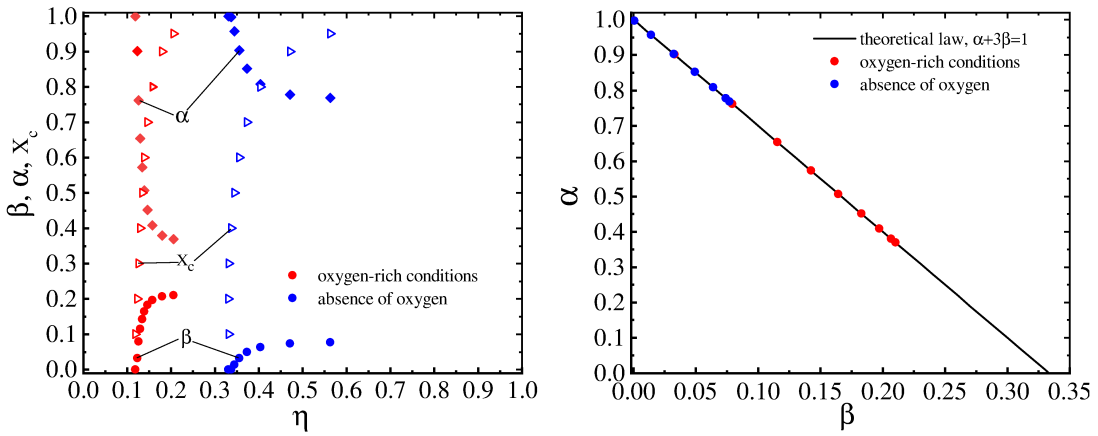

(a) the change in conversion model parameters (b) the parameter correlation and theoretical law

Fig. 5.7: The change in conversion model parameters of a 200 µm char particle with the conversion process and a comparison of the parameter correlation with theoretical law [82]

For low effectiveness factors, major carbon consumption occurs in a thin outer particle layer, resulting in a decreasing particle volume. With increasing effectiveness factors, the thickness of the layer at which the reactions occur increases, as shown in Figure 5.5. As a result, the carbon consumption in the outer layer is shifted towards higher char conversion states, resulting in smaller changes of α and β for oxygen-free conditions. α and β corresponding to each carbon conversion level were plotted in Figure 5.7b against the theoretical law $\alpha + 3\beta = 1$, confirming the validation of the current particle-resolved model.

5.4.3 Correlations for the Particle Morphology Evolution

As described above, the mode of char conversion, with either the reduction in the diameter or density dominating, depends on both the state of the conversion and the actual effectiveness factor. This section deals with the analysis of the particle data to reveal functional correlations for α and β. In order to analyze the evolution of particle morphology in a typical gasifier, the different conditions present along the particle trajectory have to be considered. Therefore, for the three operating conditions described in Table 5.1, particles with uniform char properties (Table 4.4) and different initial diameters ranging from 50 µm to 400 µm are studied using transient calculations. As shown in Section 5.4.2, steady-state calculations are carried out for all 13 transient calculations in order to estimate the effectiveness factor. To this end, 10 fixed levels of X_c between 10 % and 95 % are considered, resulting in an additional 130 steady-state calculations.

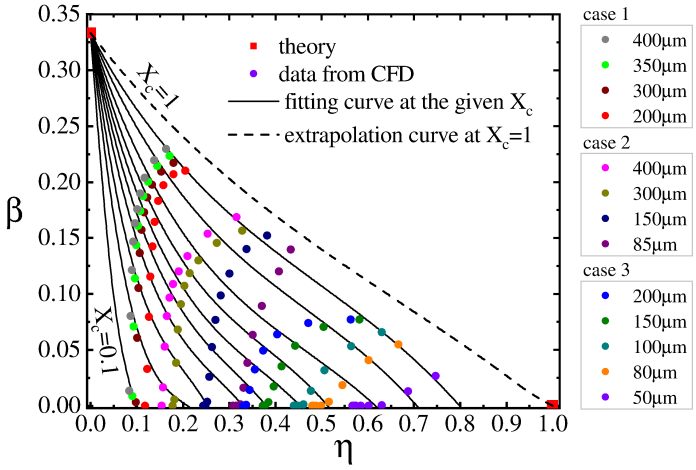

Fig. 5.8: The dependence of diameter exponent β on the effectiveness factor η and char conversion level X_c [82]

The results of the steady-state calculations for the diameter exponent β and effectiveness factor η are collected in Table 5.4. The diameter exponent β is plotted against η for all 13 particles as shown in Figure 5.8. With the effectiveness factor in the range of 0.08 to 0.75, the calculations cover almost the entire operating regime which applies to char particles in a pressurized entrained-flow reactor [36]. For all particles, as the degree of conversion X_c increases, both the effectiveness factor η and the diameter exponent β increase. For small particles in particular, β is zero until the conversion X_c reaches a certain limit. Two theoretical points are added to the graph: $\eta = 1$, $\beta = 0$ (Regime I) and $\eta = 0$, $\beta = 1/3$ (Regime III) for all carbon conversion levels. The correlation for β is shown in Figure 5.9. It can be seen that in a large area of the η-X_c plane, β is zero. This area is approximately separated by the diagonal between the points $X_c - \eta = (0, 0)$ and $X_c - \eta = (1, 1)$. From this, it can be roughly estimated that if the carbon conversion value is smaller than the actual effectiveness factor, there will be only a minor decrease in particle diameter during the conversion process.

Tab. 5.4: Diameter exponent β, RPM factor γ and effectiveness factor η vary with char conversion level X_c from 0.1 to 0.95 in different process conditions

d_p(µm)	X_c	0.1	0.2	0.3	0.4	0.5	0.6	0.7	0.8	0.9	0.95
Case 1											
400	β	0.013	0.080	0.121	0.147	0.163	0.176	0.190	0.204	0.220	0.229
	γ	0.939	0.899	0.889	0.902	0.938	1.011	1.158	1.466	2.348	3.913
	η	0.084	0.087	0.089	0.092	0.096	0.101	0.107	0.117	0.138	0.163
350	β	0.008	0.071	0.114	0.143	0.161	0.174	0.187	0.200	0.214	0.223
	γ	0.941	0.898	0.888	0.904	0.941	1.012	1.155	1.447	2.279	3.751
	η	0.090	0.093	0.096	0.099	0.103	0.108	0.114	0.124	0.145	0.171
300	β	0.003	0.061	0.105	0.136	0.157	0.173	0.186	0.198	0.209	0.217
	γ	0.943	0.898	0.887	0.903	0.943	1.019	1.158	1.438	2.209	3.565
	η	0.098	0.101	0.104	0.107	0.111	0.116	0.123	0.133	0.153	0.179
200	β	0	0.033	0.079	0.115	0.142	0.164	0.183	0.197	0.207	0.210
	γ	0.952	0.897	0.881	0.894	0.936	1.018	1.169	1.457	2.177	3.335
	η	0.118	0.123	0.126	0.130	0.134	0.139	0.146	0.158	0.179	0.206
Case 2											
400	β	0	0.016	0.053	0.080	0.097	0.109	0.120	0.134	0.154	0.169
	γ	0.959	0.902	0.881	0.882	0.898	0.938	1.021	1.214	1.786	2.768
	η	0.154	0.157	0.161	0.165	0.171	0.179	0.191	0.210	0.253	0.316
300	β	0	0.005	0.038	0.068	0.091	0.107	0.119	0.130	0.145	0.157
	γ	0.965	0.908	0.881	0.881	0.904	0.949	1.028	1.197	1.683	2.509
	η	0.178	0.182	0.185	0.189	0.195	0.203	0.214	0.233	0.273	0.328
150	β	0	0	0.003	0.026	0.052	0.076	0.098	0.118	0.140	0.152
	γ	0.978	0.935	0.889	0.871	0.883	0.925	1.012	1.187	1.666	2.423
	η	0.244	0.248	0.252	0.257	0.263	0.271	0.282	0.301	0.337	0.382
85	β	0	0	0	0.001	0.016	0.038	0.063	0.089	0.120	0.139
	γ	0.986	0.956	0.919	0.879	0.865	0.884	0.948	1.098	1.543	2.278
	η	0.309	0.315	0.320	0.325	0.331	0.339	0.351	0.371	0.408	0.433
Case 3											
200	β	0	0	0	0.001	0.014	0.032	0.049	0.064	0.074	0.077
	γ	0.985	0.955	0.918	0.879	0.865	0.879	0.921	1.008	1.199	1.441
	η	0.331	0.330	0.332	0.337	0.344	0.356	0.374	0.404	0.471	0.563
150	β	0	0	0	0	0.003	0.017	0.035	0.053	0.070	0.077
	γ	0.989	0.965	0.934	0.900	0.869	0.869	0.902	0.987	1.191	1.451
	η	0.374	0.373	0.374	0.378	0.385	0.396	0.413	0.443	0.504	0.582
100	β	0	0	0	0	0	0.001	0.013	0.032	0.053	0.066
	γ	0.993	0.976	0.955	0.929	0.899	0.870	0.875	0.933	1.107	1.356
	η	0.442	0.439	0.440	0.443	0.449	0.461	0.477	0.506	0.564	0.631
80	β	0	0	0	0	0	0	0.004	0.018	0.041	0.055
	γ	0.994	0.981	0.964	0.943	0.917	0.888	0.868	0.900	1.044	1.261
	η	0.482	0.479	0.480	0.482	0.488	0.499	0.516	0.545	0.602	0.667
50	β	0	0	0	0	0	0	0	0	0.013	0.027
	γ	0.997	0.989	0.979	0.966	0.950	0.929	0.905	0.876	0.920	1.048
	η	0.571	0.568	0.567	0.570	0.575	0.585	0.602	0.631	0.687	0.747

As β is considered a function of the effectiveness factor and char conversion level, it leads to the statement that the correlation for β should be independent of the fuel parameters and operating conditions chosen to calculate the char conversion process. To support that statement, the yellow points in Figure 5.9 plot the evolution of β during the conversion process for a 300 µm char particle with the same inlet conditions as in Case 2 but differing in terms of the pore structure parameter and pressure operations condition, e.g. Ψ=8.0 and P_{op}=20 bar. The points fitting with the surface nearly precisely are concrete evidence which reconfirms this statement.

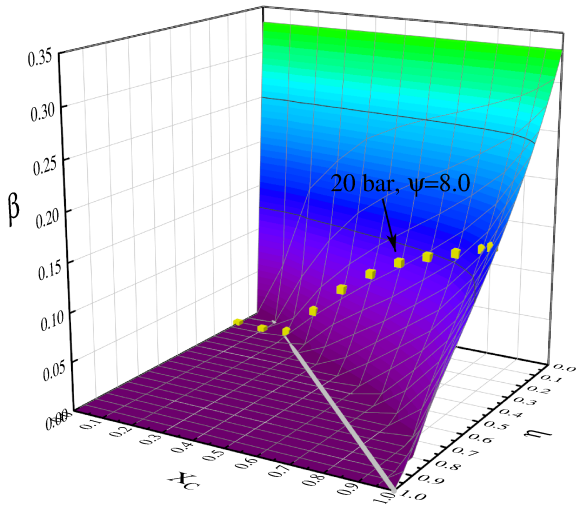

Fig. 5.9: Three-dimensional surface representing the function of the diameter exponent, $\beta(\eta, X_c)$ [82]

To apply the results in sub models for CFD reactor calculations, β is estimated as a polynomial fitting function based on the carbon conversion and the efficiency factor in the form:

$$\begin{cases} \beta = z \;\; if \;\; z \geq 0 \\ \beta = 0 \;\; if \;\; z < 0 \end{cases} \tag{5.31}$$

with

$$\begin{aligned} z = {} & p_{00} + p_{10}X_c + p_{01}\eta + p_{11}X_c\eta + p_{02}\eta^2 + p_{12}X_c\eta^2 \\ & + p_{03}\eta^3 + p_{13}X_c\eta^3 + p_{04}\eta^4 + p_{14}X_c\eta^4 + p_{05}\eta^5 \end{aligned} \tag{5.32}$$

and $p_{00} = 0.3319$, $p_{10} = 0.001608$, $p_{01} = -4.049$, $p_{11} = 3.509$, $p_{02} = 14.640$, $p_{12} = -15.480$, $p_{03} = -22.840$, $p_{13} = 27.430$, $p_{04} = 8.440$, $p_{14} = -14.510$, $p_{05} = 2.531$ ($R^2 = 0.988$).

5.4.4 Modified Random Pore Model

In Regime I, the temperature, species concentrations and reaction rates are homogeneous across the whole particle. Therefore, the Random Pore Model (RPM) can be used to describe the development of the specific surface area by applying the equation

$$\frac{S'''_V}{S'''_{V,0}} = (1 - X_c)\sqrt{1 - \Psi \ln(1 - X_c)} \tag{5.33}$$

Typically, Regime II is the main regime for reacting particles at entrained-flow gasification conditions. In Regime II, both the intrinsic chemical reactions and pore diffusion affect the heterogeneous reaction rate. For a 200 µm particle, Figure 5.10a shows the surface evolution

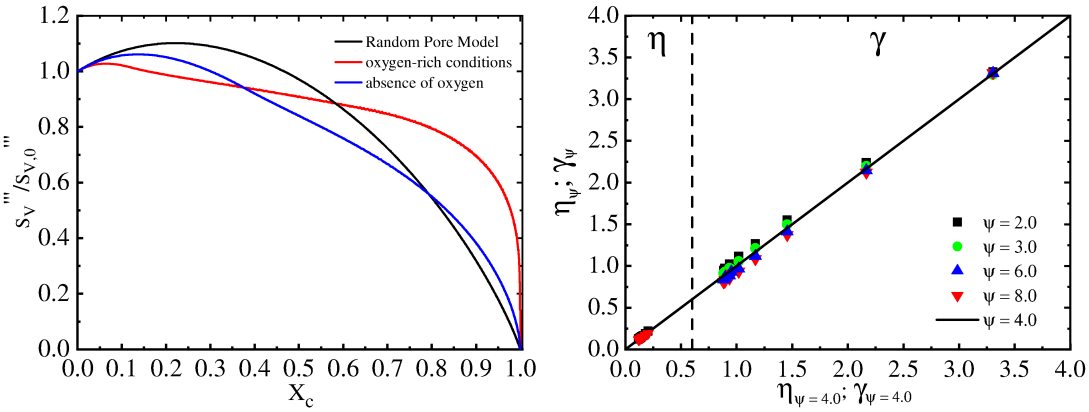

(a) specific surface area evolution (b) effect of Ψ on η and γ

Fig. 5.10: The evolution of specific surface area of a 200 µm char particle under different reaction conditions compared to the RPM, and the effect of structure parameter Ψ on the factor γ and effectiveness factor η [82]

for oxygen-rich conditions (Case 1) and oxygen-free conditions (Case 3), comparing them with results based on the RPM with the structure parameter Ψ=4.0.

It can be seen that the surface evolution depicted by the RPM deviates from the numerical calculation results, especially in oxygen-rich conditions. Since the faster reaction rate of the combustion reaction shifts the conditions closer towards Regime III, a greater deviation from the RPM is expected for this case. To increase the accuracy of the calculated specific surface, an adjustment of the RPM is necessary in the form

$$\frac{S'''_V}{S'''_{V,0}} = \gamma\,(1 - X_c)\sqrt{1 - \Psi \ln(1 - X_c)} \tag{5.34}$$

The factor γ, the ratio of the specific surface area obtained from CFD calculation to that calculated directly by the RPM, depends on the pore structure parameter, char conversion level and process conditions represented by the effectiveness factor. To estimate the effect of the pore structure parameter, several values of Ψ are used to calculate γ for a 200 µm particle under oxygen-rich conditions. A comparison of γ corresponding to different char conversion levels for different values of Ψ is shown on the right in Figure 5.10b. It can be seen that γ for different values of Ψ is narrowly distributed around γ for Ψ=4.0 with a maximal difference of 9.42 % for Ψ=2.0 at X_c=60 %. The effectiveness factor at different char conversion levels for Ψ=2.0 and 8.0 is also plotted against that for Ψ=4.0, as shown on the left in Figure 5.10b. The impact of Ψ on the effectiveness factor η is minor with a maximal deviation of 6.0 % for Ψ=8.0 at X_c=95 %. The comparison leads to the conclusion that γ estimated using Ψ=4.0 can be used to approximately modify the RPM for different structure parameters ranging from 2.0 to 8.0. Based on the relevant data obtained from the numerical calculations of 13 particles in Section 5.4.3, the correction factor γ was estimated as

$$\begin{aligned}\gamma = {} & p_{00} + p_{10}X_c + p_{01}\eta + p_{20}X_c^2 + p_{11}X_c\eta + p_{02}\eta^2 + p_{30}X_c^3 \\ & + p_{21}X_c^2\eta + p_{12}X_c\eta^2 + p_{03}\eta^3 + p_{40}X_c^4 + p_{31}X_c^3\eta \\ & + p_{22}X_c^2\eta^2 + p_{13}X_c\eta^3 + p_{04}\eta^4 + p_{50}X_c^5 + p_{41}X_c^4\eta \\ & + p_{32}X_c^3\eta^2 + p_{23}X_c^2\eta^3 + p_{14}X_c\eta^4 + p_{05}\eta^5\end{aligned} \tag{5.35}$$

and $p_{00} = 0.9843$, $p_{10} = -0.7452$, $p_{01} = 0.1949$, $p_{20} = 2.2460$, $p_{11} = -1.4130$, $p_{02} = -0.4842$, $p_{30} = 1.8660$, $p_{21} = -5.1430$, $p_{12} = 7.6430$, $p_{03} = 0.9765$, $p_{40} = -17.0800$, $p_{31} = 25.6700$, $p_{22} = -16.5600$, $p_{13} = -2.5060$, $p_{04} = -1.6440$, $p_{50} = 19.5300$, $p_{41} = -30.6300$, $p_{32} = 12.9200$,

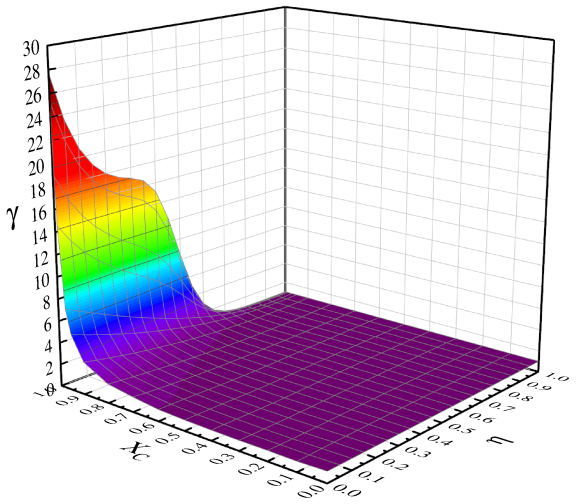

Fig. 5.11: Surface plot representing the function of the RPM factor, $\gamma(\eta, X_c)$ [82]

$p_{23} = 5.8610$, $p_{14} = -1.5730$, $p_{05} = 0.9802$ ($R^2 = 0.987$). This is illustrated in Figure 5.11. It should be noted that in Regime I the factor γ equals unity for all stages of carbon conversion. It can be seen that the correction factor γ is approximately unity over a wide range of parameters. Only at a high carbon conversion and for low effectiveness factors does γ increase up to 28.

5.4.5 Ash Influence on Char Conversion Process

In particular, char particles contain a degree of inorganic material. Some authors have indicated that the char oxidation and gasification rate could be enhanced by this inorganic material due to catalysis, especially at low temperatures. However, the inorganic material can form a porous ash layer covering the char particle [32]. At high temperatures, the ash can block micro-pore char structures when it is melted [23]. Generally, the ash's influence on the char conversion process is complicated. In particular, it is not certain whether the ash layer remains or is removed due to high shear stresses of the gas flow.

This section focuses on diffusion limitations from the gas phase to the reacting surface due to ash layering. The question is: How does the ash layer affect the total carbon conversion and the conversion parameters such as α, β, and γ? To answer that question, the CFD model introduced in Section 5.2 was modified to model the ash layer directly. For this, computational cells whose carbon content is consumed completely now become inert cells with a constant porosity. A 200 µm char particle with an ash layer porosity ε_a ranging from 0.35 to 0.9 was investigated for oxygen-rich conditions (compare Case 1, Table 5.1). This configuration was selected since it shows the maximum impact of the ash layer's diffusion limitation.

In cases where ε_a is larger than $\varepsilon_{p,0}$, the porosity of cells in the porous zone is modeled by their linear dependence on the carbon conversion level, as in the following equation

$$\varepsilon_{cell} = \varepsilon_{p,0} + (\varepsilon_a - \varepsilon_{p,0}) X_{c,cell} \tag{5.36}$$

In cases of softened ash where ε_{ash} is smaller than $\varepsilon_{p,0}$, the porosity of the porous zone's cells is calculated using the equation

$$\begin{array}{lcll} \varepsilon_{cell} & = & \varepsilon_{p,0} + (\frac{1+\varepsilon_{p,0}}{2} - \varepsilon_{p,0}) X_{c,cell} & \text{if } X_{C,cell} < 1 \\ \varepsilon_{cell} & = & \varepsilon_a & \text{if } X_{c,cell} = 1 \end{array} \tag{5.37}$$

The permeability P_m and the inertial loss coefficient C_2 of the ash layer are calculated by Eq. (5.7) and Eq. (5.8), respectively, with $S'''_{V,a}$=2.17 m^2/cm^3 [85]. The reaction kinetics and thermal annealing parameters and the particle's initial properties are kept the same as in the previous sections. Figure 5.12 shows the carbon conversion level X_c of the 200 µm ash char

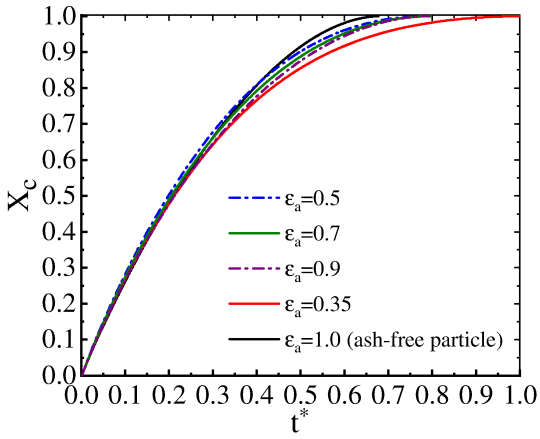

Fig. 5.12: Conversion process undergone by a 200 µm ash char particle with different levels of ash layer porosity. Oxygen-rich conditions, Case 1 in Table 5.1 [82]

particle as a function of the non-dimensional reaction time $t^* = t_r/t_{r,max}$, with the overall conversion time $t_{r,max} = max(t_r)$=149.3 ms. The ash layer prevents reactant species diffusing from the outer particle surface to the reacted core but increases the effective heat conductivity of the particle. It can be seen that below 50 % carbon conversion on average, a minor deviation between the carbon conversion profiles is observed for all the porosity values. The deviation in the carbon conversion between the ash-free and ash char particles is observed at carbon conversion levels higher than 50 % due to the increase in the ash layer's thickness over the conversion process. However, the deviation is small in all cases (3.6 % in maximum), except for the ash layer's porosity of 0.35 (6.5 % in maximum). The conclusion can be drawn that the ash layer's thickness plays a more important role than its porosity in inhibiting carbon conversion. Typically, entrained-flow gasifiers are operated in temperature conditions above the ash melting temperature. In such operation conditions, the thickness of the ash layer significantly decreases, and it becomes dynamic, which enables its rapid removal from the particle surface due the Stefan flow. Therefore, the ash layer's effect on the carbon conversion rate can be ignored in such cases, as also mentioned in [86].

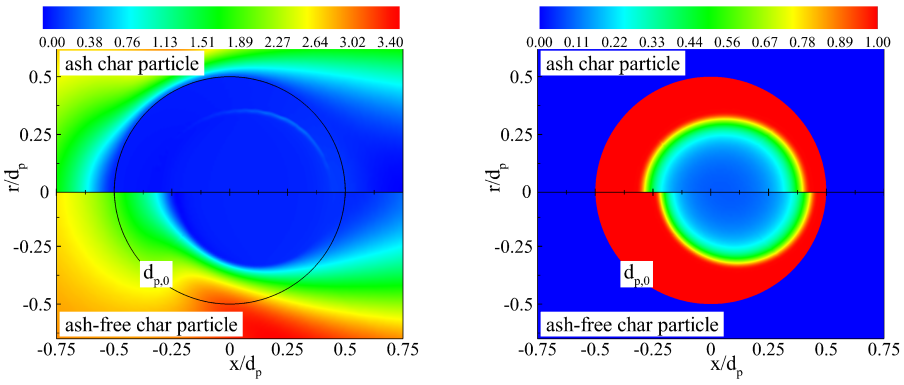

(a) velocity, m/s, (b) carbon conversion distribution

Fig. 5.13: The effect of the ash layer on intraparticle phenomena in the case of a 200 µm char particle. ε_a=0.35, X_c=80 %, oxygen-rich conditions, Case 1 in Table 5.1 [82]

In addition, Figure 5.13 compares the velocity and carbon conversion distribution for the ash-free and the ash-rich particle (ε_a=0.35) at X_c=80 %. It can be seen that the gas flow slightly penetrates the ash char particle. The reacted core's morphology is not significantly affected by the gas flow, since the carbon conversion distributions are similar for both particles. The similar distributions of the carbon conversion indicate that the interplay of the pore diffusion and chemical reaction rate for the two particles' heterogeneous reaction zone is analogous. Hence, it is reasonable to assume that the effectiveness factors are comparable.

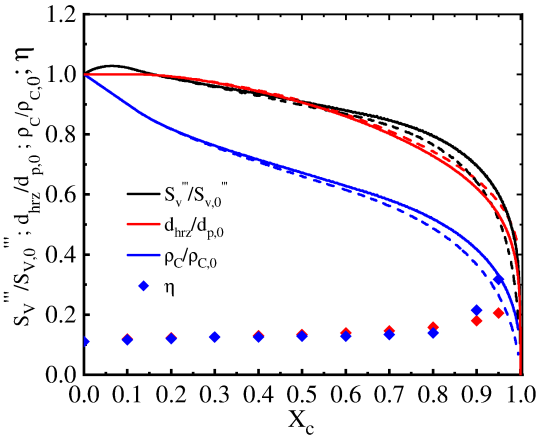

Fig. 5.14: Evolution of the heterogeneous reaction zone of a 200 µm ash-rich particle with ε_a=0.35 (dashed lines and blue points) compared to an ash-free particle (solid lines and red points) for Case 1 in Table 5.1 [82]

Correspondingly, Figure 5.14 compares the effectiveness factor η and the evolution of the reaction zone morphology for an ash-free and ash-rich particle, i.e. the relative values for the diameter of the heterogeneous reaction zone $d_{hrz}/d_{p,0}$, carbon density $\rho_C/\rho_{C,0}$ and specific surface area $S'''_V/S'''_{V,0}$ are analyzed, and exhibit only a slight deviation, except for the high carbon conversion levels; e.g. at X_c=80 % the deviation of the effectiveness factor is 11.78 %, due to a significant increase in the ash layer's thickness, which should be significantly reduced at low porosity values for a softened ash layer and moderate ash content. The comparison leads to the conclusion that the resulting correlations of conversion parameters α, β, and γ for ash-free char particles can be used to approximately describe the evolution of the reaction zone morphology of ash-containing char particles.

5.5 Discussion

The developed correlations depend on the char conversion level X_c and effectiveness factor η. A wide range of effectiveness factors and char conversion levels were considered to cover the different operation conditions applying to an entrained-flow reactor. The effectiveness factors considered in this work are also valid for processes at different operating pressures, e.g., combustion in atmospheric conditions. For that reason, the findings in this work can be used for different types of entrained-flow reactors and various operating conditions.

Typically, in experimental work, averaged values for the density and diameter are measured at the reactor outlet, where a large number of particles are found. Additionally, the process conditions in the reactor can only be considered averaged values. As a result, the diameter exponent β is overestimated by measurement, but the general trends are comparable. As mentioned in [36], the correlation between β and α from the experiment does not obey the theoretical equation $\alpha + 3\beta = 1$. That can be explained by the influence of particle fragmentation and ash layering.

5.6 Conclusion

The present work investigates the evolution of particle morphology during the char conversion process. The conversion of an isolated char particle was studied under different conditions, corresponding to a wide range of operating conditions and effectiveness factors. The CFD data were analyzed to derive new correlations for describing the particle's morphology and reactivity. From the results of the present work, it can be concluded that:

1. An asymmetric boundary layer in combination with pore diffusion limitation causes inhomogeneous and non-symmetric distributions of the temperature and species, as well as heterogeneous reactions crossing the char particle.
2. The evolution of the char particle's morphology primarily depends on the process conditions and carbon conversion level.
3. A simultaneous change in the particle's density and diameter is observed for a wide range of effectiveness factors.
4. New correlations for α and β have been derived depending on the effectiveness factor and carbon conversion level.
5. The Random Pore Model should be corrected using a factor γ.
6. The ash layering particle has a minor effect on the conversion parameters.

6 Char Conversion Model Applied for CFD Modeling of an Entrained-Flow Gasifier

Based on particle-resolved models, the evolution of the particle morphology during the char conversion process was investigated in Chapter 4 and 5. As a result, the sub models related to the drag coefficient and the fundamental parameters of a char conversion model emerged from analyzing the simulation data of the particle-resolved models. In this chapter, a detailed comprehensive particle sub model describing the char conversion process is developed. The developed particle sub model accompanied with the sub models describing the evolution of the particle morphology is applied for the CFD simulation of an entrained-flow gasifier. The reliability of the particle sub model is validated by experimental data. The validation shows a good agreement between the CFD simulation results and the experimental data. The influences of the particle shape development, other particle models and ash inhibition on the overall carbon conversion of the entrained-flow gasifier are studied and discussed in detail.

6.1 Char Conversion Model

As shown in Figure 6.1, the gas-particle reaction system consists of a reacting core surrounded by an inert ash layer and a film-gas boundary layer. The particle sub model illustrated in Figure 6.1 can be considered as a hybrid model combining the Progressive Conversion Model, Shrinking Core Model and Shrinking Particle Model [22], and is named the Hybrid Particle Model.

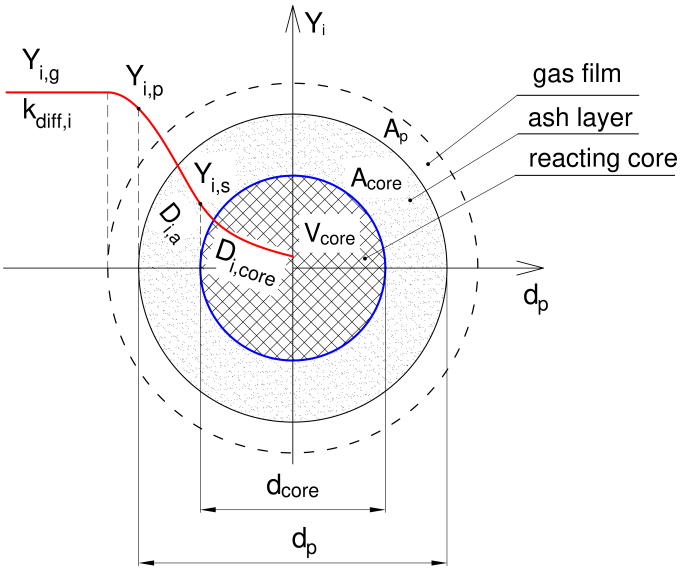

Fig. 6.1: Hybrid Particle Model of a gas-char particle reaction system

The processes of the gas-particle reaction occurring in a succession of steps can be described briefly as follows: (i) diffusion of gaseous reactant through the gas film to the outer particle surface; (ii) diffusion of the reactant through the ash layer to the boundary surface of the

reacting core; (iii) diffusion of the reactant accompanied by the heterogeneous reactions towards the center of the reacting core; (iv) diffusion of gaseous products from the reacting core towards the outer particle surface; (v) diffusion of the products through the gas film back into the main body of the gas phase. As reactant species constantly enter and react in all parts of the reacting core, usually with different reaction rates, the reacting core's morphology continuously changes during the char conversion process. As concluded in Chapter 5, the ash layer has only a minor influence on the reacting core's morphology evolution and the advanced conversion parameters, such as the density exponent α, diameter exponent β and RPM factor γ can be used to describe the morphology evolution of the reacting core. When the carbon content of the char particle is completely consumed, the char particle turns into an inert ash particle with a constant diameter and density.

Here, heterogeneous reactions are examined as follows

$$\mathrm{C} + \mathrm{CO_2} \longrightarrow 2\,\mathrm{CO} \tag{R7}$$

$$\mathrm{C} + \mathrm{H_2O} \longrightarrow \mathrm{CO} + \mathrm{H_2} \tag{R8}$$

$$\mathrm{C} + 0.5\,\mathrm{O_2} \longrightarrow \mathrm{CO} \tag{R9}$$

As the heterogeneous methanation reaction ($\mathrm{C} + 2\,\mathrm{H_2} \rightarrow \mathrm{CH_4}$) can also occur but is very slow rate and only contributes slightly to the char conversion process [1, 87], it can be neglected in the char conversion mechanisms [25, 37, 57, 88, 89]. The concept of the effectiveness factor based on the Thiele modulus is applied to calculate species consumption rates due to heterogeneous reactions [35]. The loss of char reactivity due to the thermal annealing effect is taken into account for the reduction in the species consumption rates. The consumption rate $R_{het,j}$ for the species i due to the heterogeneous reaction j, and the total char consumption rate R_c are expressed as the following:

$$R_{het,j} = \eta_j \, \frac{|\nu_{i,j}| M_{w,i}}{|\nu_{C,j}| M_{w,C}} \, k_{ta} \, k_{d,j\infty} \exp\left\{ -\frac{E_{aj}}{R_G \, T_p} \right\} p_{i,s}^{n_j} \tag{6.1}$$

$$R_c = \sum_{j=1}^{N_{het}} \frac{|\nu_{C,j}| M_{w,C}}{|\nu_{i,j}| M_{w,i}} R_{het,j} \tag{6.2}$$

$$k_{d,j\infty} = \frac{k_{j\infty}}{\Lambda_{max}} \tag{6.3}$$

$$\eta_j = \frac{1}{\Phi_j} \Big(\frac{1}{\tanh(\,3\Phi_j)} - \frac{1}{3\Phi_j} \Big) \tag{6.4}$$

$$\Phi_j = \frac{V_{core}}{A_{core}} \sqrt{ \frac{n_j + 1}{2} \frac{|\nu_{i,j}| \; S_V''' \, R_G \, T_p \, k_{ta} \, k_{d,j\infty} \exp\left\{ -\frac{E_{aj}}{R_G \, T_p} \right\} p_{i,s}^{n_j - 1}}{M_{w,C} \, D_{i,core}} } \tag{6.5}$$

where η_j is the effectiveness factor, $\nu_{i,j}$ is the stoichiometric coefficient, $M_{w,i}$ is the molar weight of species i, k_{ta} is the annealing coefficient, calculated by Eq. (5.1); $k_{d,j\infty}$ denotes the deactivated pre-exponential factor, Λ_{max} is the maximal reactivity ratio, Table 5.2; $k_{j\infty}$ and E_{aj} are the fresh pre-exponential factor [83] and the activation energy for the reaction j, $p_{i,s}$ is the partial pressure of the species i on the surface of the reacting core, n_j is the reaction order, Φ_j is the Thiele modulus of the reaction j, S_V''' is the volume-specific surface area of the reacted core, V_{core} and S_{core} are the volume and outer surface area of the reacting core, respectively, and $D_{i,core}$ denotes the effective diffusion coefficient of the species i in the reacting core. The correlation between the partial pressure $p_{i,s}$ and the mass fraction $Y_{i,s}$ is expressed as [4].

$$p_{i,s} = \frac{R_G \, \bar{\rho}_g \; T_p \; Y_{i,s}}{M_{w,i}} \tag{6.6}$$

with the average gas density $\bar{\rho}_g$ is calculated as

$$\bar{\rho}_g = 0.5(1 + \frac{T_g}{T_p})\rho_g \tag{6.7}$$

where ρ_g and T_g are the gas density and gas temperature, respectively. The key variable, which has to be determined, is the mass fraction $Y_{i,s}$ at the boundary surface of the reacting core. As the pseudo-steady-state situation of the gas-particle reaction system is achieved instantaneously, the mass of the reactant species diffusing through the gas film is equal to that diffusing through the ash layer, and also equal to the mass of the species consumed by the heterogeneous reactions taking place in the volume of the reacting core. As a result, the equation of mass balance for the species i is expressed as

$$\begin{aligned} &k_{diff,i}\,\bar{\rho}_g(Y_{i,g} - Y_{i,s}) - \left[\frac{k_{diff,i}}{D_{i,a}}\frac{d_{core}}{2}\Big(1 - \frac{d_{core}}{d_p}\Big) + \right. \\ &\left.\Big(\frac{d_{core}}{d_p}\Big)^2\right]\frac{V_{core}}{A_{core}}S_V'''\,\eta_j\frac{|\nu_{i,j}|M_{w,i}}{|\nu_{C,j}|M_{w,C}}\,k_{ta}\,k_{d,j\infty}\exp\left\{-\frac{E_{aj}}{R_G\,T_p}\right\}\Big(\frac{R_G\,\bar{\rho}_g\,T_p\;Y_{i,s}}{M_{w,i}}\Big)^{n_j} = 0 \end{aligned} \tag{6.8}$$

where $Y_{i,g}$ stands for the mass fraction of species i in gas phase. $D_{i,a}$ denotes the effective diffusion coefficient of the species i through the ash layer, $k_{diff,i}$ is the diffusion coefficient rate of the species i through the gas film, and d_{core} is the reacting core's diameter (volume-equivalent to a spherical particle). When the Hybrid Particle Model does not include the ash layer, the equation of the mass flux balance of the species i is expressed as

$$k_{diff,i}\,\bar{\rho}_g(Y_{i,g} - Y_{i,s}) - \frac{V_{core}}{A_{core}}S_V'''\,\eta_j\frac{|\nu_{i,j}|M_{w,i}}{|\nu_{C,j}|M_{w,C}}\,k_{ta}\,k_{d,j\infty}\exp\left\{-\frac{E_{aj}}{R_G\,T_p}\right\}\Big(\frac{R_G\,\bar{\rho}_g\,T_p\;Y_{i,s}}{M_{w,i}}\Big)^{n_j} = 0 \tag{6.9}$$

The diameter d_{core} and carbon density ρ_C of the reacting core are calculated as the following formulas [36, 37, 89]

$$\frac{d_{core}}{d_{core,0}} = \Big(1 - X_c\Big)^{\beta} \tag{6.10}$$

$$\frac{\rho_C}{\rho_{C,0}} = \Big(1 - X_c\Big)^{\alpha} \tag{6.11}$$

where $d_{core,0}$ and $\rho_{C,0}$ are the initial diameter and carbon density of the char particle

$$d_{core,0} = C_{sw}\,d_{p,0} \tag{6.12}$$

$$\rho_{C,0} = \frac{6(1 - f_{vap})(1 - f_{vol})m_{p,0} - m_{a,0}}{\pi d_{core,0}^3} \tag{6.13}$$

The diameter exponent β, a dependent function of the effective factor η and the char conversion level X_c, is taken from Eq. (5.32) in Chapter 5. The density exponent α is calculated based on the theoretical law, $3\beta + \alpha = 1$. The char conversion level X_c and the effectiveness factor for the carbon element η are calculated as

$$X_c = \frac{(1 - f_{vap})(1 - f_{vol})m_{p,0} - m_p}{(1 - f_{vap})(1 - f_{vol})m_{p,0} - m_{a,0}} \tag{6.14}$$

$$\eta = \frac{\sum_{j=1}^{N_{het}}\frac{M_{w,C}|\nu_{C,j}|}{M_{w,i}|\nu_{i,j}|}R_{het,j}}{\sum_{j=1}^{N_{het}}k_{ta}\,k_{d,j\infty}\exp\left\{-\frac{E_{aj}}{R_G\,T_p}\right\}p_{i,s}^{n_j}} \tag{6.15}$$

where $m_{p,0}$ is the initial mass of the coal particle, m_p is the mass of the char particle, and $m_{a,0}$ is the total mass of the ash material. Since the initial ash density $\rho_{a,0}$ is assumed to be kept constant in the reacting core during the char conversion process, the true density of the reacting core $\rho_{core,t}$ is calculated based on its remaining carbon mass fraction χ.

$$\rho_{core,t} = \frac{\rho_{a,t}\,\rho_{C,t}}{(1-\chi)\rho_{C,t} + \chi\rho_{a,t}} \tag{6.16}$$

$$\chi = \frac{\rho_C}{\rho_{core}} \tag{6.17}$$

$$\rho_{core} = \rho_C + \rho_{a,0} \tag{6.18}$$

$$\rho_{a,0} = \frac{6m_{a,0}}{\pi d_{core,0}^3} \tag{6.19}$$

where $\rho_{a,t}$ is the true ash density, $\rho_{C,t}$ denotes the true carbon density, and ρ_{core} is the density of the reacting core. The porosity of the reacting core ε_{core} is determined as

$$\varepsilon_{core} = 1 - \frac{\rho_{core}}{\rho_{core,t}} \tag{6.20}$$

The effective diffusion coefficient of the species i in the ash layer $D_{i,a}$, and in the reacting core $D_{i,core}$ are related to the porosity of the ash layer ε_a and the porosity of the reacting core ε_{core} as in the following equations

$$D_{i,a} = \varepsilon_a^2\, D_{i,m} \tag{6.21}$$

$$D_{i,core} = \varepsilon_{core}^2\, D_{i,m} \tag{6.22}$$

where $D_{i,m}$ is the diffusion coefficient of species i in the gas phase. The porosity of the ash layer ε_a is from 0.16 to 0.5, depending on properties of the ash material composition and the particle temperature [32]. The specific surface area of the reacting core S_V''' is calculated based on the Random Pore Model [52, 53] with an adjustable factor γ. The factor γ, a dependent function of the effective factor η and the carbon conversion X_c, is expressed as Eq. (5.35) in Chapter 5.

$$S_V''' = \gamma\, S_{m,0}''' \rho_{C,0}(1-X_c)\sqrt{1-\Psi\,\ln(1-X_c)} \tag{6.23}$$

where $S_{m,0}'''$ is the initial mass specific surface area, and Ψ is the structure parameter.

The diffusion rate coefficient $k_{diff,i}$ is determined based on the Sherwood number Sh [21, 22, 25, 37, 90] with a blowing factor θ_b accounting for the influence of the Stefan flow on the species transport from the gas phase to the particle surface, and the convective heat transfer between the particle and the gas phase [39, 74, 91]

$$k_{diff,i} = \frac{\theta_b\, Sh\, D_{i,m}}{d_p} \tag{6.24}$$

$$Sh = 2 + 0.6 Re^{\frac{1}{2}}\, Sc^{\frac{1}{3}} \tag{6.25}$$

where Re is the particle Reynolds number and Sc is the Schmidt number. The blowing factor θ_b is calculated as in the following formula [39]

$$\theta_b = \frac{b}{e^b - 1} \tag{6.26}$$

where b is calculated as

$$b = \frac{c_{p,g}\,(dm_p/dt)}{2\pi d_p \lambda_g} \tag{6.27}$$

where $c_{p,g}$ is the heat capacity of the gas, dm_p/dt is the char conversion rate, d_p is the particle diameter, and λ_g is the thermal conductivity of the gas. The particle diameter d_p and density ρ_p are calculated as

$$d_p = \sqrt[3]{\frac{6\left(\frac{\pi d_{core}^3}{6} + \frac{m_a}{\rho_{a,t}(1-\varepsilon_a)}\right)}{\pi}} \tag{6.28}$$

$$m_a = \frac{\pi}{6}(d_{core,0}^3 - d_{core}^3)\,\rho_{a,0} \tag{6.29}$$

$$\rho_p = \frac{m_p}{V_p} \tag{6.30}$$

where m_a is the mass of the ash layer, and V_p is the particle volume. The particle temperature T_p is obtained by analytically solving the heat balance equation for the char particle [27]

$$m_p c_{p,p}\frac{dT_p}{dt} = A_p\theta_b\, h_{conv}(T_\infty - T_p) + A_p\epsilon_p\sigma(\theta_R^4 - T_p^4) + \sum_{j=1}^{N_{het}} V_{core}\frac{M_{w,C}|\nu_{C,j}|}{M_{w,i}|\nu_{i,j}|}S_V'''\,R_{het,j}\,\Delta H_{het,j} \tag{6.31}$$

The final term in Eq. (6.31) explains the heat of heterogeneous reactions. $\Delta H_{het,j}$ denotes the heterogeneous reaction's enthalpy. Eq. (6.8) or Eq. (6.9) is numerically solved using user define functions (UDFs) to determine the species mass fraction $Y_{i,s}$ while tracking the particle. Taking the particle temperature T_p obtained by solving Eq. (6.31) and the partial pressure $p_{i,s}$ from Eq. (6.6), the consumption rate of species i due to the heterogeneous reaction j is determined using Eq. (6.1). Mass, species and energy exchange between the dispersed particles and the gas phase are added in the continuity equation, species transport equations and energy equation as sources.

6.2 Model Validation

6.2.1 Experimental Data

The Pressurized Entrained Flow Reactor (PEFR) developed by the Commonwealth Scientific and Industrial Research Organization (CSIRO) are used to validate a CFD reactor model, which uses the Hybrid Particle Model to describe the char conversion process taking place inside the PEFR. CRC-274 denotes a type of coal fed the PEFR. The proximate and ultimate analyses for CRC-274 are given in Table 6.1 [50, 51].

Tab. 6.1: Ultimate and proximate analysis for CRC-274 [50, 51]

Proximate analysis (% as received)		Ultimate analysis (% daf)	
Volatile matter	29.4	C	83.7
Fixed carbon	60.8	H	4.8
Moisture	4.7	O	9.1
Ash	9.8	N	2.0
LHV (daf) (MJ/kg)	33.0	S	0.4

The coal was ground and fractionated to a range from 30 µm to 250 µm with d_{10}=57.4 µm and d_{50}=109.8 µm [81]. A Rosin–Rammler distribution is used to describe the particle size distribution of the coal fed the reactor. The mass fraction of particles with diameters larger

than the diameter d_p is given by

$$Y_{p,d} = \exp\left[-\left(\frac{d_p}{\bar{d}_p}\right)^{n_d}\right] \tag{6.32}$$

where $\bar{d}_p$ and n_d are the mean diameter and the spread parameter of the particle size distribution, respectively. Based on the values of d_{10} and d_{50}, the size distribution parameters are determined: $\bar{d}_p$=124.6 µm and n_d=2.9.

The reactor is operated at a pressure of 20 bar with the inner wall temperature adjusted to 1673 K by electrical wall heating. 2.0 kg/h of coal, transported by N_2 with 5.01 m^3 N/h as the carrier gas, enters from the top center of the reactor. An additional mixture consisting of air with 7.22 m^3 N/h and N_2 with 17.95 m^3 N/h as the oxidizing reactant gas is preheated to 1273 K and supplied to the PEFR. The measurement data such as the temperature, the gas composition and the particles probed at four different positions along the reactor [72, 89] are used to compare with the PEFR CFD simulation results. A schematic diagram of the PEFR is shown in Figure 6.2 [50, 72].

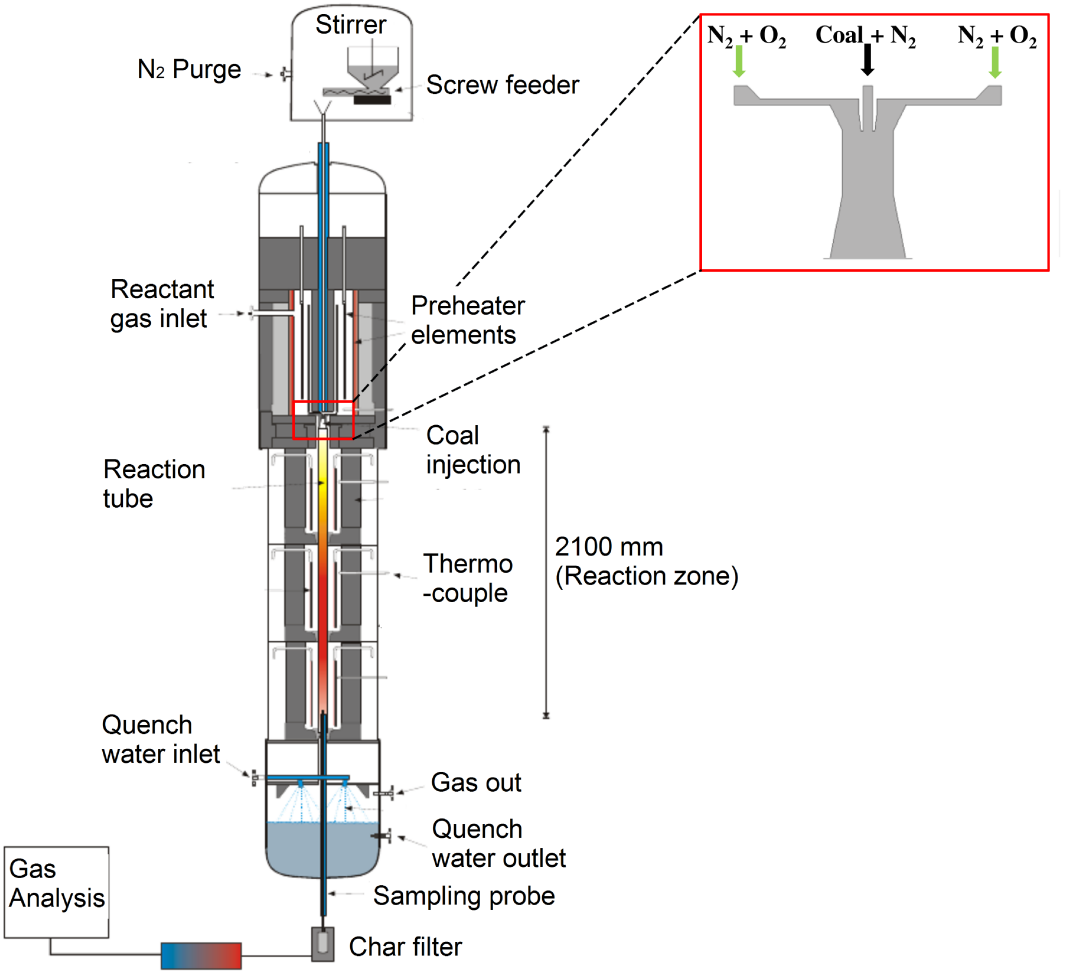

Fig. 6.2: A schematic diagram of the pressurized entrained-flow reactor (PEFR) [50, 72]

6.2.2 Validation

The CFD simulation of the PEFR is performed using a 2D axis-symmetric model. The heating and pyrolysis processes are based on standard models of ANSYS-Fluent®. The empirical

Competing 2-Step Model (C2SM) is applied for describing the rate of the pyrolysis process. Approximate pyrolysis kinetics for CRC-274 is given in Table 6.2 [37, 89], and the amount of volatile matter released, which was calculated by the CPD model, is 0.4169 kg/kg (daf fuel). The volatile matter decomposes very quickly into light gas and tar, which react with oxidants such as O_2 and H_2O in the gas phase by the following reactions.

$$\mathsf{Vol} \longrightarrow 0.2756\,\mathsf{H_2O} + 0.0449\,\mathsf{CO_2} + 0.3618\,\mathsf{CH_4} + 0.0696\,\mathsf{CO} + 0.0937\,\mathsf{C_2H_2} + 0.0655\,\mathsf{N_2} + 0.0887\,\mathsf{Tar} \tag{R10}$$

$$\mathsf{Tar} + 7\,\mathsf{O_2} \longrightarrow 14\,\mathsf{CO} + 8.2451\,\mathsf{H_2} \tag{R11}$$

$$\mathsf{Tar} + 14\,\mathsf{H_2O} \longrightarrow 14\,\mathsf{CO} + 22.2451\,\mathsf{H_2} \tag{R12}$$

Tab. 6.2: Kinetic parameters of C2SM for CRC-274 [37, 89]

Step	$k_{j,\infty} \big/ 1/\mathrm{s}$	$E_{a,j} \,\big/\, \mathrm{J/kmol}$	Y_j
1	1.026×10^5	6.246×10^7	0.2875
2	7.993×10^7	1.190×10^8	0.6261

The optical microscopy analysis of the CRC-274 char sample and the observation of little change in the CRC-274 particle density during the conversion process inside the PEFR [81] indicate that the char structure produced by the CRC-274 coal under the PEFR operation conditions is characterized by Group III. Therefore, the Hybrid Particle Model is applicable to model the conversion process of the CRC-274 char particle. The heterogeneous reaction rate is modeled based on the intrinsic kinetics. The kinetics parameters given in [92] are converted into $\mathrm{kg/(m^2\,s\,Pa^n)}$ and are given in Table 6.3. The initial specific surface area for the char particle $S'''_{m,0}$ is estimated at $270\,\mathrm{m^2/g}$ and the swelling factor C_{sw} is taken as a value of 1.35 [81]. The structural parameter Ψ is estimated at 3.0 [23, 37, 49].

Tab. 6.3: Reaction rate of heterogeneous reactions for CRC-274 [92]

Reac.	$k_{j\infty} \,\big/\, \mathrm{kg/(m^2\,s\,Pa^n)}$	$E_{a,j} \,\big/\, \mathrm{J/kmol}$	n_j
R7	198.95	2.89×10^8	0.4
R8	5.9685	2.28×10^8	0.4
R9	0.00137	1.38×10^8	0.8

When the ash layer is not included in the Hybrid Particle Model and the particle shape is assumed to be spherical and unchanged, Eq. (6.9) is solved to determine the heterogeneous reaction rates. The particle trajectories are tracked based on the drag coefficient calculated using Eq. (4.26). As a result, the velocity, temperature field and the mole fraction distribution of species along the height of the PEFR are shown in Figure 6.3. It can be seen that the temperature (Figure 6.3a) and gas velocity (Figure 6.3b) are distributed nearly homogeneously over the volume of the gasifier except for the heating zone, where coal particles are heated up and decomposed into pyrolysis products, such as tar and volatile materials (Figure 6.3c). Coal particles enter the gasifier with high velocity and devolatilize quickly to form char, some of which combusts. The remainder of the char is consumed by relatively slow gasification reactions, producing a gas mixture at the outlet with a high concentration of CO and H_2. Figure 6.3d shows that O_2 is consumed very quickly by the tar and volatile to produce a vapor of H_2O and CO_2 in the combustion zone. Then, CO_2 and H_2O vapor react with char

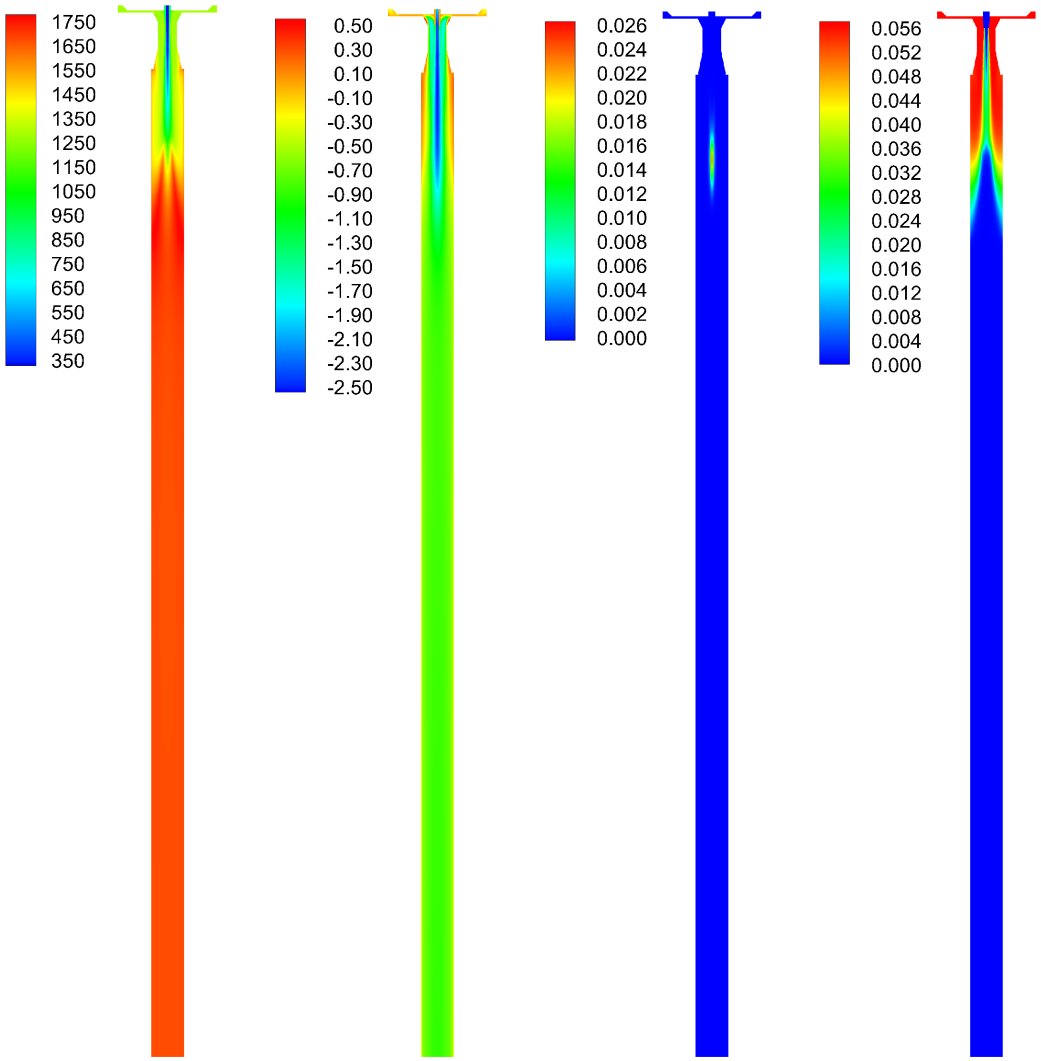

(a) temperature, K (b) velocity, m/s (c) $x_{vol.}$, mol/mol (d) x_{O_2}, mol/mol

Fig. 6.3: Temperature velocity and species model fraction distribution along the height of the PEFR

by gasification reactions to form CO and H_2. The mole fractions of CO_2, H_2O, CO and H_2 along the height of the PEFR are shown in Figure 6.4.

Figure 6.5 compares the CFD simulation results obtained from the current particle model with the experiment and published data in [51, 72, 89]. Figure 6.5a shows the total carbon conversion profile X_C along the height of the reactor. The carbon conversion level at different intersecting planes is calculated based on the amount of carbon in the gas phase. The total carbon conversion predicted by the current model is in good agreement with the experimental data. The predicted overall carbon conversion from the current model is 84.5 % which is 9.0 % lower than the final carbon conversion stated in the previous study [89], which used the similar approach for the char conversion process but modeled the density exponent α using Eq. (2.48) in Chapter 2, and closer to the experimental data. Figure 6.5b shows the distribution of the mole fraction of species such as CO, CO_2 and H_2 along the height of the reactor. Generally, the mole fraction distribution of CO_2 and H_2 predicted by the current model and the previous model are in good agreement with the experimental data however, the CO mole fraction differs significantly between the two models at the reactor outlet and the current model shows a better agreement with the experimental data. The current model predicts a CO mole fraction of 0.0571, while the previous model reports approximately 0.0652.

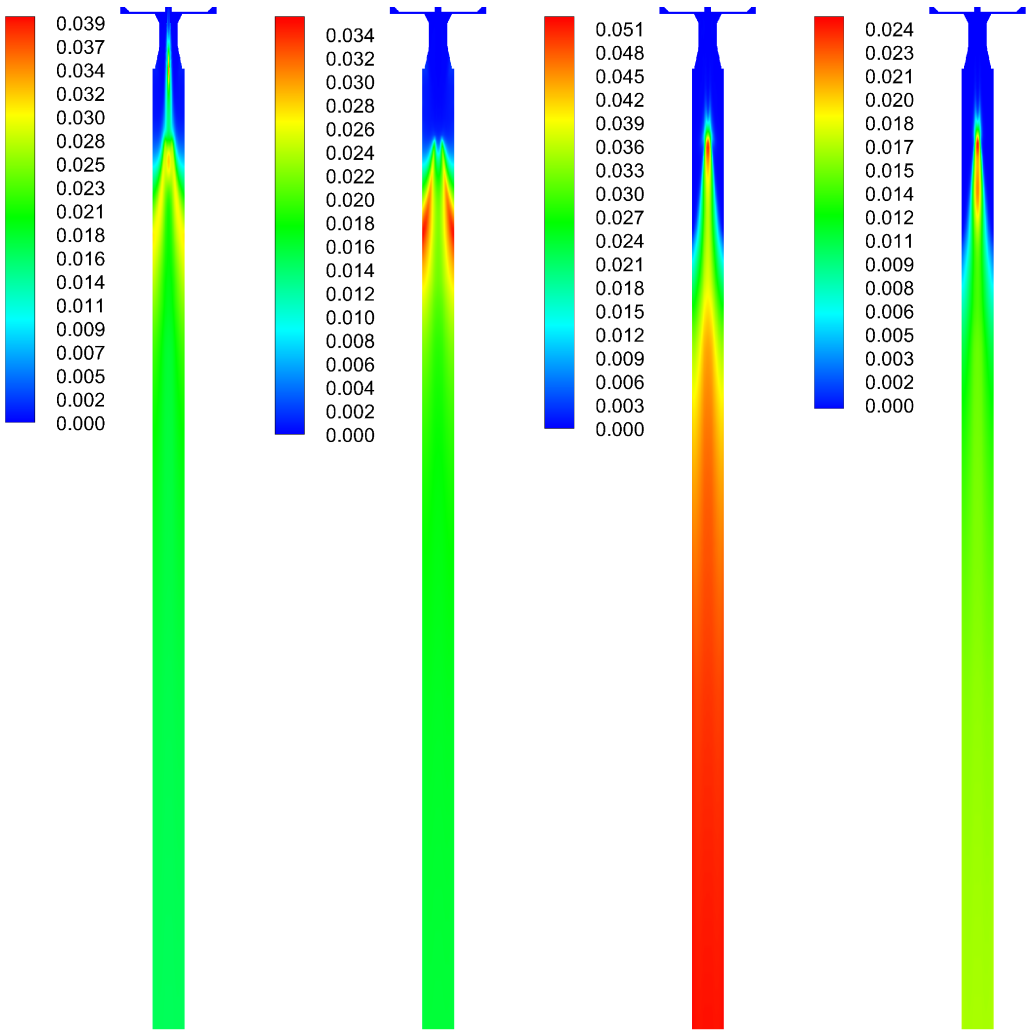

(a) x_{H_2O}, mol/mol (b) x_{CO_2}, mol/mol (c) x_{CO}, mol/mol (d) x_{H_2}, mol/mol

Fig. 6.4: Mole fraction distribution of species along the height of the PEFR

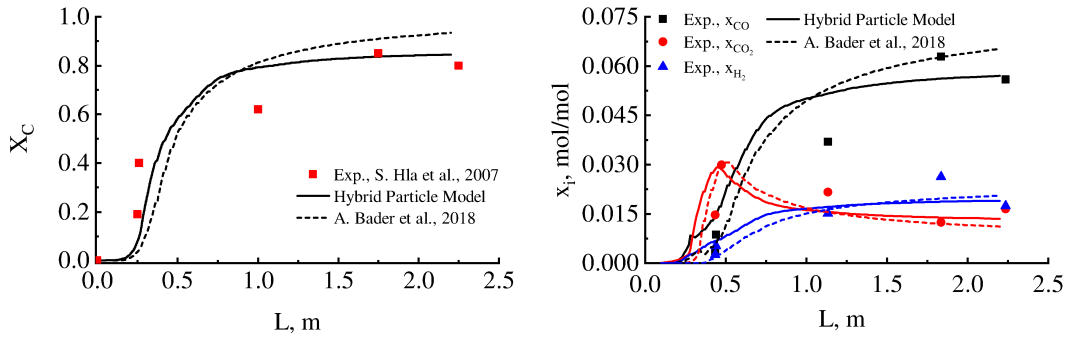

(a) total carbon conversion profile (b) distribution of species concentration

Fig. 6.5: Comparison of current numerical data to the experimental and published data for the PEFR

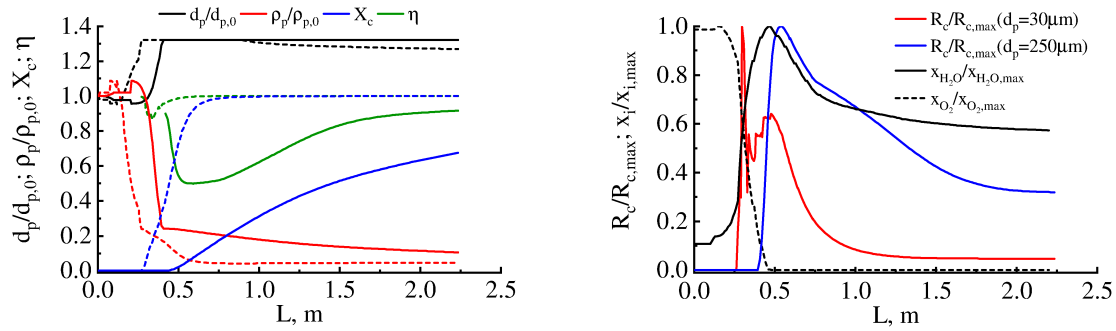

(a) particle morphology evolution

(b) relative char conversion rate

Fig. 6.6: Morphology evolution and relative char conversion rates of the smallest and biggest coal particles along the height of the PEFR. In (a), the dashed lines denote a 30 µm particle and the solid lines stand for a 250 µm particle

Figure 6.6 shows the conversion characteristics of a 30 µm and 250 µm particle, representing the smallest and largest sizes in the reactor feedstock, along the height of the reactor. Figure 6.6a demonstrates that the char conversion of the smallest particle starts at around 0.25 m of the reactor length and is complete. In contrast, the char conversion of the largest particle begins at about 0.4 m of the reactor length and reaches 68 % at the reactor outlet. After the drying and pyrolysis process, the particle size increases by a factor of 1.35 [81] due to the swelling process, leading to a reduction in the particle density. During the char conversion process, the density of the particles continuously decreases due to carbon consumption, while the particle diameters remain constant, except for the smallest particle at late conversion stages. This can be explained by the relation between the diameter exponent, β, the effectiveness factor, η, and the char conversion level, X_c, (see Eq. (5.31) and Figure 5.9 in Chapter 5). For the largest particle, at its early conversion stages when the X_c is less than 5 %, the η reaches its minimum, 0.5, resulting in a zero value of the diameter exponent, β, and consequently a constant diameter. Similarly, the carbon conversion level of the largest particle at the reactor outlet is around 68 % with $\eta = 0.9$ resulting in a zero value of β again and constant diameter. However, for the smallest particle at its late conversion stages, X_c is 100 % and η is close to 1 resulting in a small positive β value and a slight reduction in the particle diameter.

Figure 6.6b presents the relative char conversion rate of the smallest and largest particles and the relative distributions of O_2 and H_2O along the height of the reactor. The concentration of O_2 is depleted at around 0.5 m of the reactor length, while the concentration of H_2O increases to its maximal value due to the feedstock moisture released, and the volatile oxidized then decreases due to the consumption of char gasification reaction (R8). This is consistent with the O_2 and H_2O concentration distributions shown in Figure 6.3d and Figure 6.4a, respectively. It can be seen that the smallest char particle loses 50 % of its mass due to the oxidation reaction, while the largest particle mainly loses its mass due to the gasifying reactions. The char consumption rates of both particles reach maximal values, then fall along the height of the reactor. At the reactor outlet, the smallest particle's char consumption rate remains 4.69 % of the maximal rate, while the largest particle's char consumption rate stays at 31.39 %.

6.3 Influence of Particle Shape Development on Char Conversion

The ratio V_{core}/A_{core} in Eq. (6.5), Eq. (6.8) and Eq. (6.9) is equal to $\phi d_{core}/6$ for non-spherical particles. The reacting core diameter d_{core} of non-spherical particles is calculated based on

the volume-equivalent diameter to a spherical particle. When the ash layer is not included into the Hybrid Particle Model, Eq. (6.9) for the mass flux balance of the species i becomes Eq. (6.33) to describe the char conversion model of non-spherical particles conveniently.

$$k_{diff,i}\,\bar{\rho}_g(Y_{i,g}-Y_{i,s})-\phi\frac{d_{core}}{6}S_V'''\,\eta_j\frac{|\nu_{i,j}|M_{w,i}}{|\nu_{C,j}|M_{w,C}}\,k_{ta}\,k_{d,j\infty}\exp\left\{-\frac{E_{aj}}{R_G\,T_p}\right\}\left(\frac{R_G\,\bar{\rho}_g\,T_p\;Y_{i,s}}{M_{w,i}}\right)^{n_j}=0 \tag{6.33}$$

In the case of the particle shape kept constant, Eq. (6.33) is solved with a constant particle sphericity ϕ of the initial value ϕ_0 to calculate the mass faction of species $Y_{i,s}$, and hence the heterogeneous reaction rate $R_{het,j}$. As mentioned in Chapter 4, the particle shape changes during the char conversion process. When the influence of the ash material on the shape of particle is ignored, and the particle shape development is examined, the drag coefficient and the particle sphericity are considered as dependent functions of the particle Reynolds number and the char conversion level. It should be recalled that the char conversion level X_c is replaced by a term of $\left[1-(d_{core}/d_{core,0})^3\right]$ in the dynamic drag coefficient and the particle sphericity models, which were developed in Section 4.4 in Chapter 4, to make them be valid for Regime II. The influences of the shape development of several particles studied in Section 4.4 in Chapter 4 on overall carbon conversion of the PEFR are given in the following.

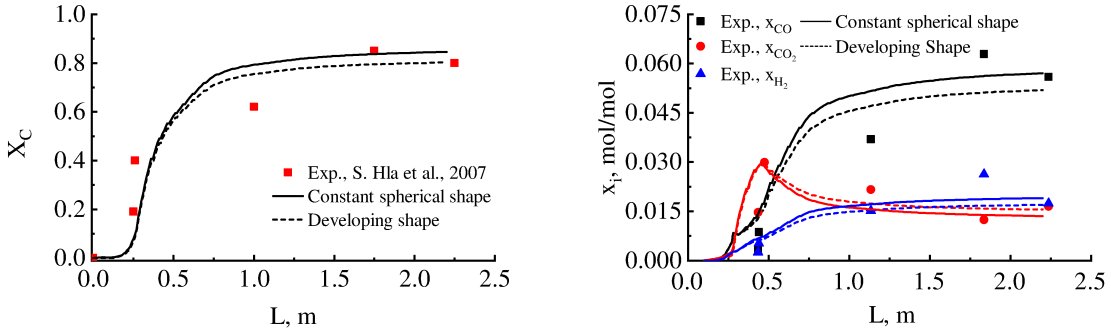

(a) total carbon conversion

(b) species distribution

Fig. 6.7: The influence of spherical particles' shape development on the performance of the PEFR

First, the feedstock with initially spherical shape is considered. Figure 6.7 compares the total carbon conversions and the species mole fraction distributions along the height of the PEFR for two cases. One assumes the particle shape remains spherical during the char conversion process (as presented in Section 6.2.2). The other considers the influence of the particle shape development, using Eq. (4.24) to compute the particle sphericity and Eq. (4.25) to calculate the drag coefficient. Figure 6.7a shows that the effect of changes in the particle shape on the total carbon conversion starts at X_C=60 % and causes the final carbon conversion to be 5.0 % lower compared with the spherical shape. Figure 6.7b presents a slight deviation in the CO_2 and H_2 mole fraction distribution between the two cases, but a large gap in the CO mole fraction profiles with a difference of 9.87 % at the reactor outlet.

Next, the cylinder and double cone are considered as an example of other feedstock e.g. municipal waste, biomass and recycled plastic. Figure 6.8 shows the total carbon conversion along the height of the PEFR using the cylinder and double cone for two cases: one is the particle shape constant and the other is shape development. When the shape development is taken into account with the char conversion process, the particle sphericity and drag coefficient of these particles are calculated based on Eq. (4.37) and Eq. (4.38), respectively. In comparison to the particle shape constant, where $c_{d,0}$ given in Eq. (4.39) for the cylinder and in Eq. (4.40) for the double cone were used to calculate particle trajectories during the char conversion

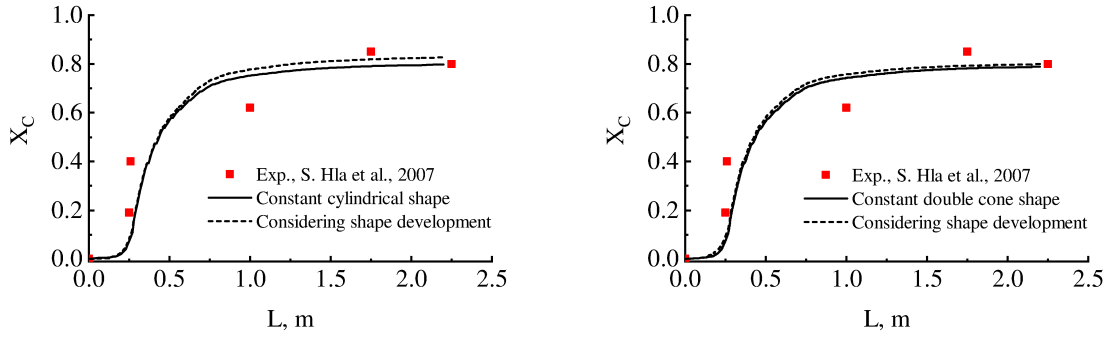

(a) cylindrical shape (b) double cone shape

Fig. 6.8: The influence of non-spherical particles' shape development on the total carbon conversion of the PEFR

process, the particle shape development leads to the final carbon conversion increasing by about 3.0 % for the cylinder, as shown in Figure 6.8a, while there is a minor difference for the double cone, as shown in Figure 6.8b. A comparison of Figure 6.7a to Figure 6.8 indicates that non-spherical particles cause the char conversion to decrease by a maximum of 5.0 %.

6.4 Conversion Behavior of Different Particle Sub Models

Usually, Regime II dominates the entire char conversion process inside an entrained-flow gasifier, and requires sub models describing changes in the particle diameter, density and specific surface area to calculate the char consumption rate. The most frequent particle sub models applied for the CFD modeling of entrained-flow gasifiers are the diffusion-limited model, kinetics/diffusion model and multiple surface reaction model. However, there are very poor definitions of the particle morphology evolution for those particle sub models. The shrinking core (SCM) model developed by Wen and Chaung is considered the best fit at very high chemical reaction rates, hence Regime III [24].

In addition to the Hybrid Particle Model used to model the char conversion process taking place in Regime II, this section illustrates different particle sub models, such as the Shrinking Density Model (SDM) and the Shrinking Particle Model (SPM) corresponding to Regimes I and Regimes III, respectively applied for the CFD modeling of the PEFR. The char conversion model for those particle sub models is identical to the Hybrid Particle Model, but the particle morphology evolution is modeled in consistent way with those. The particle shape is spherical for both the SDM and SPM.

In the case of the SDM, the char particle diameter is constant at the initial char diameter, hence the diameter exponent β in Eq. (6.10) equal to zero, the density exponent α in Eq. (6.11) is equal to 1.0, and the RPM without the correctness factor γ is applied for the specific surface area development. Due to no pore diffusion effect in the SDM, Eq. (6.9) with the effectiveness factor η_j equal to 1.0 is solved to determine the mass fraction $Y_{i,s}$, hence to calculate the species consumption rate $R_{het,j}$.

As opposed to the SDM, the SPM characterizes the particle density to be constant at the initial char density, hence the density exponent α equal to zero, the diameter exponent β equal to 1/3, and the specific surface area to be constant at the initial value $S'''_{V,0}$. The ash layer is also excluded from the SPM in order to compare the SPM to the Hybrid Particle Model and the SDM. Therefore, Eq. (6.9) with the effective factor η calculated by Eq. (6.4) is solved to find the mass fraction $Y_{i,s}$, and hence the species consumption rate $R_{het,j}$ for the

SPM.

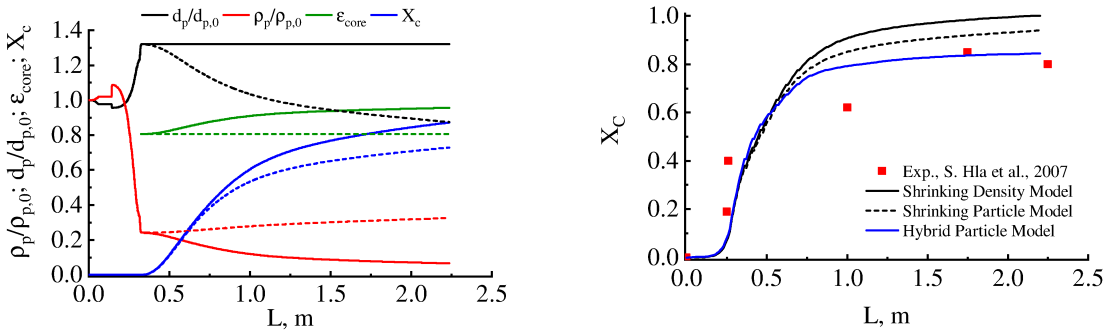

(a) particle morphology evolution

(b) total carbon conversion profiles

Fig. 6.9: Morphology evolution of a 125 µm coal particle and overall carbon conversion of the PEFR corresponding to different particle sub models. In (a) the solid lines stand for the Shrinking Density Model and the dashed lines denote the Shrinking Particle Model

Figure 6.9 shows the morphology evolution of the char particle with a mean size of 125 µm, and total carbon conversion profiles along the height of the PEFR corresponding to the SDM, SPM and Hybrid Particle Model. In addition to the development of the particle diameter and particle density, which is consistent with the corresponding regimes, Figure 6.9a shows that the porosity of the reacting core ε_{core} increases in the case of the SDM, while it remains constant in the case of the SPM during char conversion process. Figure 6.9b indicates that the total carbon conversion predicted using the SDM and SPM is an overestimation compared to the Hybrid Particle Model and the experimental data. The final carbon conversion is mostly 100 % for the SDM and reaches 94.0 % for the SPM, while it is 84.5 % for the Hybrid Particle Model.

6.5 Ash Inhibition

Many investigations have mentioned that the char oxidation and gasification rate can be enhanced by mineral matter due to catalysis, especially at low temperatures. However, at high temperatures when transport effects are especially important, and at the late stages of conversion where the mineral matter is the dominant component, the ash's net effect is inhibitory [32]. The ash inhibition acting on the char conversion rate can be explained by one of several physical mechanisms, such as additional resistance to species reactant transport to the reacting zone, or melted ash blocking the micro-pore structure [23, 32]. To the author's best knowledge, the ash formation process has not been thoroughly studied, and ash inhibition is rarely included in particle sub models.

This section studies the simple model of ash inhibition, which describes a resistance to the species transport from the gas phase to the reaction volume of a char particle. The Hybrid Particle Model shown in Figure 6.1 assumes that there is a porous ash layer around the carbon-rich core. After the pyrolysis process, when the char conversion starts, the boundary surface of the reacting core, the blue line in Figure 6.1, coincides with the outer particle surface. As the conversion progresses, an ash layer is formed only when the boundary surface separates from the outer particle surface and moves towards the particle center. The separation depends on the diameter exponent β. Maybe, β equals to zero during the whole conversion process of the char particle (see again Figure 5.9 in Chapter 5), hence no ash layer is formed at the char particle. When the carbon content of the char particle has been converted completely, the char particle turns into an ash particle, whose diameter and density are constant and are

calculated using Eq. (6.28) and Eq. (6.30), respectively.

The char conversion model considering ash inhibition is expressed as in Eq. (6.8). The ratio V_{core}/A_{core} in Eq. (6.5) and Eq. (6.8) equals $d_{core}/6$ when the particle shape is assumed to be spherical and remains constant during the char conversion process. There are two important parameters to model the ash inhibition: the ash layer's porosity ε_a and its thickness, which depends on the coal ash content and the density of nonporous ash. The ash layer thickness is calculated by applying $(d_p - d_{core})/2$. The reacting core diameter d_{core} and the particle diameter d_p are calculated using Eq. (6.10) and Eq. (6.28), respectively. The ash porosity ε_a, which is adjustable model parameter, has a value in a range from 0.16 to 0.5, and the density of nonporous ash $\rho_{a,t}$ has a value of 2.6 g/cm^3 [32, 85]. Eq. (6.8) was solved to calculate the heterogeneous reaction rate $R_{het,j}$. As a result, the comparison of total carbon conversion and species mole fraction along the height of the PEFR between the Hybrid Particle Model with or without ash inhibition (presented in Section 6.2.2) is shown in Figure 6.10.

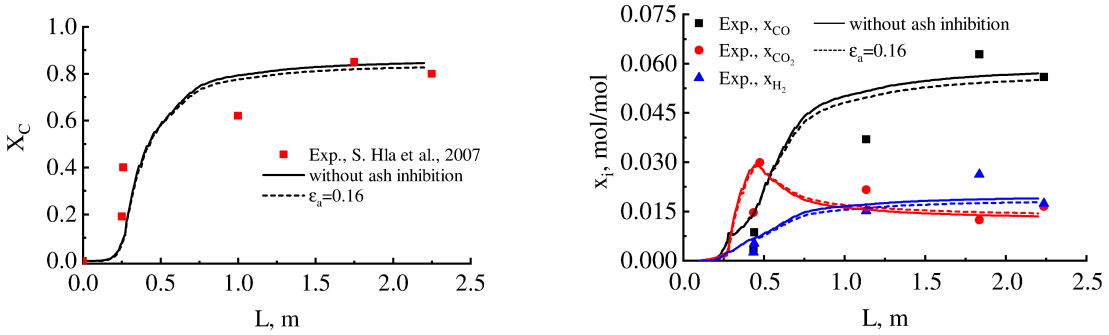

(a) total carbon conversion profile

(b) species distributions

Fig. 6.10: The influence of ash inhibition on the performance of the PEFR

From Figure 6.10a, it can be seen that the ash inhibition starts to affect the total carbon conversion from 70 %, and the final carbon conversion is only 2.0 % lower in comparison to that predicted using the Hybrid Particle Model without ash inhibition, even when the ash porosity is set at the smallest value ε_a=0.16. Figure 6.10b shows a minor deviation in the CO_2 and H_2 mole fraction distribution, but a noticeable enough difference 3.64 % in the outlet CO mole fraction of the two models.

6.6 Conclusion

This chapter introduces a particle sub model, which is derived from the analytical approach, for the chemically reacting char particle. The particle sub model uses the effectiveness factor to account for the diffusion limitation affecting the char consumption rate. The particle sub model consists of an ash layer surrounding a reacting core, whose morphology changes during the char conversion process. The evolution of the reacting core morphology is described using several sub models. The emphasis here is that the sub models describing the morphology evolution are amended using the particle-resolved model. Consequently, the accuracy of the particle sub model in predicting the char consumption rate is improved. The dynamic drag model accounting for the impact of the particle shape development on the char conversion process is studied. From the obtained results, it can be concluded that:

1. The particle sub model together with sub models describing the particle morphology evolution enhances the reliability of the CFD modeling of the entrained-flow gasifier.

2. The particle shape development influences the performance and efficiency of the entrained-flow gasifier significantly.
3. The Shrinking Density Model and the Shrinking Particle Model corresponding to the theoretical regimes, such as Regimes I and III over-predict the char conversion rate, and hence the entrained-flow gasifier's performance and efficiency. Therefore, selecting a particle sub model suitable with real operating conditions of a entrained-flow gasifier to calculate the char conversion rate plays an important role in obtaining reliable simulation results of a CFD-based modeling of the entrained-flow gasifier.
4. Generally, ash layering particle prevents reactant diffusing from the bulk phase to the reaction volume of the char particle. Therefore, it reduces the char consumption rate, hence the performance and efficiency of the entrained-flow gasifier. However, the ash material's influence on the final carbon conversion of the entrained-flow gasifier is minor for the coal with a moderate ash content (for example, 10 % in this study),

7 Conclusion

This Ph.D. thesis develops reliable sub models describing the particle morphology evolution during the char conversion process based on the PRM in order to improve the quality of CFD-based modeling of entrained-flow gasifiers. The modeling approach is described systematically from particle to reactor scale. Based on the results achieved, main conclusions are drawn:

1. Although much computational effort is put into describing and solving the particle-resolved model of a chemically reacting char particle, the particle-resolved model plays an essential role in developing and improving sub models to depict the char conversion process more accurately. In particular, at the micrometer scale of particle size, no equipment can be used to directly measure and observe the conversion process within a char particle, but the particle-resolved model can give details information of the conversion process, and estimate conversion parameters.
2. Based on the CFD simulation of particle-resolved models, the evolution of the particle morphology, and complex physical and chemical phenomena occurring during the char conversion process are observed in detail and are understood further. The shape of the boundary layer around a reacting char particle depends directly on the Reynolds number and particle shape, consequently, the carbon consumption rate is characterized by a non-uniform distribution on the outer particle surface. A direct relationship between the particle shape development and the distribution consumption rate is shown. Moreover, the complex relations between the internal carbon conversion and the evolution of pore structure as well as the changes in particle volume, density and specific surface area are also quantified, that extends the knowledge of the evolution of particle morphology during the char conversion process.
3. New sub models for the drag coefficient and the char conversion parameters emerge from the analysis of numerical data obtained from the CFD simulation of particle models. The sub models are crucial to improve the reliability of the CFD simulation of an entrained-flow gasifier. Dynamic drag coefficient models, which depend on the particle shape development, are developed for different initial particle shapes to improve the accuracy of particle trajectories inside an entrained-flow gasifier. The fundamental parameters for the char conversion model, such as the diameter and density exponent and the evolution of the internal surface area, are considered as dependent functions not only of the effectiveness factor but also of the char conversion level. The dependent functions are applicable to a wide range of process conditions.
4. The Hybrid Particle Model of a chemically reacting char particle combined with the sub models describing the particle morphology evolution improves the accuracy and reliability of the CFD modeling of the entrained-flow gasifier. Especially, the particle sub model can predict an accurate char consumption rate at the ending of char conversion process, where particle sub models usually decline in their accuracy due to significant changes in the particle morphology and the intensive ash inhibition. The particle sub model shows sensitivities to input model parameters. The shape influences overall char conversion significantly with a deviation up to 5.0 %, and a small decrease below 2.0 % in overall char conversion due to ash inhibition can be also observed. Hence, the particle sub model has great potential in designing optimal entrained-flow gasifiers.

Bibliography

[1] C. Higman and M. van der Burgt. *Gasification*. Elsevier Science, 2003.

[2] D. Safronov, T. Förster, D. Schwitalla, P. Nikrityuk, S. Guhl, A. Richter, and B. Meyer. "Numerical study on entrained-flow gasification performance using combined slag model and experimental characterization of slag properties". In: *Fuel Processing Technology* 161 (2017), pp. 62–75.

[3] M. Gräbner. *Industrial Coal Gasification Technologies Covering Baseline and High-Ash Coal*. Wiley-VCH Verlag GmbH & Co. KGaA, 2015.

[4] P. A. Nikrityuk and B. Meyer, eds. *Gasification Processes: Modeling and Simulation*. Wiley-VCH Verlag GmbH & Co. KGaA, 2014.

[5] A. Richter and P. A. Nikrityuk. "Drag forces and heat transfer coefficients for spherical, cuboidal and ellipsoidal particles in cross flow at sub-critical Reynolds numbers". In: *International Journal of Heat and Mass Transfer* 55 (2012), pp. 1343–1354.

[6] K. Wittig, P. Nikrityuk, and A. Richter. "Drag coefficient and Nusselt number for porous particles under laminar flow conditions". In: *International Journal of Heat and Mass Transfer* 112 (2017), pp. 1005–1016.

[7] W. Nusselt. "Der Verbrennungsvorgang in der Kohlenstaubfeuerung". In: *Zeitung des Vereins Deutscher Ingenieure* 68 (1924), p. 124.

[8] S. P. Burke and T. E. W. Schuman. "NOTES AND CORRESPONDENCE: Kinetics of a Type of Heterogeneous Reactions the Mechanism of Combustion of Pulverized Fuel". In: *Industrial and Engineering Chemistry* (1931), p. 721.

[9] S. R. Turns, ed. *An Introduction to Combustion- 2nd Edition*. McGraw- Hill, 2000.

[10] P. Nikrityuk, M. Gräbner, M. Kestel, and B. Meyer. "Numerical study of the influence of heterogeneous kinetics on the carbon consumption by oxidation of a single coal particle". In: *Fuel* 114 (2013), pp. 88–98.

[11] A. Richter, P. Nikrityuk, and M. Kestel. "Numerical investigation of a chemically reacting carbon particle moving in a hot O_2/CO_2 atmosphere". In: *Industrial and Engineering Chemistry Research* 52 (2013), pp. 5815–5824.

[12] A. Richter, P. Nikrityuk, and B. Meyer. "Three-dimensional calculation of a chemically reacting porous particle moving in a hot O_2/CO_2 atmosphere". In: *International Journal of Heat and Mass Transfer* 83 (2015), pp. 244–258.

[13] A. Richter, M. Vascellari, P. A. Nikrityuk, and C. Hasse. "Detailed analysis of reacting particles in an entrained-flow gasifier". In: *Fuel Processing Technology* 144 (2016), pp. 95–108.

[14] D. Safronov, M. Kestel, P. A. Nikrityuk, and B. Meyer. "Particle resolved simulations of carbon oxidation in a laminar flow". In: *The Canadian Journal of Chemical Engineering* 92.10 (2014), pp. 1669–1686.

[15] S. Kriebitzsch and A. Richter. "LES simulation of char particle gasification at Reynolds numbers up to 1000". In: *Combustion and Flame* 211 (2020), pp. 185–194.

[16] K. Wittig, P. Nikrityuk, S. Schulze, and A. Richter. “Three-dimensional modeling of porosity development during the gasification of a char particle”. In: *AIChE Journal* 63.5 (2017), pp. 1638–1647.

[17] F. Dierich, A. Richter, and P. Nikrityuk. “A fixed-grid model to track the interface and porosity of a chemically reacting moving char particle”. In: *Chemical Engineering Science* 175 (2018), pp. 296–305.

[18] M. Beckmann, J. Bibrzycki, M. Mancini, A. Szlęk, and R. Weber. “Mathematical modeling of reactants’ transport and chemistry during oxidation of a millimeter-sized coal-char particle in a hot air stream”. In: *Combustion and Flame* 180 (2017), pp. 2–9.

[19] G. H. Fong, S. Jorgensen, and S. L. Singer. “Pore-resolving simulation of char particle gasification using micro-CT”. In: *Fuel* 224 (2018), pp. 752–763.

[20] C. B. Nguyen, J. Scherer, Q. Guo, S. Kriebitzsch, and A. Richter. “The Shape Development of Spherical and Non-Spherical Char Particles in the Flame Zone of an Entrained-Flow Gasifier – A Numerical Study”. In: *International Journal of Heat and Mass Transfer* 149 (2019).

[21] M. Vascellari, R. Arora, and C. Hasse. “Simulation of entrained flow gasification with advanced coal conversion submodels. Part 2: Char conversion”. In: *Fuel* 118 (2014), pp. 369–384.

[22] O. Levenspiel, ed. *Chemical Reaction Engineering, Third Edition*. John Wiley & Sons, Inc., 1999.

[23] A.Tremel and H. Spliethoff. “Gasification kinetics during entrained flow gasification – Part II: Intrinsic char reaction rate and surface area development”. In: *Fluel* 107 (2013), pp. 653–661.

[24] J. Mularski, H. P. Kruczek, and N. Modlinski. “A review of recent studies of the CFD modelling of coal gasification in entrained flow gasifiers, covering devolatilization, gas-phase reactions, surface reactions, models and kinetics”. In: *Fuel* 271 (2020).

[25] S. Schulze, A. Richter, M. Vascellari, A. Gupta, B. Meyer, and P. A. Nikrityuk. “Novel intrinsic-based submodel for char particle gasification in entrained-flow gasifiers: Model development, validation and illustration”. In: *Applied Energy* 164 (2016), pp. 805–814.

[26] M. M. Baum and P. J. Street. “Predicting the Combustion Behaviour of Coal Particles”. In: *Combustion Science and Technology* 3 (1971), pp. 231–243.

[27] Inc. ANSYS. *Fluent™ User’s Guide*. 2018.

[28] M. A. Field. “Rate of combustion of size-graded fractions of char from a low-rank coal between 1200K and 2000K”. In: *Combustion and Flame* 13 (1969), pp. 237–252.

[29] I. W. Smith. “The combustion rates of coal chars: A review”. In: *Symposium (International) on Combustion* 19 (1982), pp. 1045–1065.

[30] C. Y. Wen and T. Z. Chaung. “Entrainment Coal Gasification Modeling”. In: *Ind. Eng. Chem. Process Des. Dev.* 18(4) (1979), pp. 684–695.

[31] D. A. Bell, B. F. Towler, and M. Fan. “Gasification Fundamentals”. In: *Coal Gasification and Its Applications* (2011), pp. 35–71.

[32] R.Hurt, J. K. Sun, and M. Lunden. “A Kinetic Model of Carbon Burnout in Pulverized Coal Combustion”. In: *Combustion and Flame* 113 (1998), pp. 181–197.

[33] S. Niksa, G. S. Liu, and R. H. Hurt. “Coal conversion submodels for design applications at elevated pressures. Part I: Devolatilization and char oxidation”. In: *Progress in Energy and Combustion Science* 29 (2003), pp. 425–477.

[34] G. S. Liu and S. Niksa. “Coal conversion submodels for design applications at elevated pressures. Part II: Char gasification”. In: *Progress in Energy and Combustion Science* 30 (2004), pp. 679–717.

[35] R. J. Wijngaarden, A. Kronberg, and K. R. Westerterp. “Calculation of Effectiveness Factor”. In: *Industrial Catalysis: Optimizing Catalysts and Processes*. Wiley-VCH Verlag GmbH, 1998.

[36] U. Kleinhans, S. Halama, and H. Spliethoff. “Char particle burning behavior: Experimental investigation of char structure evolution during pulverized fuel conversion”. In: *Fuel Processing Technology* 171 (2018), pp. 361–373.

[37] M. Vascellari, D. G.Roberts, S.S. Hal, D.J. Harris, and C. Hasse. “From laboratory-scale experiments to industrial-scale CFD simulations of entrained flow coal gasification”. In: *Fuel* 152 (2015), pp. 58–73.

[38] Sümer M. Peker and Şerife Ş. Helvaci. “4 - Motion of Particles in Fluids”. In: *Solid-Liquid Two Phase Flow* (2008), pp. 245–289.

[39] Thomas H. Fletcher. “Gasification fundamentals”. In: *Integrated Gasification Combined Cycle (IGCC) Technologies*. 2017.

[40] R. Clift, J. R. Grace, and M. E. Weber. “Bubbles, Drops and Particles”. In: *Academic Press* 94 (1979), pp. 795–796.

[41] A. Haider and O. Levenspiel. “Drag Coefficient and Terminal Velocity of Spherical and Nonspherical Particles”. In: *Powder Technology* 58 (1989), pp. 63–70.

[42] W. E. Ranz and W. R. Marshall. “Evaporation From Drops”. In: *Chemical Engineering Progress* 48(3) (1952), pp. 141–146.

[43] S. Whitaker. “Forced convection heat transfer correlations for flow in pipes, past flat plates, single cylinders, single spheres, and for flow in packed beds and tube bundles”. In: *AIChE Journal* 18(2) (1972), pp. 361–371.

[44] Z. Xue, Q. Guo, Y. Gong, J. Xu, and G. Yu. “Numerical study of a reacting single coal char particle with different pore structures moving in a hot O_2/CO_2 atmosphere”. In: *Fuel* 206 (2017), pp. 381–389.

[45] Z. Xue, Y. Gong, Q. Guo, Y. Wang, and G. Yu. “Conversion characteristics of a single coal char particle with high porosity moving in a hot O_2/CO_2 atmosphere”. In: *Fuel* 256 (2019), p. 115967.

[46] K. E. Benfell. “Assessment of char morphology in high pressure pyrolysis and combustion”. Ph. D. Thesis. Department of Geology, University of Newcastle, 2000.

[47] K. E. Benfell, G. S. Liu, D. G. Roberts, D. J. Harris, J. A.Lucas, J. G. Bailey, and T. F. Wall. “Modeling char combustion: The influence of parent coal petrography and pyrolysis pressure on the structure and intrinsic reactivity of its char”. In: *Proceedings of the Combustion Institute* 28 (2000), pp. 2233–2241.

[48] E. M. Hodge. “The coal char–CO_2 reaction at high temperature and high pressure”. Ph. D. Thesis. School of chemical engineering and industrial chemistry, University of New South Wales, Sydney, 2009.

[49] S. S. Hla, D. G. Roberts, and D. J. Harris. “A numerical model for understanding the behaviour of coals in an entrained-flow gasifier”. In: *Fuel Processing Technology* 134 (2015), pp. 424–440.

[50] D. Harris, D. Roberts, and D. Henderson. “Gasification behaviour of Australian coals at high temperature and pressure”. In: *Fuel* 85 (2006), pp. 134–142.

[51] S. S. Hla, D. J. Harris, and D. G. Roberts. "CFD modelling for an entrained flow gasification reactor using measured intrinsic kinetic data". In: *Fifth International Conference on CFD in the Process Industries*. Melbourne, Vic.

[52] S. K. Bahatia and D. D. Perlmutter. "A Random Pore Model for Fluid-Solid Reactions. I: Isothermal, Kinetic Control". In: *AlChE Journal* 26(3) (1980), pp. 379–386.

[53] S. K. Bahatia and D. D. Perlmutter. "A Random Pore Model for Fluid-Solid Reactions . II: Diffusion and Transport Effects". In: *AlChE Journal* 27(2) (1981), pp. 247–254.

[54] R. H.Essenhigh. "Influence of initial particle density on the reaction mode of porous carbon particles". In: *Combustion and Flame* 99 (1994), pp. 269–279.

[55] R. H.Essenhigh. "An integration path for the carbon-oxygen reaction with internal reaction". In: *Symposium (International) on Combustion* 22(1) (1989), pp. 89–96.

[56] L. Ma. "Combustion and Gasification of Chars in Oxygen and Carbon Dioxide at Elevated Pressure". Ph. D. Thesis. Stanford University, 2006.

[57] S. Halama and H. Spliethoff. "Numerical simulation of entrained flow gasification: Reaction kinetics and char structure evolution". In: *Fuel Processing Technology* 138 (2015), pp. 314–324.

[58] André Bakker. *Turbulence Models*. URL: `http://www.bakker.org/dartmouth06/engs150/10-rans.pdf`. (accessed: 20.07.2020).

[59] H. K. Versteeg and W. Malalasekera, eds. *An Introduction to Computational Fluid Dynamics*. PEARSON Prentice Hall, 2007.

[60] André Bakker. *Kolmogorov's Theory*. URL: `http://www.bakker.org/dartmouth06/engs150/09-kolm.pdf`. (accessed: 20.07.2020).

[61] B. F. Magnussen. "The Eddy Dissipation Concept a Bridge Between Science and Techology". In: *ECCOMAS Thematic Conference on Computational Combustion*. Lisbon, Portugal, 2005.

[62] I. R. Gran and B. F. Magnussen. "A Numerical Study of a Bluff-Body Stabilized Diffusion Flame. Part 2. Influence of Combustion Modeling and Finite-Rate Chemistry". In: *Combustion Science and Technology* 119 (1996), pp. 191–217.

[63] L. Talbot, R. Cheng, R. Schefer, and D. Willis. "Thermophoresis of Particles in a Heated Boundary Layer". In: *Journal of Fluid Mechanics* 101(4) (1980), pp. 737–758.

[64] A. M. Bechmann. "Experiments and CFD Modeling of Pulverized Coal Flames with Emphasis on Fly Ash Deposition". Ph. D. Thesis. TU Clausthal, 2017.

[65] K. Wittig, A. Richter, and P. A. Nikrityuk. "Numerical study of heat and fluid flow past a cubical particle at sub-critical Reynolds numbers". In: *Computational Thermal Sciences Journal* 4.4 (2012), pp. 283–296.

[66] R. Raul, P. S. Bernard, and F. T. Buckley. "An application of the vorticity-vector potential method to laminar cube flow". In: *International Journal for Numerical Methods in Fluids* 10(8) (1990), pp. 875–888.

[67] R. Mittal. "A Fourier–Chebyshev spectral collocation method for simulating flow past spheres and spheroids". In: *International Journal for Numerical Methods in Fluids* 30 (1999), pp. 921–937.

[68] S. A. Isaev and D. A. Lysenko. "Calculation of unsteady flow past a cube on the wall of a narrow channel using URANS and the Spalart–Allmaras turbulence model". In: *Journal of Engineering Physics and Thermophysics* 82 (2009), pp. 488–495.

[69] A. Hölzer and M. Sommerfeld. “Lattice Boltzmann simulations to determine drag, lift and torque acting on non-spherical particles”. In: *Computers & Fluids* 38(3) (2009), pp. 572–589.

[70] M. Kestel. “Numerical Modeling of Moving Carbonaceous Particle Conversion in Hot Environments”. Ph. D. Thesis. TU Bergakademie Freiberg, Germany, 2016.

[71] S. R. Turns. *An Introduction to Combustion: Concepts and Applications*. McGraw Hill Higher Education, 2011.

[72] S. S. Hla, D. Harris, and D. Roberts. *Gasification Conversion Model – PEFR*. Research report 80. Cooperative research centre for coal in suistainable development. 2007.

[73] B. J. McBride, S. Gordon, and M. A. Reno. *Coefficients for calculating thermodynamic and transport properties of individual species*. Tech. rep. NASA TM-4513, 1993.

[74] R. B. Bird, W. E. Stewart, and E. N. Lightfoot. *Transport Phenomena*. John Wiley & Sons, 2007.

[75] G. Krishnamoorthy, R. Rawat, and P. J. Smith. “Parallelization Of The P-1 Radiation Model”. In: *Journal Numerical Heat Transfer* 49(1) (2006), pp. 1–17.

[76] D. Safronov, P. Nikrityuk, and B. Meyer. “Fixed-grid method for the modelling of unsteady partial oxidation of a spherical coal particle”. In: *Combustion Theory and Modelling* 16(4) (2012), pp. 589–610.

[77] P. A. Bejarano and Y. A. Levendis. “Single-coal-particle combustion in O_2/N_2 and O_2/CO_2 environments”. In: *Combustion and Flame* 153(1-2) (2008), pp. 270–287.

[78] M. Rodriguez and R. Raiko. “Effect of O_2 and CO_2 Content on Particle Surface Temperature and Size of Coal Char During Combustion”. In: *Proceedings of the Finnish-Swedish Flame Days* (2009), pp. 28–29.

[79] R. Stauch and U. Maas. “Transient detailed numerical simulation of the combustion of carbon particles”. In: *International Journal of Heat and Mass Transfer* 52 (2009), pp. 4584–4591.

[80] F. Küster, P. Nikrityuk, M. Junghanns, S. Nolte, A. Tünnermann, R. Ackermann, A. Richter, S. Guhl, and B. Meyer. “In-situ investigation of single particle gasification in a defined gas flow applying TGA with optical measurements”. In: *Fuel* 194 (2017), pp. 544–556.

[81] D. Harris, D. Roberts, and D.Henderson. *Gasification behaviour of Australian coals*. Research report 43. Cooperative research centre for coal in sustainable development. 2003.

[82] C. B. Nguyen, J. Scherer, M. Hartwich, and A. Richter. “The morphology evolution of char particles during conversion processes”. In: *Combustion and Flame* 226 (2021), pp. 117–128.

[83] A.Tremel and H. Spliethoff. “Gasification kinetics during entrained flow gasification – Part I: Devolatilisation and char deactivation”. In: *Fuel* 103 (2013), pp. 663–671.

[84] F. A. L.Dullen. *Porous Media: Fluid Transport and Pore Structure*. Academic Press, Inc, 1991.

[85] M. R. Schure, P. A. Soltys, D. F. S. Natusch, and T. Mauney. “Surface Area and Porosity of Coal Fly Ash”. In: *Environmental Science & Technology* 19(1) (1985), pp. 82–86.

[86] P. Edge, M. Gharebaghi, R. Irons, R. Porter, R. T. J. Porter, M. Pourkashanian, D. Smith, P. Stephenson, and A. Williams. “Combustion modelling opportunities and challenges for oxy-coal carbon capture technology”. In: *IChemE* 89 (2011), pp. 1470–1493.

[87] P. Walker, F. Rusinko, and L. Austin. “Gas Reactions of Carbon”. In: *Advances in Catalysis* 11 (1959), pp. 133–221.

[88] P. A. Nikrityuk, M. Gräbner, M. Kestel, and B. Meyer. “Numerical study of the influence of heterogeneous kinetics on the carbon consumption by oxidation of a single coal particle”. In: *Fuel* 114 (2013), pp. 88–98.

[89] A. Bader, M. Hartwich, A. Richter, and B. Meyer. “Numerical and experimental study of heavy oil gasification in an entrained-flow reactor and the impact of the burner concept”. In: *Fuel Processing Technology* 169 (2018), pp. 58–70.

[90] M. Vascellari, C. Hasse, P. Nikrityuk, S. Schulze, and D. Safronov. “Numerical simulation of pulverized coal MILD combustion using a new heterogeneous combustion submodel”. In: *Flow, Turbulence and Combustion* 92.1–2 (2014), pp. 319–345.

[91] H. Niazmand and M. Renksizbulut. “Transient three-dimensional heat transfer from rotating spheres with surface blowing”. In: *Chemical Engineering Science* 58 (2003), pp. 3535–3554.

[92] S. S. Hla, D. J. Harris, and D. G. Roberts. “A coal conversion model for interpretation and application of gasification reactivity data”. In: *2005 ICCS & T*. Okinawa, Japan, 2005.